A novel approach to thin film deposition and rare-earth incorporation for silicon integrated photonics

A novel approach to thin film deposition and rare-earth incorporation for silicon integrated photonics

By Jeremy William Miller, B. Eng

A Thesis Submitted to the School of Graduate Studies in the Partial Fulfillment of the Requirements for the Degree Doctor of Philosophy

McMaster University

McMaster University

Doctor of Philosophy (2020)

Hamilton, Ontario (Department of Engineering Physics)

TITLE: A novel approach to thin film deposition and rare-earth incorporation for silicon integrated photonics

AUTHOR: Jeremy William Miller (McMaster University)

SUPERVISORS: Dr. Peter Mascher and Dr. Jonathan Bradley

NUMBER OF PAGES: xviii, 156

Abstract

In this thesis, group IV material oxides for silicon photonics applications were deposited using novel deposition techniques. Erbium and terbium doped silicon oxide thin films were deposited through a novel hybrid radio frequency (RF) magnetron sputtering source in an electron cyclotron resonance (ECR)-plasma enhanced chemical vapour deposition (PECVD) reactor chamber. This approach contrasts with traditional doping methods which use metal-organic precursors to introduce rare-earth dopant species into the host matrix. The effects of sputtering power applied to the rare-earth target and system plasma pressure on the thin film properties were investigated. It was found that the sputtering power strongly influences the rare-earth incorporation, and a wide range of control over the doping level can be achieved. The effect of sputtering power on the refractive index, stoichiometry, and film density were also investigated. Doped thin films deposited with this technique showed low as-deposited hydrogen concentrations. In the case of terbium doped silicon oxide (SiO_x), photoluminescence (PL) studies were conducted finding bright emission due to $^5D_4 \rightarrow {}^7F_5$ transitions visible with the naked eye in films annealed above 1150 °C. Further investigation found that silicon nanostructures formed at the high annealing temperatures and were likely sensitizing the Tb^{3+} ions. These results demonstrate that hybrid sputtering in ECR-PECVD can be an effective tool for integrating optically active rare-earth dopants into silicon-based thin films. Using alternating current (AC) plasma assisted reactive magnetron sputtering (PARMS), low optical loss germanium oxide (GeO_2) thin films were also produced. The films were fabricated at low temperature and high deposition rates of 6–38 nm/min on silicon and thermally oxidized silicon substrates.

Prism coupling measurements demonstrated losses of 0.1 dB/cm at wavelengths ranging from 638 to 980 nm attributed to good uniformity and low surface roughness demonstrated through atomic force microscopy (AFM) measurements. The thin films materials developed here are highly promising for their applications in silicon photonics devices, including light sources and amplifiers.

Acknowledgements

First and foremost, I would like to express my deepest gratitude towards my supervisors, Dr. Peter Mascher and Dr. Jonathan Bradley, whose continual support, patience, and knowledge helped me throughout my research. Their trust in my work and the opportunities they provided me helped to develop my confidence as a researcher. I would also like to thank my committee member Dr. Andrew Knights for his guidance and challenging questions throughout my degree.

I am grateful to all the members of the 'Mascher,' 'Bradley,' and the 'Knights' Research Groups, past and present, who provided me with much-needed support during my research, especially Austin Brown, Aysegul Abdelal, Dawson Bonneville, Khadijeh Miarabbas Kiani, Hamidu Mbonde, Cameron Naraine, Renjie Wang, David ('DJ-L') Hagan, Dixon ('D $') Paez-Capacho and Ross ('the boss') Anthony.

This work would not have been possible without help from some incredible individuals. I would like to thank Shahram Tavakoli for all his assistance with maintaining the CVD system. His technical advice and mentorship allowed me to develop confidence in maintaining and upgrading deposition systems. I am thankful to Jacek Wojcik for his early mentorship and assistance and the opportunities he provided me, both in the fields of research and backcountry camping. Zhiling Peng for his help with the SEM and TEM sample preparation. Doris Stevanovic for her guidance and for being my TAB lab work neighbour. Lyudmila Goncharova and Jack Hendrix at Western University for their assistance and advice with RBS and ERDA.

I would like to acknowledge Dino Deligiannis and Michael Chesaux for the opportunity to collaborate with them at IntlVac. Many thanks to Raytheon ELCAN for their invaluable work experience, allowing me to pursue exciting research and challenges. I would also like to thank the Center of Emerging Device Technologies for their equipment and resources. Finally, I am also thankful to all the funding agencies that found my research interesting—specifically, the Department of Engineering Physics, the Ontario Graduate Scholarships program, the SIEPIC CREATE program, the Ontario Ministry of Research and Innovation, the Ontario Research Fund and the Society of Vacuum Coaters (SVC).

To my family and friends who have each provided tremendous support over these years. I am especially grateful to my mother, who has always been supportive of me in the decisions I made and provided me with invaluable advice. Even in the most challenging times, she has given me a positive and supporting perspective. A special thanks to my partner Alex for being there for me throughout all the highs and the lows of research. Finally, I would also like to acknowledge my late pet cat Charlie who provided me with much-needed company and distraction. This endeavour would not be possible without everyone's tremendous love and support.

Contents

List of Figures

List of Tables

Acronyms

3D	Three-dimensional
$^4He^+$	Helium Ion
AC	Alternating Current
AFM	Atomic Force Microscopy
Al_2O_3	Alumina
AM	Amplitude Modulated
Ar	Argon
Au	Gold
CCD	Charge-coupled Device
CCEM	Canadian Centre for Electron Microscopy
CMOS	Complementary Metal-oxide-semiconductor
CVD	Chemical Vapour Deposition
DC	Direct Current
ECR	Electron Cyclotron Resonance
EDFA	Erbium Doped Fibre Amplifier
EDX	Energy Dispersive X-ray Spectroscopy
EELS	Electron Energy Loss Spectroscopy
Er	Erbium
ERDA	Elastic Recoil Detection Analysis
FIB	Focused Ion Beam
FM	Frequency Modulated

Ga	Gallium
Ge	Germanium
GeO_2	Germanium Oxide
HeCd	Helium Cadmium
HR	High Resolution
HV	High Vacuum
IP	Internet Protocol
N_2	Molecular Nitrogen
NCHR	Non-contact / Tapping^{TM} Mode - High Resonance Frequency - Reflex Coating
NIR	Near-infrared
O_2	Oxygen
PARMS	Plasma Assisted Reactive Magnetron Sputtering
PC_RSA	Polariser - Rotating Compensator - Sample - Analyser
PECVD	Plasma Enhanced Chemical Vapour Deposition
PID	Proportional–integral–derivative
PL	Photoluminescence
PLC	Programmable Logic Controller
Pt	Platinum
PVD	Physical Vapour Deposition
RBS	Rutherford Backscattering Spectrometry
RF	Radio Frequency
RGA	Residual Gas Analyzer
RMS	Root Mean Squared
SAED	Selected Area Electron Diffraction

sccm	Standard Cubic Centimeters per Minute
SEM	Scanning Electron Microscopy
SiC	Silicon Carbide
SiH_4	Silane
Si_3N_4	Silicon Nitride
SiO_2	Silicon Dioxide
SiO_x	Silicon Oxide
SOI	Silicon On Insulator
Tb	Terbium
TE	Transverse Electric
TEM	Transmission Electron Microscopy
TeO_2	Tellurium Oxide
TM	Transverse Magnetic
UHV	Ultra High Vacuum
UV	Ultraviolet
VASE	Variable Angle Spectroscopic Ellipsometry
vdW	Van der Waals
VLSI	Very Large Scale Integration
VUV	Vacuum Ultraviolet
WDM	Wavelength-division Multiplexing
WP	Witness Piece

Portions of this work have been published in:

Surface and Coatings Technology

DOI: 10.1016/j.surfcoat.2017.08.051

and

Thin Solid Films

DOI: 10.1016/j.tsf.2020.138165.

Chapter 1

Introduction

There is an exponential increase in internet protocol (IP) traffic around the world driven by consumer demand for digital video media, cloud-based services, and associated machine-learning applications. It is estimated that currently, about 80% of all IP traffic is in the from of video traffic; with every second, one million minutes of video is being sent across the internet [1]. This data, originating from data centres, travels along long-haul fibre optic networks to reach the end-user. However, for every byte of data sent out from a data centre, multiple bytes are sent around within. For certain services, such as social media, the internal data traffic may exceed the external traffic by several orders of magnitude [2]. This has created two important challenges that need to be resolved. The first is the need to create network architectures within the data centre that can support an ever-increasing bandwidth. The second is the management of the growing power consumption for these data centres, which already accounts for 1.5% of the total energy consumed in the U.S. [1].

Much like the solution in the early 1990s that met IP traffic bandwidth needs

through fibre optic systems, short-haul communication within data centres can be achieved through optical interconnects, which provide both higher bandwidths and lower energy cost per bit when compared to traditional metal interconnects. Silicon photonics leverages the economy of scale and technological sophistication of the complementary metal-oxide-semiconductor (CMOS) electronics industry to solve the challenge of manufacturing low-cost, high bandwidth optical communications. These photonic circuits are comprised of building blocks that have, for the most part, reached a stage of maturity. These building blocks include waveguides [3]–[5], filters [6], modulators [7]–[9] and photodetectors [10]–[12]. The key challenge, however, is the development of an efficient monolithic silicon light source compatible with silicon on insulator (SOI). Any such advancement could also be leveraged for other light-emitting applications that could benefit from a low-cost silicon-based light source and ease of integration with CMOS infrastructure.

Light emission from solid-state sources is primarily achieved through the use of III-V compounds. These can be integrated with silicon through III-V to silicon wafer bonding, direct epitaxial growth on silicon or SOI using intermediate buffer layers, or through butt-coupling via precise assembly. All these approaches face considerable challenges due to their complexity and cost [13]. Monolithic materials will be, by contrast, a less complex solution to integrate into SOI and, consequently, less costly to implement.

1.1 Challenges with regards to light emission from silicon

Compared to a direct bandgap semiconductor, recombination in silicon is inefficient. This inefficiency is due to the conservation of momentum requirements, which results in the necessity of phonon mediated radiative transitions. Most solutions to this problem involve the creation of highly spatially confined structures to generate quantum confinement, allowing for the relaxation of momentum requirements for radiative transitions to occur [14]. Engineering the dimensions of these quantum structures can allow for tuning of emission energies, which allows for emission of photons with much higher energies than the bandgap of silicon (1.11 eV), at room temperatures.

There are many approaches to engineering these quantum confined systems in silicon. Bulk silicon can be etched using chemicals or plasma processes to form porous silicon [15]–[17], one-dimensional silicon structures can be grown in the form of nanowires [18]–[20], and zero-dimensional structures can be generated in the form of quantum dots or silicon nanocrystals [21]–[23]. The latter of these is compatible with very large scale integration (VLSI) technology making them an appealing solution for light-emitting device fabrication [14]. Significant progress has been made through bandgap engineering of group-IV materials. Growth of silicon-germanium alloy nanowires has successfully resulted in temperature-insensitive radiative recombination with sub-nanosecond lifetimes [18]. However, due to the complex patterning nature and the requirement of a III-V nanowire core, it is yet to be seen if this will be a viable low-cost solution for monolithic integration into

silicon photonic circuits.

Another solution is to forgo the challenges of engineering silicon to emit light altogether and dope silicon-based materials with rare-earth ions. Rare-earth dopants are prominent in many light-emitting applications due to their distinct narrow emission bands, wide range of emission wavelengths and high radiative recombination efficiency. Erbium is perhaps the most well-studied rare-earth for light emission. Since the late 1980s, it has been a well-established material for light amplification in long-haul telecommunications due to the invention of the erbium doped fibre amplifier (EDFA). EDFAs amplify wavelengths near 1.55 µm, which sits nicely in silica's low loss transparency window. Erbium doping in silicon-based thin films has since been an intensively researched field encompassing carbide [24]–[26], nitride [27]–[29], oxide [30]–[32], and porous [33]–[35] materials. Other such rare-earths have also garnered interest due to the success and popularity of erbium. Terbium is a rare-earth element with strong green emission lines, which makes it popular in display and lighting applications. Although research of terbium doped silicon-based thin films dates back 30 years to the early 1990s [36], [37], the body of publications on the topic is not nearly as extensive as erbium-doped silica.

Certain drawbacks need to be overcome, however, for rare-earth-doped silicon-based materials to become truly competitive. Multiphoton relaxation can rapidly depopulate excited states and ion-ion interactions between nearby rare-earth ions constitute a non-radiative decay pathway leading to quenching of luminescence. The strong dependence of the rare-earth emission on the concentration of rare-earth ions, impurities and host properties necessitates a deposition method that offers a wide range of control over rare-earth doping concentration while also enabling

both high film purity and optical quality [38].

Ex-situ rare-earth doping of thin films is performed using ion implantation. This process's major drawbacks are the introduction of potentially unwanted defects into the thin films and a depth-dependent distribution profile for rare-earth ion concentrations [39], [40]. In a plasma enhanced chemical vapour deposition (PECVD) process, the concentration of rare-earth ions can be controlled during the growth process, leading to a more uniform material with fewer defects than other conventional techniques. To date, metal-organic precursors are primarily applied for *in-situ* rare-earth doping during the PECVD process [41]. However, metal organics are highly sensitive to temperature variability. The heating of the foreline and crucible required for transporting the metal organics to the reactor strongly influences doping concentrations, and often there are challenges associated with replicating these strict temperature conditions. Furthermore, metal organics tend to introduce significant hydrogen contamination into the deposited films.

1.2 Germanium oxide thin films

Germanium oxide (GeO_2) is a material that is widely used in photonic applications because of its advantageous structural and optical properties. GeO_2 first gained interest in its applications in doped optical fibers due to its structural similarities to silica, allowing for ease of integration into fiber cores [42]. GeO_2 glass has strong inter-ionic forces between the Ge^{4+} and O^{2-} ions which provide high thermal stability and mechanical strength [43]. It has a higher refractive index (n = 1.6) than silica and is used to increase the numerical aperture of optical fibers. GeO_2 possesses a high Raman gain coefficient when compared to other oxide-based glasses

[44], making it a strong candidate for Raman based amplification. It also shows promise as a host for rare earth dopants amplifiers and lasers due to its high rare-earth solubility [45]. Its low nonlinearity and absorption allow for long-distance optical transmission in fibers [46]. GeO_2 glass possesses strong opto-refractive effects allowing for permanent shifts in refractive index when exposed to ultraviolet (UV) radiation [45], [47], [48]. This property is used to write Bragg gratings in optical fibers by UV laser exposure for applications, including fiber lasers, sensors, and dispersion compensators [49]–[52].

GeO_2's high refractive index and low loss also make it a promising material for planar waveguide applications. Because it is a CMOS compatible material already extensively used in silicon foundries for high-k gate dielectrics [53], [54], it is particularly attractive for silicon photonics platforms [55]. Its high rare-earth solubility motivates its use in on-chip amplifiers and lasers. Optical gain and lasing have been demonstrated in germanosilicate glass [56] and several authors have reported efficient photoluminescence in rare-earth-doped germinate alloys such as lead-, antimony-, and bismuth-germinate glasses [57]–[61]. The UV sensitivity of GeO_2 suggests it might be useful for grating structures or as a UV-sensitive cladding material for post-process trimming to increase yield in silicon photonics devices [62].

While the physical and material properties of GeO_2 thin films have been explored, there has been limited investigation towards the fabrication of low loss thin films. GeO_2 thin films have been previously fabricated by radio frequency (RF) sputtering and reactive direct current (DC) sputtering [43], [63]–[65]. Both of these techniques have been able to achieve high deposition rates; however, they have not been able to

produce films with as-deposited losses of less than 1.9 dB/cm at 638 nm. The losses in these films have been reduced by post-deposition annealing or laser annealing, which adds processing steps and increases fabrication complexity [43]. Germanate based alloy waveguide structures have achieved losses ranging from around 0.6 to 2.2 dB/cm at 632 nm, with these losses being attributed to scattering off of the waveguide sidewalls [66], [67].

1.3 Thesis objectives and methods

The objective of this thesis is to investigate novel means of depositing thin films for silicon photonics, and solid-state lighting applications. This objective, in part, involves the development of a new hybrid deposition technique based on a hybrid RF sputtering modality within an electron cyclotron resonance (ECR)-PECVD system. Structural and luminescent properties of the thin films are influenced by a broad range of processing parameters, which were studied experimentally to understand the developed material systems and the tool used to produce them. The development of this new deposition technique and the results yielded by this research will facilitate the fabrication of novel material systems.

Rare-earth-doped silicon oxides have already been extensively studied. However, hybrid sputtering in an ECR-PECVD system provides an *in-situ* rare-earth incorporation modality that is open to study. This investigation served to understand an alternative means of incorporating rare-earth dopants and overcoming metal-organic precursors potential shortcomings. It was expected that the rare-earth sputtering targets would limit the contamination that arises from using metal-organics with different vapour pressures and reduce the incorporation of hydrogen known to

form quenching OH groups for specific rare-earth transitions. While the results are inconclusive, there has been seen a reduction in hydrogen concentration in as-deposited films.

GeO_2 was investigated as a second material system due to its CMOS-compatibility and interesting physical and optical properties. It possesses both a strong photorefractive effect that could be exploited for device tuning on a silicon photonic chip as well as a high Raman gain coefficient compared to other oxide-based glasses. However, the investigation of this material system focused on the deposition of high growth rate and low-optical loss material, both qualities that are important in producing economically and optically efficient devices. Similar material studies have been conducted in the past; however, the one presented in the thesis is unique. It explores a specialized material deposition technique known to produce high optical quality thin-films. The system used in this study was a plasma assisted reactive magnetron sputtering (PARMS) alternating current (AC) sputtering tool, and the research presented in this thesis is the first instance of GeO_2 being grown and characterized using this system.

As a whole, this work aims to look at group IV material systems deposited through novel deposition techniques for future use in silicon photonics platforms to help meet an increasing need for high bandwidths.

1.4 Statement of thesis work

This thesis contains seven chapters and contributes to the knowledge of novel group IV thin film deposition techniques for the fabrication of silicon-based photonic

devices. This contribution is made with a focus on a new deposition system capable of *in-situ* rare-earth doping of silicon-based thin films and AC PARMS for low-loss GeO_2 thin films. This introductory chapter has established the motivations for the thesis and highlighted key contributions to the field.

Chapter 2 reviews the background and theory behind light emission from rare-earth ions. A summary of host materials for rare-earth incorporation in silicon photonics is then provided. Lastly, this is followed by the details of relevant deposition techniques.

In Chapter 3, characterization techniques and pertinent experimental detail related to studying the structural and optical properties of thin films are discussed. This chapter contains information and experimental details regarding Rutherford backscattering spectrometry (RBS), variable angle spectroscopic ellipsometry (VASE), atomic force microscopy (AFM), transmission electron microscopy (TEM), photoluminescence (PL) spectroscopy, and prism coupling. Furthermore, it highlights challenges encountered when using these techniques and advice to future students on how to navigate these issues.

In Chapter 4, the equipment and process parameters used to fabricate the thin film samples are described. This chapter begins with a detailed description and highlights the development of a hybrid sputtering system in an ECR-PECVD environment. The system geometry, installation of gas lines, programmable logic controller (PLC), and installation of components necessary for operation are all discussed. The techniques developed for the deposition of rare-earth-doped silicon-based thin films using the aforementioned system are discussed. This is followed by

a discussion about the PARMS system used to produce low loss GeO_2 thin films. Also, details are provided regarding the post-fabrication annealing process carried out on both material systems.

In Chapter 5, the experimental results for the calibration of the hybrid ECR-PECVD sputtering system using erbium (Er) are shown. This calibration is followed up with additional results showing the inclusion and optical activation of terbium (Tb) ions in a silicon oxide (SiO_x) matrix using the same deposition technique. A discussion of the material system follows.

Chapter 6 shifts focus onto GeO_2 as a low-loss material for potential integration into a silicon photonics platform. Specifically, it focuses on PARMS as a deposition technique and presents low-loss high deposition rate results for this material system.

Finally, in Chapter 7, a conclusion of the thesis is given followed by a brief discussion of future avenues of investigation.

1.5 Publications

Journal articles by the author which contribute to the work presented in this thesis are as follows:

- **J. W. Miller**, Z. Khatami, J. Wojcik, J. D. B. Bradley, and P. Mascher, "Integrated ECR-PECVD and magnetron sputtering system for rare-earth-doped Si-based materials", *Surface and Coatings Technology*, vol. 336, pp. 99–105, Feb. 2018

- **J. W. Miller**, M. Chesaux, D. Deligiannis, P. Mascher, and J. D. B. Bradley, "Low-loss GeO_2 thin films deposited by ion-assisted alternating current reactive sputtering for waveguide applications", *Thin Solid Films*, vol. 709, p. 138165, Sep. 2020

Conference proceedings and presentations which contribute to the work presented in this thesis:

- **J. W. Miller**, J. Wojcik, J. D. B. Bradley, and P. Mascher, "Calibration of a Circular HV Magnetron Sputtering Source for in-Situ RE Doping of ECR-PECVD Si-Based Thin Films", 229$^{\text{th}}$ Electrochemical Scociety, California, San Diego, May 29-June 2, 2016.

- **J. W. Miller**, Z. Khatami, J. Wojcik, J. D. B. Bradley, and P. Mascher, "Integrated ECR-PECVD and Magnetron Sputtering System for Rare-Earth-Doped Si-Based Materials", 60$^{\text{th}}$ Annual Technical Conference Proceedings 2017 Society of Vacuum Coaters, Providence, Rhode Island, April 29-May 4, 2017.

- **J. W. Miller**, A. Brown, Z. Khatami, J. Wojcik, and P. Mascher, "In-Situ Rare Earth Doping of Silicon-Based Nanostructures By Plasma Enhanced Chemical Vapour Deposition", Pacific Rim Meeting on Electrochemical and Solid-State Science (PRiME), Honolulu, Hawaii, October, 2016.

- **J. W. Miller**, D. Bonneville, N. Vadivelu, Z. Khatami, J. Wojcik, J. D. B. Bradley and Peter Mascher, "Green Light Emission from Terbium-Doped Si-Based Thin Films: ECR-PECVD films doped via a Circular HV Magnetron

Sputtering Source", Photonics North, Ottawa, Ontario, June, 2017.

Other journal articles by the author:

- C. M. Naraine, **J. W. Miller**, H. C. Frankis, D. E. Hagan, P. Mascher, J. H. Schmid, P. Cheben, A. P. Knights, and J. D. B. Bradley, "Subwavelength grating metamaterial waveguides functionalized with tellurium oxide cladding", Optics Express, vol. 28, no. 12, p. 18538, June, 2020.

Other proceedings and presentations by the author:

- **J. W. Miller**, A. P. Knights, J. D. B. Bradley, and P. Mascher , "Signal Enhancement from Silicon Slot Waveguide with ECR-PECVD Erbium-Doped Silica Cladding", Photonics North, Montreal, Quebec, June, 2018.

- **J. W. Miller**, C. M. Naraine, H. C. Frankis, D. E. Hagan, A. P. Knights, P. Mascher and J. D. B. Bradley, "Subwavelength Grating Waveguides Functionalized with Tellurium Oxide Cladding", Photonics North, Quebec City, Quebec, June, 2019.

1.5.1 Internship statement

Throughout this Ph.D., I had the opportunity to spend four months in a paid internship position at Raytheon ELCAN Optical Technologies in Midland, Ontario, as an Optical Thin Film Scientist. The work involved the study of thin film adhesion for infrared materials and optical interference coating characterization. Additionally, I collaborated in with Intlvac Inc., over the span over 6 months, developing thin film deposition processes.

Chapter 2

Luminescence from Rare-Earth Doped Materials

Many efforts have been made to turn silicon from an electronic material into an optical material. While silicon serves a role as a photonic material in its ability to guide, modulate, and detect light effectively, its major shortcoming in optoelectronic devices is that it is a poor light emitter [68]. Crystalline silicon's poor radiative efficiency is a result of its indirect bandgap. Its band structure is shown in Fig. 2.1 alongside gallium antimonide (GaSb), a direct bandgap semiconductor, as an example. In silicon, the minimum of the conduction band is located by the X point near the Brillion zone boundary along the $\langle 001 \rangle$, Δ, direction. This point is offset from the valance band maximum, located at the Γ point or Brillouin zone center (where the wave vector is $k = 0$). Radiative recombination across the bandgap would require mediation from a phonon, with an equal and opposite wave vector to the initial state of the electron in the conduction band, in order to maintain conservation of momentum. By contrast, an excited electron in the conduction

band of a direct bandgap semiconductor, such as GaSb, does not require a phonon and can relax spontaneously through photon emission [69]. Compared to a direct bandgap material, recombination in silicon is inefficient.

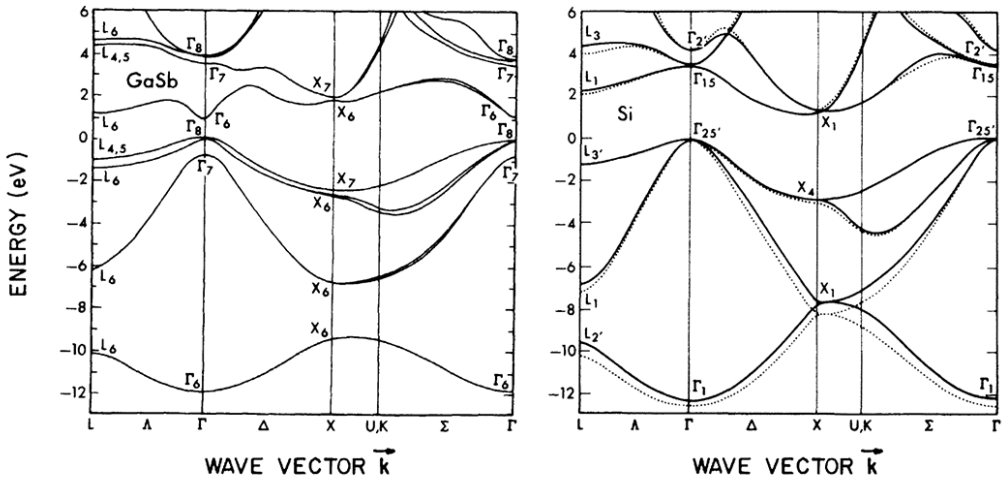

FIGURE 2.1: Band structures for gallium antimonide (GaSb) and silicon (Si) crystals, left and right, respectively. GaSb is a direct band-gap semiconductor as the minimum energy separation between the valence and conduction bands occurs at the Γ point. Si is an indirect band-gap semiconductor as the minimum energy separation requires traversing along the Δ direction in k-space. Reproduced with permission from [70] (© 1976 by the American Physical Society).

2.1 Rare-earth dopants

Luminescence from rare-earth ions has a long history of study dating back to the beginning of the 20$^{\text{th}}$ century. Rare-earth elements comprise the lanthanides (Z = 57-71) in addition to scandium (Z = 21) and yttrium (Z = 39). The energy levels of lanthanides in a range of materials were studied by Dieke and his colleagues in the 1960s [71]. When incorporated into a host, rare-earths most often ionize in a trivalent state, however they may sometimes have an other valance.

It is the trivalent rare-earth ions that are generally of interest, however, as these exhibit the most intense narrow-band intra-4f luminescence. The ground state electronic configuration of a trivalent lanthanide ion is [Xe]4f^{n} (n = 0-14). The sharp luminescent lines are attributed to the partially filled 4f shell that is shielded from external fields by the $5s^2$ and $5p^6$ electrons; an example is shown in Fig. 2.2 for reference. As a consequence of the shielding of 4f electrons, spin-orbit interactions rather than the applied crystal field influence the positions of the rare-earth electronic levels [38]. Laporte's parity selection rule would imply that the intra-4f transitions are parity forbidden; however, the crystal field interactions mix electronic states from opposite parity into the 4f wavefunctions through non-centrosymmetric interaction. This mixing relaxes the selection rules, and the transitions become partially allowed [72]. The effects of crystal field splitting are relatively minor; however, it does induce a slight broadening of the energy levels through the Stark effect. This broadening is most prevalent in the low point symmetry of rare-earth sites in amorphous matrices, such as glass [38].

The [Xe]4f^{n} configuration has a distinct energy separation from the [Xe]4$f^{n-1}5d^{1}$ configuration in the rare-earth structure. The 5d states will exhibit stronger coupling to lattice vibration modes as these are less localized around the ion and are strongly influenced by the host matrix. Transitions from [Xe]4$f^{n-1}5d^{1}$ to [Xe]4f^{n} are parity allowed and can exhibit intensities multiple orders of magnitude greater than intra-4f transition. The large energy separation, however, yields a low probability of expected interaction with a higher energy configuration [72], [75]. For some trivalent rare-earths, however, these transitions can be easily exploited, such as the strong blue luminescence given off by cerium (Ce^{3+}) when incorporated into certain hosts.

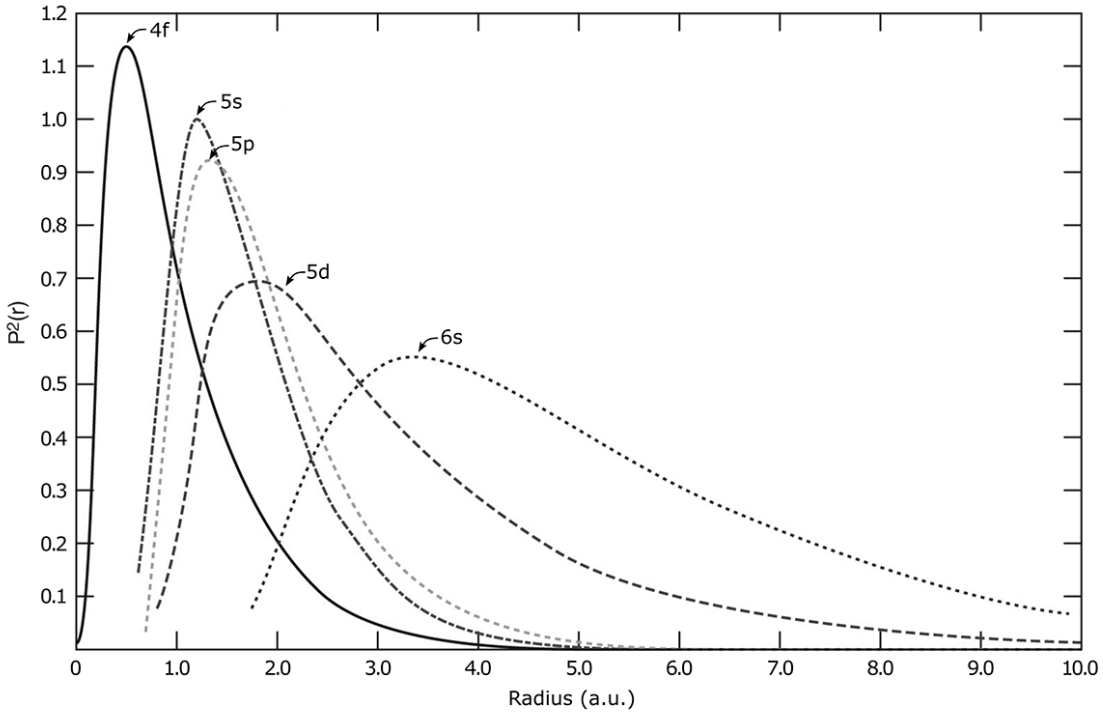

FIGURE 2.2: Radial probability function for $4f$, $5s$, $5p$, $5d$, $6s$ electron shells for gadolinium (Gd). The $4f$ shell is shielded against external electric fields by electrons in outer shells. Adapted from [73] after [74].

As a consequence of the screening provided by outer electron shells, a rare-earth ion can be said to behave in a manner similar to that of a free ion [38], [71]. While the luminescent peak may undergo varying degrees of broadening due to the influence of the host matrix, the rare-earth ions each exhibit characteristic emission wavelengths resulting from their $4f$ energy transitions. This consistent emission wavelength has been exploited for use in CRT phosphors to produce red, green, and blue light required for a full-colour display; solid-state lasers such as the Nd:YAG laser used in a wide variety of applications; and in telecommunications for long haul communication and chip-to-chip interconnects. The latter two technologies have focused on erbium (Er) ions in particular with an emission band around 1.53 µm.

Energy level diagrams for Er^{3+} and Tb^{3+} are shown in Fig. 2.3 along with select radiative transitions and lifetimes.

Under the static, free-ion, and single configuration approximations, the intensity of the transitions between $4f$ energy levels of the lanthanides in solids can be predicted through the Judd-Ofelt theory. The theoretical expression for line strength (i.e.: the square of the transition moment) is given by [77]–[79]:

$$S_{i\to f} = \sum_{\lambda=2,4,6} \Omega_\lambda |\langle 4f^n[SL]J||\boldsymbol{U}^{(\lambda)}||4f^n[S'L']J'\rangle|^2 \tag{2.1}$$

where Ω_λ are the *Judd-Ofelt parameters*. J and J' indicate the total angular momentum of the initial and final manifold, S and S' are the initial and final spin angular momentum, and L and L' are the initial and final orbital angular momentum. The terms in the brackets are doubly reduced matrix elements for intermediate coupling, referring to mutual repulsion interactions between $4f$ electrons when these are the same order of magnitude as the spin-orbit coupling. These matrix elements are integrals of the dipole operator between the upper and lower wavefunctions of the transitions. The $\boldsymbol{U}^{(\lambda)}$ terms are irreducible tensor forms of the dipole operator, where during the transition, the atom can be described as an electric dipole oscillating at some frequency [77]. The oscillator strength for an electric dipole transition can be written as:

$$f_{i\to f} = \frac{8\pi^2 mc}{3h\bar{\lambda}(2J+1)} n \left(\frac{n^2+2}{3n}\right)^2 S_{i\to f} \tag{2.2}$$

where m is the mass of the electron, c the speed of light in a vacuum, h is Planck's

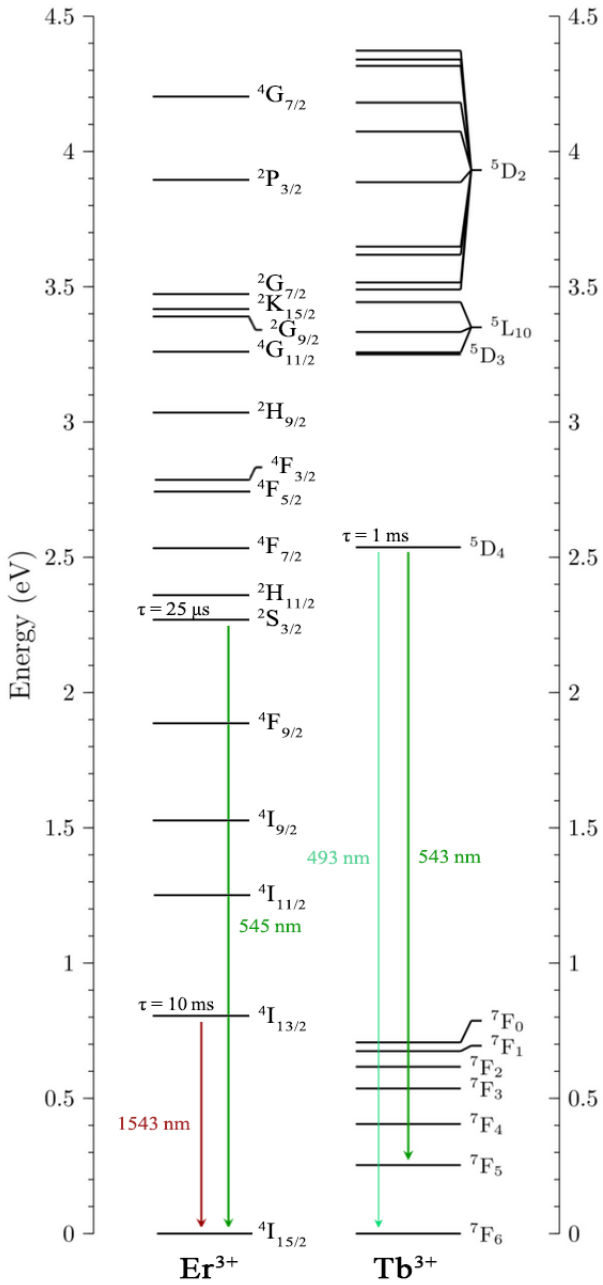

FIGURE 2.3: Schematic of 4*f* energy levels, with selected radiative transitions and relevant lifetimes for trivalent erbium and terbium. The energy in eV is relative to the ground state. Er^{3+} is primary used as an infrared emitter while Tb^{3+} is primary used as a green emitter. Adapted from [76] after [71].

constant, n the refractive index of the host matrix, at the average transition wavelength, $\overline{\lambda}$, and J is the total angular momentum of the initial upper excited state.

The Judd-Ofelt theory provides a method for the calculation of manifold to manifold transition probabilities; from this, the radiative lifetimes and branching ratios of emission can be determined. This determination requires accurate absorption measurements of the integrated absorption cross-section. The line strength can be found experimentally from the integrated absorption cross-section [77]:

$$S_m = \frac{3hc(2J+1)}{8\pi^3 e^2 \overline{\lambda}} n \left(\frac{3}{n^2+2}\right)^2 \int \sigma_{ab}(\lambda) d\lambda \tag{2.3}$$

where e is the elementary charge, J is the total angular momentum of the initial ground state manifold, and $\sigma_{ab}(\lambda)$ is the absorption cross-section as a function of wavelength.

The measured emission cross section for an isotropic host matrix is given by the equation,

$$\sigma_{em}(\lambda) = \frac{\lambda^5}{8\pi c n^2 (\tau_r/\beta)} \frac{I(\lambda)}{\int I(\lambda)\lambda d\lambda} \tag{2.4}$$

where $I(\lambda)$ is the wavelength dependent emission intensity, τ_r is the intrinsic radiative lifetime and β is the branching ratio. The emission cross section is related to the absorption cross section through a relationship which is was initially derived by McCumber [80] and reformulated in Payne et al. [81]. By scaling τ_r/β in Equation 2.4 such that the calculated and measured emission cross section agree, the lifetime can be determined provided one knows the branching ratio. Lifetimes

determined through Judd-Ofelt theory are usually accurate within 15% which is an illustration of the theory's predictive power [77].

In part, the success of many light-emitting devices is determined by achieving desirable lifetimes for a given excited state. For instance, in lasing applications, the excited states' lifetimes should be relatively long, and the ground state's relatively short. These lifetimes, τ, are composed of two components: an intrinsic radiative lifetime, τ_r, and nonradiative lifetime, τ_{nr} [82]:

$$\frac{1}{\tau} = \frac{1}{\tau_r} + \frac{1}{\tau_{nr}}. \tag{2.5}$$

The radiative lifetimes are influenced by the host material's local crystal symmetry at the rare-earth site. As will be discussed, nonradiative lifetimes are influenced by the vibrational density of states and other quenching effects. These nonradiative processes are undesirable for amplification, because they depopulate excited states and make it more challenging to achieve population inversion [82].

There are many limiting factors, which often result in suppressed luminescent efficiency, to consider when incorporating rare-earths into a host matrix. One of the most significant factors is multiphonon relaxation. This process competes with radiative decay, in which multiple phonons are emitted via an electron transition to a lower energy state from a higher energy manifold. The rate at which this occurs is material and temperature-dependent and can be given by the simplified expression [83]:

$$W_{NR} = B \exp\left(\alpha \Delta E\right) \left[1 - \exp\left(-h\nu_{max}/kT\right)\right]^{-p} \tag{2.6}$$

where k is Boltzmann's constant, $h\nu_{max}$ is the maximum phonon energy, ΔE is the energy gap between the two participating energy levels, and p is the number of phonons required to bridge the energy gap. Both α and B are coefficients dependent on the host matrix and can be found reported in tables [83]–[85]. This dependence on material properties highlights the importance of the selection of host material, as certain desired radiative transitions may be incompatible with a specific host.

There exists a critical concentration for rare-earth ions in a host matrix beyond which precipitates begin to form. These can exist as clusters of rare-earth ions, or as compounds or alloys formed from a component of the host matrix. These precipitates quench the luminescence through ion-ion interactions or the formation of non-optically active states. In this case, ion-ion interactions can occur between the same types of rare-earth ion or between different rare-earth ions [38]. These processes, including co-operative upconversion, energy migration, and cross-relaxation are depicted in Fig. 2.4 - for the case of terbium.

Two interacting ions can undergo co-operative upconversion. An ion in a meta-stable state can decay to the ground state. If it interacts with the second ion in a meta-stable state, it can transfer its energy and promote the second ion into a higher state. The second ion may then decay through non-radiative processes and lose its energy in the form of heat, as is common in glass materials, or return to its initial meta-stable state and undergo radiative decay. Furthermore, an ion in a metastable state can decay to the ground state through energy transfer to a secondary ion, promoting it from a ground state to a metastable state. This energy migration can lead to an increased probability of non-radiative decay for each instance of energy transfer. Moreover, cross-relaxation is a process where an ion in

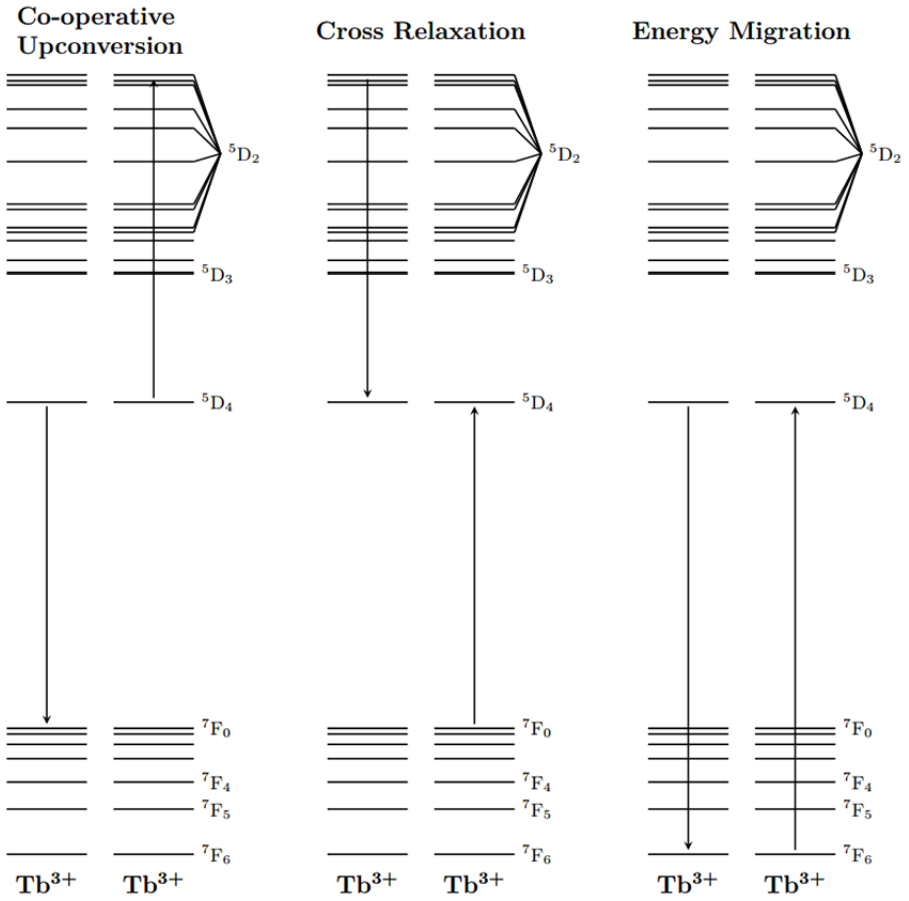

FIGURE 2.4: Ion-ion interactions between neighboring Tb^{3+} ion. Taken from [76].

a highly excited state can decay to a metastable state, promoting a nearby ion from the ground state to a metastable state. These processes are strongly dependent on the number of ions that exist in metastable states within close proximity, thus are dependent on the concentration and the excitation intensity [38].

Provided a long enough excited-state lifetime, a photon with the correct energy may interact with an ion in a metastable state, exciting it to a higher energy state, through a process referred to as excited-state absorption. The ion can return to a metastable state through multiphonon relaxation or radiative decay. This transition

will result in the loss of a photon through heat or photon emission with the incorrect wavelength from the metastable-to-ground state radiative decay. This process is detrimental in material systems designed for light emission and amplification due to the loss of a photon at the desired wavelength [38].

2.2 Rare-earth incorporation in silicon

Silicon is the semiconductor of choice for microelectronics. The success of achieving efficient light emission from rare-earths embedded within it would be significant. Presently the rare-earth ion with the greatest interest for inclusion is Er due to its emission at 1.5 µm allowing for operation at desirable telecommunications wavelengths. Erbium also possesses a relatively large absorption cross-section when incorporated into crystalline silicon. Once incorporated, the ion can be excited via direct optical or carrier-mediated excitation [38]. Means of incorporation can include ion implantation of high-quality bulk silicon or fabrication using metal-organic chemical vapour deposition (CVD) [86]. There are, however, many drawbacks which prevent silicon from being a suitable host. Strong non-radiative coupling between the erbium ion and host at room temperature makes it difficult to obtain luminescence [38]. The non-radiative decay rates are high, in the microseconds, compared to the radiative rates, in the millisecond [87]. Furthermore, crystalline silicon has low rare-earth solubility leading to clustering and increased ion-ion interactions [88], [89]. This solubility can be improved through the utilization of an amorphous silicon matrix; however, many of the aforementioned challenges still apply.

2.3 Overview of rare-earth host materials in silicon photonics

While the materials presented in this section are by no means exhaustive, they cover the most relevant host matrices used in the field of silicon photonics with the omission of group IV oxides, which will be covered in Section 2.4.

Alumina (Al_2O_3) is a material with high rare-earth solubility and a high refractive index ($n = 1.64$), making it suitable as a waveguiding material capable of signal amplification. The high rare-earth solubility of alumina is attributed to rare-earth valance matching allowing easy substitution into Al^{3+} cation sites. Additionally, one-third of Al^{3+} sites are unoccupied in the amorphous Al_2O_3 matrix, allowing for these sites to be filled with Er^{3+} ions without the detriments of pair-induced quenching [38], [90]. Furthermore, the emission linewidths in Er due to crystal field splitting in Al_2O_3 are up to 55 nm, about five times greater than that of silica, making it a suitable material system for wavelength-division multiplexing (WDM) applications [91].

Recently, an Er-doped Al_2O_3 distributed feedback laser with 75 mW of on-chip lasing at 1563 nm was produced [92], which utilizes a complementary metal-oxide-semiconductor (CMOS) compatible process through the fabrication and patterning of silicon nitride (Si_3N_4) waveguides and cavities on which the doped Al_2O_3 layer is deposited. These innovations have been further advanced through the development of integrated tunable lasers [93], and data links leveraging the Er-doped Al_2O_3 lasers [94]. Due to alumina's transparency over silicon at lower wavelengths, it can be used as a guiding material in the place of silicon and can be co-doped with

ytterbium, which aids with the sensitization of Er with its broad absorption band between 800 and 1080 nm [38].

Tellurium oxide (TeO_2) is a material with high refractive index ($n = 2.08$) suitable for silicon photonics platforms [95]. It is transparent over a wide wavelength range and possesses low phonon cutoff energies (750 cm^{-1}) [38]. It has been reported that that erbium ions exhibit high rates of radiative transitions when incorporated [96] making the material well suited for amplifiers or lasers. Furthermore, high rare-earth solubility of up to 3.5 at. % has been shown [97]. Recently, 5 dB of net gain has been shown in Er-doped TeO_2 coated Si_3N_4 waveguides [98]. The material is also reported as having a wide gain flattened bandwidth, making them a useful candidate for WDM systems. The low phonon cut-off energy makes the material promising for mid-infrared applications, including 2-µm-band amplifications, with recent developments in Tm-doped TeO_2 waveguide amplifiers achieving 7.6 dB of net gain [99]. Although these materials are highly promising for hybrid waveguide structures fabricated using post-processing steps, standard materials compatible with silicon foundry processing are also of interest.

2.4 Group IV oxides as hosts

Host materials compatible with silicon foundry processes offer reduced complexity of manufacturing wavguide structures compared to materials that require post-fabrication deposition. Group IV materials are foundry compatible, making them promising candidates as rare-earth hosts.

Silica

Silica has been extensively used as a host for rare-earth incorporation in the telecommunications industry. Fibre optic cables, doped with Er ions are used for signal amplification over long distances. Perhaps one of the most significant limitations of this material system is the modest solubility of trivalent rare-earth-dopants in silica. Precipitates form in melt glass at 0.1 at.% incorporation, in the case of Er^{3+} this results in interaction between ions leading to the rapid non-radiative decay of the $^4I_{l3/2}$ metastable state, resulting in quenching [38]. As a result, optical amplifiers require long lengths of lightly doped fibre to achieve significant amplification. This makes it challenging to produce compact devices on a chip as the low concentrations will require long structures to obtain significant amplification. This low solubility, in part, can be addressed through low-temperature deposition systems such as plasma enhanced chemical vapour deposition (PECVD) techniques, which have been reported to raise the solubility of erbium in silica by an order of magnitude [100]. This higher solubility is attributed to the low diffusion of the dopant ions in the matrix at low deposition temperatures.

Germania

Amorphous germanium oxide (GeO_2) is structurally very similar to amorphous silicon dioxide (SiO_2). Both are very good glass-forming materials, and exhibit tetrahedral structures with the group IV atom connected to four oxygen atoms, forming flexible bridging bonds (Ge – O – Ge) [101]. GeO_2 benefits from having a moderately high refractive index ($n = 1.64$), making it suitable for photonics applications as a waveguide core or cladding. It possesses a wide transparency

region and a lower phonon energy (820 cm^{-1}) than SiO_2 [102], [103]. For these reasons, it is widely used in SiO_2 fibre fabrication as a means to increase the refractive index and lower the phonon energy. Much of the research into this material has been as in the form of multicomponent glasses incorporating materials such as lead oxide, sodium oxide, gallium oxide, and bismuth oxide, which allow for higher refractive indexes and lower phonon cutoff energies. These material systems, with the inclusion of rare-earth dopants, have also seen some recent success with optical signal enhancements. Relative gains of 4.5 dB/cm were seen in Tm^{3+} doped germania bismuth oxide glasses at 1470 nm ($^3H_4 \rightarrow {}^3F_4$) [104].

2.5 Thin-film deposition techniques

This section serves as a brief overview of the most common methods of depositing dielectric thin films and incorporating rare-earths into these hosts. For this reason, group IV materials are of interest.

2.5.1 Plasma enhanced chemical vapour deposition

CVD is a technique that, in broadest terms, can be described as a process that produces a solid thin film on a heated surface through a chemical reaction of a singular or multiple precursors introduced into the reaction chamber in a vapour phase. It presents many advantages compared to other deposition techniques due to its conformal deposition overtop of 3D structures and high deposition rates [105]. There are many types of CVD processes based around the activation mechanism (hot wire CVD [106], laser CVD [107] and plasma enhanced CVD [108]), experimental condition (low pressure CVD [109] and atmospheric pressure CVD [110]), or type

of precursor used (direct liquid injection CVD [111] and metal organic CVD [112]) [113].

A low-temperature CVD deposition may be desirable to limit stress formation, reduce diffusion rates between the substrate and film, and damage to devices and structures. In this case, a plasma source would be used to provide additional energy to the substrate to compensate for the lower deposition temperature, resulting in a plasma-assisted or plasma enhanced chemical vapour deposition (PECVD) [113]. The highly energetic electrons present in the plasma partially dissociate and ionize the gas precursors to form chemically reactive ions. The result is a nearly electrically neutral plasma which contains some positively charged species and negatively charged electrons amongst a mostly neutral molecular gas precursor. It is the ions and molecules in the plasma discharge, which undergo interaction with the substrate to create an environment where chemical reactions take place, leading to film growth [114]. These chemical reactions are often incredibly complex, with the simple formation of SiO_2 using silane (SiH_4) and O_2/Ar plasma comprising of hundreds of gas-phase reactions between ions, neutral radicals, and electrons in addition to dozens of surface mechanisms from deposition, oxidation, and dissociation [115].

The integration of rare-earth-dopants into the film during a deposition in a PECVD plasma can be finely controlled through the introduction of metal-organic compounds through an inert carrier gas. In these instances, the metal-organics are typically β-diketonates, which are comprised of a single rare-earth atom at the center of a complex set of carbon, oxygen, and hydrogen ligands. The plasma cracks the precursors and the rare-earth is incorporated into the host. PECVD

techniques are often employed for silicon-based materials as they offer precise control and higher quality films than what can be generated through a physical vapour deposition technique.

2.5.2 Electron-beam evaporation

Electron-beam evaporation is a physical vapour deposition (PVD) process that uses a beam of electrons produced by an anode and focused with a magnetic field to heat solids in a crucible under ultra high vacuum (UHV) conditions. These solids undergo evaporation or sublimation under the extreme temperatures of the electron beam as it sweeps over the solids. These evaporated materials then condense onto the substrate, typically placed on a rotating or planetary stage. Reactive gases can be introduced into the chamber to produce a greater diversity of thin-film materials. E-beam evaporation benefits from the broad range of deposition rates it can produce by varying the beam current and can achieve rates in the 100 nm/min range. It struggles, however, with materials with very high melting points, where these would be more suitable in a sputtering system. Multilayer Al-Tb/SiO_2 devices have been recently fabricated through e-beam evaporation [116], [117] to produce green light-emitting devices under electroluminescent conditions.

2.5.3 Sputtering

Sputtering is a physical vapour deposition process that produces solid thin films through the kinetic bombardment of atoms onto a material substrate. Standard sputtering uses a target of pure material and an inert gas, typically Ar. The sputtering head and target act as a cathode, which electrically energizes the gas

to create a plasma. This may be done through the application of DC, AC or RF power, the latter typically operating at 13.56 MHz. The atoms in the gas will lose electrons to the plasma. These positively charged ions under the influence of the electric field generated by the cathode will accelerate into the target. The kinetic energy of these ions will dislodge the atoms in the target and traverse the chamber in a stream depositing themselves onto the sample [118].

Reactive sputtering distinguishes itself from standard sputtering in that it utilizes non-inert gases in place of or in addition to inert gases. The ionized chemically non-inert gas reacts with the stream of target atoms to produce a molecular compound. This process is applied in the deposition of SiO_2 thin films where a pure Si target is sputtered in a reactive oxygen (O_2) environment. The deposition is controlled by adjusting system variables such as substrate heater temperature, chamber pressure, gas partial pressure, and power to the targets [119]. Sputtering is a versatile deposition technique in which the complexity of a thin film can be increased by merely adding targets to the system. Furthermore, sputtering is considered a much safer process for the production of certain films as dangerous gas precursors can be avoided, such as silane, germane and ammonia. A typical modern sputtering process will often employ a magnetron to confine electrons above the sputtering target using a magnetic field. Magnets are placed behind the cathode to generate the magnetic field normal to the cathode's electric field. The confined electrons improve the efficiency of gas ion formation due to their high density, and the magnetic field constrains the discharge plasma [120]. This allows for the sputtering to occur at lower pressures and consequently allows for a much higher deposition rate. The high-quality films produced through reactive sputtering make

for promising rare-earth-doped material candidates for optoelectronic applications, such as Al_2O_3 [121], TeO_2 [122] and CdO [123].

2.5.4 Ion implantation

Ion implantation is a post-deposition processing technique in which ions are accelerated into the subsurface region of a solid target, changing its chemical, electrical, or physical properties. Atoms of the desired element are ionized and accelerated electrostatically. By knowing the mass to charge ratio, ion energies can be selected using a magnetic chamber in which they are accelerated towards the target where they come to rest at a point. The position of the beam can be scanned along the surface to select specific regions of the target, whereas the depth of the ion implantation is stochastic, influenced by the energy of the ion, its mass and the target material. Ion implantation is most commonly used in the semiconductor industry for introducing impurities into semiconductors to form devices due to its precise control over doping concentrations. These characteristics are also valuable for creating light-emitting devices by precisely introducing rare-earth dopants into films or micro-structures, such as the fabrication of Er doped silica microsphere lasers [124], or more recently, the doping of thin-film lithium niobate ring structures with Er ions, with Q-factors on the order of 1×10^6 after annealing, for their integration into silicon photonics [125].

2.6 Systems utilized in thesis

2.6.1 Electron cyclotron resonance PECVD

Electron cyclotron resonance (ECR)-plasma enhanced chemical vapour deposition (PECVD) is a technique that allows for a high power density in the plasma, which contributes to a higher degree of dissociation of the precursor gasses. These conditions are met while maintaining low chamber pressures (<10 mTorr) and limiting high energy energetic ions and radicals through the use of a remote plasma in a separate plasma chamber. The chamber, referred to as the ECR chamber, features a strong magnetic field produced through solenoid coils in which microwaves are introduced via a waveguide. The role of the ECR chamber is to couple the microwave power to the plasma. The plasma is discharged when the electron cyclotron frequency matches the microwave frequency. This condition is satisfied in a surface layer or volume of the ECR chamber known as the ECR zone delimited by the static magnetic field that meets the conditions mentioned earlier. The excited plasma electrons collide with neutral particles resulting in ionization and further plasma generation [126]. The magnetic field required to satisfy the ECR resonance condition is obtained from the equation for a simple harmonic oscillator at the cyclotron frequency [127]:

$$B = \frac{\omega_c m_e}{q} \tag{2.7}$$

where ω_c is the microwave angular frequency, m_e is mass of the electron, q is the fundamental electronic charge. It is typical to use a 2.45 GHz microwave source, so the magnetic field strength where ECR resonance occurs is 875 G. The magnetic field inside the ECR chamber confines the plasma radially. As the magnetic field

decreases upon the exit of the ECR chamber, the plasma will diffuse along the divergent magnetic field lines, and decrease in density [126].

Gasses are introduced to the chamber near a quartz window through which microwaves can pass. The confined ECR plasma allows for ion densities far in excess of what is achievable in a typical radio frequency (RF)-PECVD plasma, typically 100 times greater. The high fractional ion density combined with the low operating pressure allows for the creation of low energy ions, which limits damage to the film during film growth and limits the incorporation of hydrogen [128]. Such systems have been used to produce rare-earth-doped visible and infrared light emitting thin films [129]–[131].

2.6.2 Plasma assisted reactive magnetron sputtering

Plasma assisted reactive magnetron sputtering (PARMS) is an attractive fabrication technique for applications requiring low-loss thin films such as high-performance optical filters [132], [133] and dielectric mirrors for lasers [134]. The deposition technique can be described as the application of dual mid-frequency alternating current (AC) magnetron sputtering with partial pressure control of a reactive gas and reactive ion assistance to the process through an RF plasma source. Mid-frequency AC magnetron sputtering utilizes two cathodes with an AC current that switch back and forth. This allows for the target surface to reduce charge build-up on dielectrics, which can lead to arcing and expulsion of material droplets, which can reduce film uniformity [135]. Moreover, the use of RF plasma assistance is an important detail. In a process that does not use plasma assistance, the substrate's thermochemistry, film materials, and temperature primarily govern nucleation

modality and film growth [136]. The addition of a plasma and ion assistance provides additional energy to surface atoms, providing them with higher surface mobility to more readily find energetically preferred locations. This additional energy assists in the desorption of weakly bound surface atoms/molecules and increases film densification. The high-quality films produced through PARMS have been used for planar waveguide fabrication [137] and rare-earth-doped dielectric layers for upconversion laser waveguides [138].

Chapter 3

Methods of Sample Characterization

Preface

This chapter contains details on the sample characterization techniques and tools used throughout this thesis. Sample stoichiometry was determined through Rutherford backscattering spectrometry (RBS) and elastic recoil detection analysis (ERDA). This was important for the calibration process of the hybrid sputtering system. Sample thickness and refractive index measurements were performed through variable angle spectroscopic ellipsometry (VASE). This technique was also required to calibrate the recipes used on the thin film deposition systems in order to establish the growth rate and to understand how variations in the recipes used would affect the dispersion relation of the films grown. Given films measured in this thesis featured very low loss at longer wavelengths, it was necessary to use a prism coupler to extract optical attenuation values that would otherwise be too

low to be measured with VASE. The primary mode for film loss was thought to be light scattering at the material interface—this promoted investigation of surface roughness of the films via atomic force microscopy (AFM). Characterization of rare-earth emission was performed through the use of photoluminescence (PL) and was used to validate the successful incorporation of optically active rare-earth dopants. Increased emission at high annealing temperatures was thought to be caused by the formation of Si nanostructures and was investigated with the use of scanning electron microscopy (SEM) and transmission electron microscopy (TEM).

3.1 Rutherford backscattering spectrometry

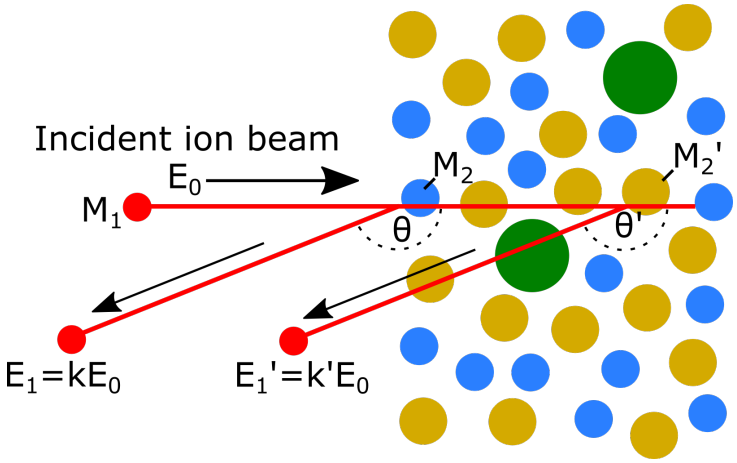

FIGURE 3.1: Schematic diagram of incident ion-beam interaction with atoms in the thin film during RBS. Ions are backscattered into the detector with energy equal to the product of the kinematic factor and initial ion energy.

Compositional analysis of deposited thin films can be obtained through high-energy ion scattering techniques, which include Rutherford backscattering spectrometry (RBS) and elastic recoil detection analysis (ERDA). These techniques employ high energy elastic scattering of charged ions off the sample through Coulomb

interactions. The atomic composition of a sample is determined from the reflected energy spectra of an ion beam source with known initial energy and scattering angles, as represented in Fig. 3.1. The relationship between the projectile's incident and scattered energies with respect to the scattering angle is expressed as the kinematic factor. The expression for the kinematic factor is given in the following equation and plotted in Fig. 3.2:

$$k = \frac{E_1}{E_0} = \left[\frac{(M_2^2 - M_1^2 \sin^2\theta)^{\frac{1}{2}} \pm M_1 \cos\theta}{M_1 + M_2} \right]^2 \tag{3.1}$$

where M_1 is the projectile mass, M_2 is the target nucleus mass, and θ is the scattering angle with respect to the initial propagation vector, E_0 is the incident projectile energy, and E_1 is the scattered projectile energy. Equation 3.1 has a *+ve* operator for the $\pm$ term under the condition that $M_2 > M_1$ and *-ve* operator for the opposite case.

The distribution of kinematic factors at large scattering angles for heavy atoms highlights a limitation of RBS. The resolution between elements decreases for higher Z elements. For films containing co-doped materials of heavy Z elements, there can be significant overlap in the signal from these elements, increasing the complexity of characterization. In Fig. 3.2, we see the kinematic factor as a function of scattering angle, θ for an incident helium ion ($^4He^+$). Lighter elements such as oxygen and carbon that are close to each other in the periodic table share a similar difference in kinematic factors as germanium and terbium, two heavier elements that are relatively distant in the periodic table, at large scattering angles.

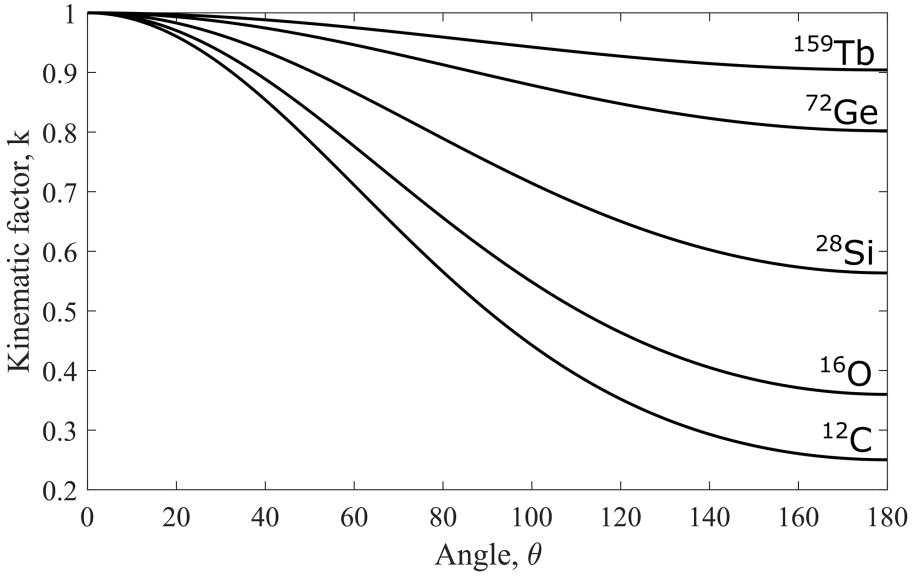

FIGURE 3.2: Kinematic factors of $^4He^+$ ion interacting with various isotopes as a function of scattering angle produced through Equation 3.1. As the mass of the target nucleus increases, the difference in kinematic factor for near elements in the periodic table decreases for large scattering angles.

The primary benefits provided by RBS are composition and depth profiling of individual elements with high sensitivity for heavy elements. This sensitivity to heavy elements is due to large Rutherford scattering cross-sections that heavier elements possess. This cross-section can be expressed by the following relationship:

$$\frac{d\sigma}{d\Omega} \equiv \sigma(\theta) = \left(\frac{Z_1 Z_2 e^2}{4E_0 \sin^2(\frac{\theta}{2})} \right)^2 \tag{3.2}$$

with Z_1 and Z_2 representing the atomic numbers of the incident and target ions, e is the elementary charge, Ω is the solid angle. Here we see that cross-section scales as a function of Z_2^2 assuming the scattering angle remains constant. This characteristic makes high precision measurements of lanthanides concentrations in

a matrix possible.

An energetic particle that moves through a medium loses energy through many individual scattering encounters. These encounters reduce the kinetic energy of the particle and result in a spread of beam energy. This is referred to as energy loss straggling and is a product of statistical scattering fluctuations of the energy transfer in the collision process [139]. The causes of the broadening and its effects will change for varying energy loss magnitudes and film thicknesses. These range from an increased number of collisions causing Gaussian distributions of particle energy to changes in stopping power of the charged particle as they slow down.

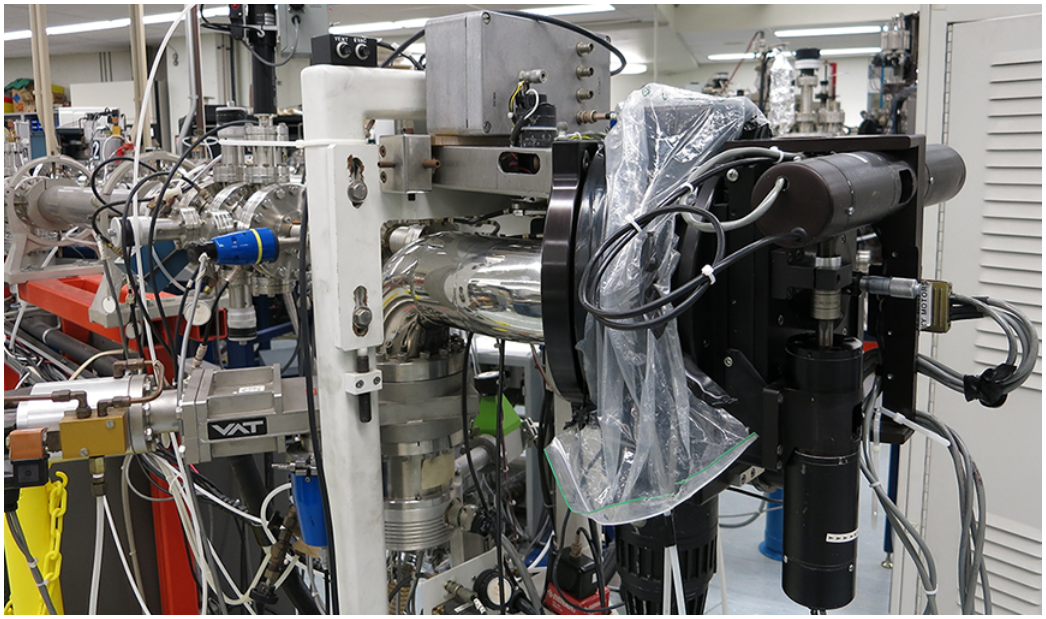

FIGURE 3.3: Ion scattering chamber used for RBS spectroscopy which houses a 4-axis manipulator. Sample alignment is performed with computer software. Image modified from [140].

RBS and ERDA measurements in this work were performed at the Tandetron Accelerator Laboratory at Western University, using the ion scattering chamber shown in Fig. 3.3. Measurements were carried out using a Cornell geometry with

a 2 µC to 4 µC dose utilizing 1.8 MeV $^4He^+$ ions with scattering angles, θ, of 5° from the surface normal. A reference sample of antimony doped silicon with known dopant concentration was measured at the start of each set of measurements. Samples deposited on crystalline substrates underwent random rotation during measurement in order to minimize the effects of substrate channelling. Carbon substrates were used during calibration of the electron cyclotron resonance (ECR)-plasma enhanced chemical vapour deposition (PECVD) system; these provide low background noise levels for elements heavier than carbon making it easy to obtain accurate fits of oxygen and silicon.

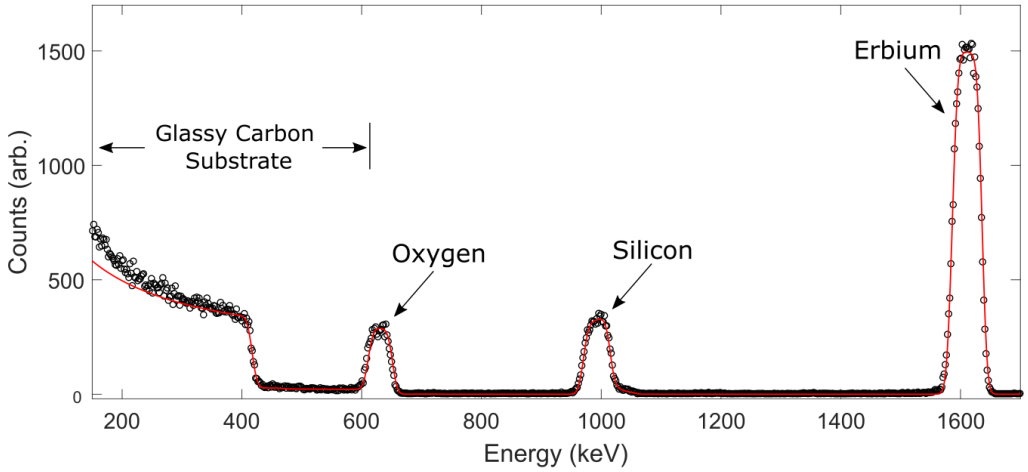

FIGURE 3.4: Experimental RBS data of sample E30 (circles) with the simulated spectrum (red line). Different scattering energies correspond to different elements.

The measured RBS spectra were fit using SIMNRA simulation software [141]. Simulated models were used to obtain the atomic concentration, except for hydrogen, as a function of depth. The simulation parameters used accounted for the natural abundance of elemental isotopes, dual scattering of incident ions utilizing Ziegler/Biersack stopping power data, Chu and Yang energy-loss straggling

model, and Anderson screening corrections to Rutherford cross-sections [141]. An example of this is provided in Fig. 3.4. An experimental RBS spectrum of an erbium (Er)-doped silicon dioxide (SiO_2) on glassy carbon substrate (Sample E30) is superimposed with the simulated spectrum. Further details of the composition of this sample are given in Table 5.1, Section 5.1. Here, individual energy peaks can be seen corresponding to separate elements. From the relations established by equation 3.1, we can determine the element that each peak represents based on the measured reflected energy. In this case, the peak around 1600 keV represents the erbium present in the sample. The signal from the erbium ions is about three times greater than that of silicon despite the concentration of erbium being five times less than silicon in this sample. This is expected due to the greater differential cross-section that erbium possesses relative to a lighter elements like silicon. The broad, smooth elemental peaks denote a uniform stoichiometry through the thickness of the film. At lower energies around 400 keV, a broad signal edge from multiple scattering events in the carbon substrate can be observed. We can also observe the heavy concentration of oxygen present in the substrate from a broad background signal below 600 keV. It can be observed that the light elements that compose the substrate allow for a clear resolution of the silicon and oxygen in the thin film.

Overlapping elemental signals highlights the importance of the substrate in these measurements. Substrates composed of heavier elements will impose a background signal overtop of lighter elements. The overlap can be especially problematic when the substrate is crystalline as channelling effects from the crystal lattice become unavoidable. Not only does this add background signal overtop elemental peaks of

lighter elements, but it reduces the expected signal from the substrate. The low substrate signal requires an artificial reduction in the substrate density in the model to correct, which is achieved by substituting hydrogen into it. Polycrystalline or amorphous substrates can be desirable as these will not suffer from channelling effects.

It is also worth drawing attention to the divergence from the simulated and experimental RBS spectra in Fig. 3.4. It is often the case at low backscattered energies that the simulated spectra will underestimate the experimental spectra. This deviation arises from the limited number of scattering events the simulation software will simulate in the substrate. As ions travel deep within the sample, there is an increased probability that the ions that have been scattered back into the detector will have undergone multiple scattering events. Each of these scattering events will deposit some energy into the film/substrate. This energy loss is the reason behind the peak broadening seen for each element – broader peaks imply a thicker film. The substrate is many orders of magnitude thicker than the thin film, and for the simulation, it can be considered infinitely thick. It is the case that as the incident ions travel deeper within the film, they will undergo more scattering events than the maximum limit of the simulation software resulting in a bias towards a smaller simulated signal.

3.2 Ellipsometry

Variable angle spectroscopic ellipsometry (VASE) provides a noncontact non-destructive way to characterize thin films. Ellipsometry has gained significant popularity in thin film analysis due to the range of materials it can characterize.

Modern instruments can cover optical ranges from the ultraviolet to the mid-infrared by combining multiple optical sources and detector types [142]. Through model-based regression, the refractive index, thickness, surface roughness, alloy composition, doping concentration, optical anisotropy, and composition gradient of a film can be determined [143]. Its high precision and rapid data acquisition have made it popular in a wide range of research fields.

Spectroscopic ellipsometry measures the change in polarization of light reflected (or transmitted) off a medium. The measurements obtained are described by Ψ and Δ, which represent amplitude and phase change of the Fresnel coefficients, as seen in Equation 3.3:

$$\rho \equiv \tan(\Psi)e^{i\Delta} = \frac{r_p}{r_s} \tag{3.3}$$

where r_p and r_s are the Fresnel reflection coefficients for parallel and perpendicular (senkrecht in German) polarization components with respect to the incident plane. The measurement is typically selected around the Brewster's angle as this provides the greatest ratio between r_p and r_s, increasing the sensitivity of the measurement.

Variation in the angle of incidence of light serves to change the path length through a material. The inclusion of multiple angles increases the information available. This information, however, may not be unique; an accurate model, after all, will describe the light-film interactions for all angles. The benefits obtained from multiple measurements using varying angles come from the analysis of semi-absorbing films, multilayer structures, and anisotropic materials [142]. For these

materials varying path lengths or interactions along different optical axes can supply new information to be characterized. The material properties of these thin films can then be determined through model-based regression.

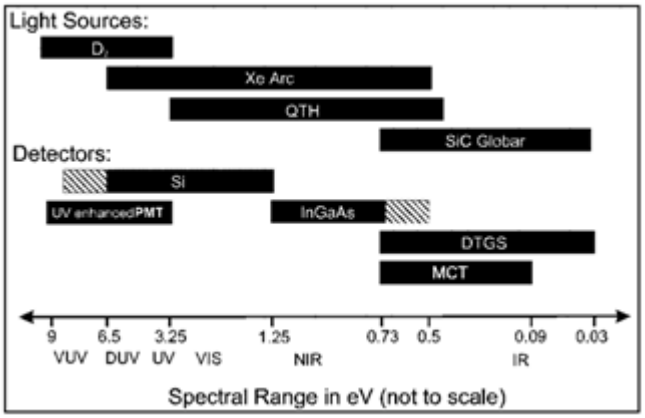

FIGURE 3.5: Wavelength ranges for common light sources and detectors used in spectroscopic ellipsometry [142].
*deuterium arc lamp (D2), quartz tungsten halogen (QTH), deuterated triglycine sulphate detector (DTGS), mercury cadmium telluride (MCT)

Spectroscopic measurements provide new information for each wavelength as the dispersion relation for the material will change across the measured spectrum. Conventional spectroscopic ellipsometry development focuses on expanding acquisition times for data as well as expanding the range of wavelengths from vacuum ultraviolet (VUV) to the near-infrared (NIR). It is often achieved by combining multiple sources and detectors in a single instrument, as seen in Fig. 3.5. To take a spectroscopic measurement, light enters the detector through an entrance slit. It is reflected off a holographic grating onto a photodiode array allowing for simultaneous acquisition of all wavelengths with a dramatically reduced measurement time. This measurement technique is contrasted with older methods of wavelength-by-wavelength steps with a monochromator, which could take up to several minutes per measurement.

Ellipsometry requires specific optical elements to measure polarized light. These elements are classified as polarizers (analyzers), compensators (retarders), and depolarizers. A polarizer serves to convert unpolarised light into polarized light. These are typically placed right after the light source, or in the case of an analyzer, placed in front of the detector. The analyzer will attenuate a polarized light source depending on its relative polarization axis. The compensator's purpose is to convert linearly polarized light into circularly polarized light and achieves this by using materials with a fast and slow optical axis. The depolarizer converts polarized light into unpolarised light. Many light sources will not emit perfectly unpolarised light. A depolarizer is used to remove any polarization bias that may be present in a source.

A schematic of a polariser - rotating compensator - sample - analyser (PC_RSA) ellipsometer is shown in Fig. 3.6. The advantages that a rotating compensator ellipsometer provides is that it can measure the degree of depolarization of the sample for each wavelength and provide reliable measurements if the light incident on the samples becomes depolarized. It also provides uniform measurement sensitivity for Ψ and Δ across its spectroscopic measurement range. However, the drawback is that these systems have complicated optical configurations, which makes calibration more challenging.

It is impossible to discuss ellipsometry without discussing modelling. The development of models is perhaps one of the most important steps in ellipsometry. Data acquisition through ellipsometric techniques does not, on its own, provide any interpretive data. In order to extract meaningful parameters such as refractive index and thickness, a model must be appropriately fitted to the data. Many

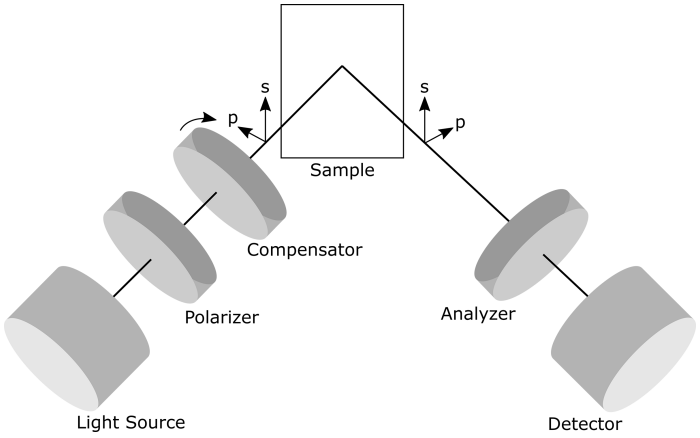

FIGURE 3.6: Schematic diagram of a PC_RSA VASE. Light from the light source becomes linearly polarized as it passes through the polarizer with s- and p-components.

dielectric function models can be applied to a set of data, and it is important to know which models are appropriate for a given set of materials. For materials that are transparent in the region of the light used, then the Sellmeier or Cauchy models are used. Where free carrier absorption occurs, the Drude model is preferred. In cases of electric polarization in the visible/UV, the Lorentz model, the Tauc-Lorentz model, harmonic oscillator approximation, and model dielectric function can be used [144].

The Lorentz oscillator model treats the electron and nucleus as if they were connected by a spring. The nucleus is assumed to have an infinite mass compared to the electron and does not move. The assumption is that this binding force can be modelled by a spring, and is reasonable given a small enough displacement. The Lorentz Oscillator model can be expressed with the following set of equations for both real, ϵ_1, and imaginary, ϵ_2, components of the dielectric function:

$$\epsilon_1 = 1 + \frac{\omega_p^2(\omega_0 - \omega)}{(\omega_0^2 - \omega^2)^2 + \omega^2\gamma^2} \tag{3.4}$$

$$\epsilon_2 = \frac{\omega_p^2\gamma\omega}{(\omega_0^2 - \omega^2)^2 + \omega^2\gamma^2} \tag{3.5}$$

where ω is the angular frequency of the time-varying electric field driving the oscillator, ω_0 is the resonance angular frequency of the oscillator, ω_p is the plasma angular frequency of the material, γ is the dampening rate. Further details regarding the derivation can be found in [145].

The Tauc-Lorentz model is primarily used to look at amorphous materials; however, it can also be applied to the modelling of transparent conductive oxides. For the Lorentz Oscillator model, the shape of the imaginary dielectric function component is symmetrical. This symmetry, however, is not present for the imaginary dielectric component of amorphous materials. The Tauc-Lorentz is asymmetric in this regard and can provide a better fit for these materials.

For transparent regions of the Lorentz oscillator, where $\epsilon_2 \approx 0$, the Sellmeier model can be used as an approximation. Equation 3.6 gives the relation for this model:

$$\epsilon_1 = A_1 + \sum_j \frac{B_{1j}\lambda^2}{\lambda^2 - C_{1j}}, \quad \epsilon_2 = 0 \tag{3.6}$$

where A_1, B_{1j}, and C_{1j} are Sellmeier coefficients, and λ is wavelength. The Cauchy model is similar to the Sellmeier model in that it requires the film to be transparent. It is, however, only approximately accurate in the visible spectrum. The Sellmeier

model more accurately models the refractive index in the ultraviolet, visible and infrared regions. The Cauchy equation is given by:

$$n = A_2 + \frac{B_2}{\lambda^2} + \frac{C_2}{\lambda^4} + ..., \quad k = 0 \tag{3.7}$$

where A_2, B_2, and C_2 are Cauchy coefficients. The refractive index, n, and the extinction coefficient, k, are related to the dielectric function, $(n + ik)^2 = \epsilon_1 + i\epsilon_2$. These are fitted using the experimental data. It is important to note that both the Cauchy and Sellmeier model do not follow the Kramers-Kronig relations since the real component of the dielectric function is obtained through the assumption that the imaginary component is equal to zero [144].

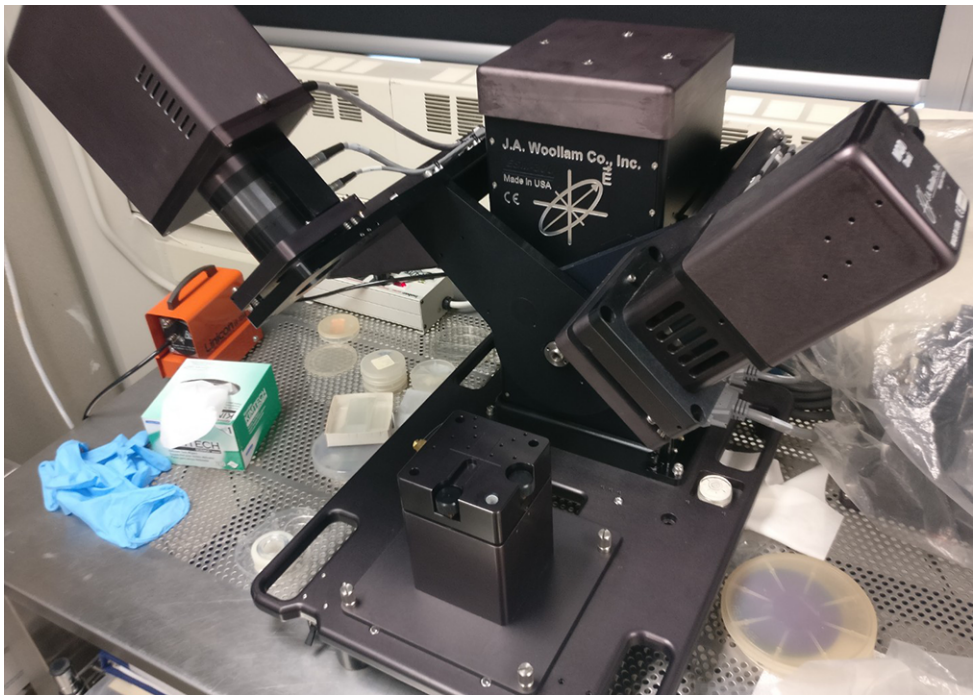

FIGURE 3.7: Photograph of the J. A. Woollam M-2000 VASE instrument.

VASE measurements in this work were conducted using a J. A. Woollam M-2000, a PC_RSA ellipsometer, seen in Fig. 3.7, operating from 245 to 1690 nm with spectra collected at multiple angles of incidence (55°, 60°, 65°, 70° and 75°) to the surface normal. The modelling was performed using J. A. Woollam's CompleteEASE™ software package [146]. For transparent materials, Cauchy and Sellmeier fits were used. For lossy films, a B-spline layer was fit over higher wavelengths of the film. Using the wavelength range expansion fit with an increment of 0.2 eV, the B-spline layer was expanded down to 245 nm. The layer was then parametrized as a Tauc-Lorentz oscillator with the oscillator's imaginary component being fit first and the real part being fit second. For films deposited on silicon, a standard silicon model was used as the substrate, while a uniaxial anisotropic Cauchy model was applied to quartz substrate films to account for the ordinary and extraordinary directions. Single-side polished silicon was preferred over dual-side polished as it scatters reflections off the backside of the substrate. In the same vein, Scotch® tape was used on the backside of quartz as it shares a similar refractive index and scatters reflections off the backside.

3.3 Atomic force microscopy

Atomic force microscopy (AFM) is a local characterization technique that rasterizes a sharp tip across a surface in order to obtain a three-dimensional (3D) surface topography. Conceptually, each interaction between the probe tip and the material surface can be thought of as an individual local experiment that is compiled together to form an image reconstruction of the scanned surface. The operational modes of an AFM can be broken down into three distinguishing types: static mode, also

referred to as DC mode; amplitude modulated (AM) mode, also referred to as intermittent or tapping mode; and frequency modulated (FM) mode, also referred to as noncontact mode [147]. The work in this thesis was performed using tapping mode AFM; as such, it will be the only one discussed further.

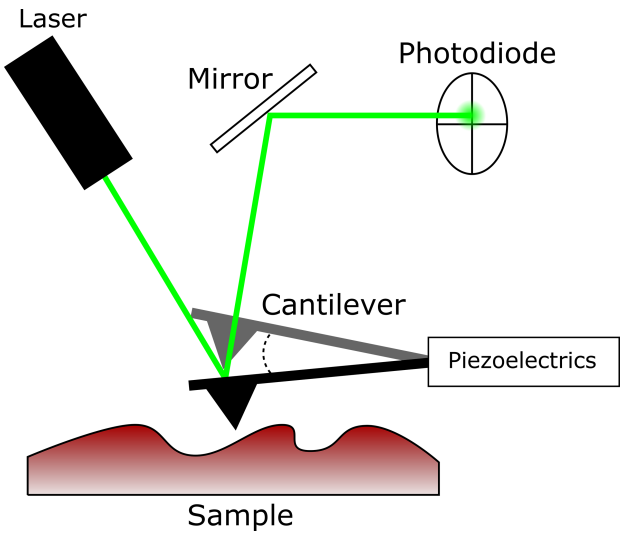

FIGURE 3.8: Schematic diagram of the AFM apparatus. Cantilever deflection is measured through laser reflection off the back of the cantilever into a segmented photodiode.

Tapping mode force microscopy requires the sinusoidal excitation of the cantilever near its resonant frequency. The probe is excited through a piezoelectric plate or actuator. It provides advantages over direct current (DC) mode force microscopy in that it is mostly non-destructive. With reference to Fig. 3.8, a laser is reflected off the back of the cantilever onto a segmented photodiode. The laser beam is assumed to have a Gaussian distribution intensity profile with a characteristic spot diameter. The segmented photodiode generates a current proportional to the flux density of the laser. It thus can measure the deflection of the cantilever based on the change in flux density incident on the photodiode segments. The cantilever and sample surface experience varying force interactions when in proximity to each other. Of

these interactions, van der Waals (vdW) interactions are considered long-range interactions and scale with the inverse square of the separation between a point and a flat surface. These interactions lead to a negative interaction potential, which results in attraction. If the electronic wave function of the outermost atom of the probe and sample begin to overlap, short-range repulsive forces begin to dominate [148].

The vertical resolution for a commercial AFM is considered sub-Ångstrom (0.1 nm) and is primarily limited by the thermal noise of the deflection system. The lateral resolution is primarily limited by the sharpness of the tip. The tip's diameter and shape will interact with surface features. As a consequence, it is expected that the image produced will show topographic features convolved with the volume of the tip. This effect is especially noticeable if the tip is damaged or dirty [147]. A scanned AFM image will exhibit artifacts of odd repeating geometric shapes that appear over every surface feature - all lined up with the same orientation. It is perhaps sufficient to say that the lateral resolution of an AFM image will be orders of magnitude higher than the vertical resolution.

Surface roughness in this thesis is reported as root mean squared (RMS) roughness. It represents the standard deviation of the distribution of surface heights and is used to quantify roughness statistically. It is an alternative to the average arithmetic height, which is the most universally used roughness parameter. RMS roughness may be chosen as the characterization parameter as it is more sensitive to significant deviations from the mean [149]. It can be obtained from the experimental 3D amplitude profile taken by the AFM.

AFM measurements in this work were performed on an Asylum MFP-3D instrument in tapping mode under ambient environmental conditions. The AFM images were processed with WSxM [150], a freeware scanning probe microscopy software based on MS-Windows. Monolithic silicon probe tips from Oxford instruments (NCHR) with a 4-sided polygon based pyramid tip with a length of 15 µm, tip radius of less than 8 nm, a front angle of 25° and a back angle of 15° were used. The cantilevers featured aluminum coatings to improve laser reflectance and had a stiffness of 60 N/m. The controller software was used to determine the resonant frequencies of the probe (approximately 300 kHz) and to set scan parameters.

3.4 Scanning electron microscopy

The fundamental resolution limit of optical microscopy limits the ability to investigate small scale structures on the order of hundreds of nanometers and below. These limits are described by the Rayleigh criterion, which defines the minimum resolvable separation that can be observed. The resolution is proportional to the wavelength of light incident on the sample. As a result, it is practically limited due to the wavelength of light. Scanning electron microscopy (SEM) provides the means to investigate incredibly small features through the principle of the wave-particle duality of matter. An electron gun is used to generate an ion beam through thermionic emission before accelerating it through an electric potential. The electron is accelerated with voltages of around 30 kV, providing it with an associated de Broglie wavelength on the order of Ångstroms.

Images are produced by raster scanning the primary electron beam over the surface of the material. Secondary electrons are a product of the higher energy

primary electrons inelastically scattering valence electrons from their shell. These low energy secondary electrons have a limited mean free path in solid materials. As a result, they will only escape the top few nanometers of the sample. The image is produced through contrast generated by the signal difference from these electrons to the detector.

Films deposited on structures were investigated using the FEI Versa Dual Beam Scattering Electron Microscope/Focused Ion Beam at the Centre for Advanced Nuclear Systems at McMaster University. Sampling milling for cross-section SEM imaging was performed using a 60 pA gallium (Ga) beam. In order to limit charge build-up, samples were mounted with conductive carbon tape to an aluminum stub and coated with 3 nm of gold using a physical vapour deposition (PVD) chamber.

3.5 Transmission electron microscopy

In contrast to SEM, where secondary electrons generated from the surface of a material are observed, TEM images are obtained by primary electrons passing through a sample and impinging onto a detector. In order for the detector to properly resolve electrons that have not been scattered, samples must be appropriately thin (< 100 nm), and primary electrons must be accelerated with higher voltages (> 100 kV). Images are produced through the contrast of the transmitted and the scattered electrons interacting with materials, defects, and structure of the sample.

When a sample is subjected to electron bombardment from a high energy source, there are a range of possible interactions that may occur. Some of these interactions are shown in Fig. 3.9. As these high energy electrons interact with

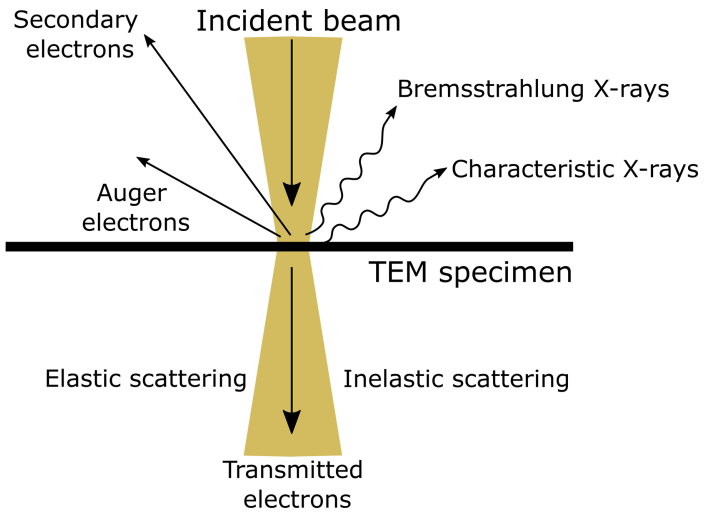

FIGURE 3.9: High energy electron interactions from incident beam on a semiconductor TEM specimen.

the sample, electrons may get ejected from the sample material. Electrons from higher energy states then fill the vacancies produced. The electron transitions result in the production of a characteristic x-ray via the conservation of energy. Energy dispersive X-ray spectroscopy (EDX) measurements process the relative abundance of incident x-rays from which the material matrix composition can be determined. This analytic technique is often used in conjunction with electron energy loss spectroscopy (EELS). Electrons that pass through the transmission electron microscopy (TEM) sample interact with a spectrometer where they are distinguished by their kinetic energy. Key features such as ionization edges allow for alternative means of determining matrix composition [151]. As electrons pass through a periodic crystal structure, they may be diffracted by the atoms at specific angles. The resulting diffraction patterns can be used as a crystallographic experimental technique, known as selected area electron diffraction (SAED), from which information regarding the crystallographic structures can be obtained. These analytic techniques were used in this thesis in an attempt to resolve nano-crystalline

Si structures in an amorphous SiO_x matrix. Transmission electron microscopy (TEM) samples require careful preparation, including milling a vertical slice of a deposited thin film down to tens of nanometers. A thin sample is necessary in order to limit the number of inelastic scattering events by a single electron in a sample to obtain high fidelity measurements.

Film structure details were investigated through high-resolution TEM. Samples were prepared using the FEI Titan 80–300 *Cryo-in-situ* microscopes at the Canadian Centre for Electron Microscopy (CCEM) at McMaster University. Focused ion beam (FIB) milling was used for the preparation of the high resolution (HR)-TEM samples by sputtering on either side of the area of interest using a platinum (Pt) beam current of 60 pA. The milling was performed for 30 min until the film layer was thinned to 80 nm. Prior to the FIB milling, a 20-nm gold layer was deposited using electron beam evaporation. EELS and EDX measurements were performed to characterize the clusters observed in the TEM images.

3.6 Photoluminescence spectroscopy

Photoluminescence (PL) spectroscopy was used as a means to measure room temperature visible emission spectra excited by ultraviolet (UV) laser excitation. When light from the source is incident on a rare-earth-doped sample, an electron from the rare-earth ion is promoted to an excited state. The electron undergoes radiative decay returning to its lower energy state. The UV excitation source used was a 325 nm HeCd laser, which was directed onto the sample using a free space optical set-up at an incident angle of 52° from the normal. Light emission from the sample was collected through a collimator lens and coupled through a multimode

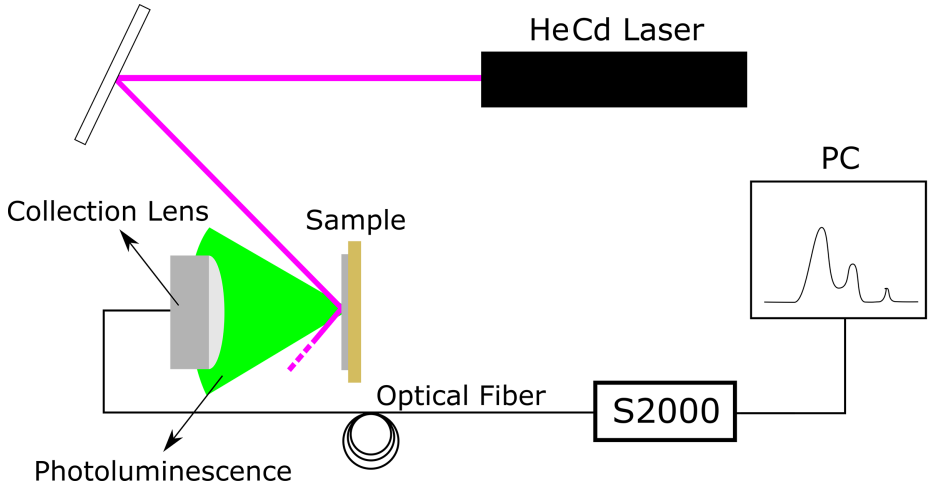

FIGURE 3.10: Photoluminescence spectroscopy set-up schematic. A HeCd 325 nm laser light source was used to excite Tb^{3+} doped SiO_x samples. Photoluminescent light was collected in a collimator lens and analyzed with an S2000 Ocean Optics spectrometer.

fibre optic cable to a visible charge-coupled device (CCD) spectrometer. The collection lens was mounted to a 3-axes stage, and its position was adjusted along the X- Y-plane to maximize signal intensity from the sample. A schematic diagram of this set-up is provided in Fig. 3.10 for reference. A particular challenge associated with HeCd lasers is that they are not stable over time. Helium atoms are small and prone to diffuse through the walls of the laser cavity. As a consequence, the power emitted by the laser will gradually decrease over time, which can influence the measured PL spectra. Upon initial characterization of the laser, the output power was reported to be 17 mW with an intensity of 640 mW/cm^2 [152]. At the time the bulk of the PL experiments in the thesis were performed, May 2017, the power had degraded to 2.3 mW. In order for comparisons between films measured years apart to be equitable, a standard calibration sample to normalize the data was required. This calibration sample was a particularly bright cerium and terbium co-doped sample produced by Patrick R. J. Wilson, a former Ph.D. student. Since

these measurements have been carried out, a new solid-state 375 nm laser has been purchased to replace the HeCd laser. This new laser has an adjustable power output of up to 100 mW. Measurements in this thesis were not carried out with this laser.

Further details regarding the HeCd PL set-up can be found in a journal article by O. H. Y. Zalloum et al [152] which outlines the set-up and calibration of the PL system.

3.7 Prism coupling

Optical attenuation in thin films can be challenging to quantify if the films are low loss. The sensitivity of an instrument, in this case, is dependent on the optical path length through the material. In many circumstances, it would be sufficient to take a reflection and transmission measurement of a film on a substrate and subtract these from the source signal to obtain the loss of the film (provided the loss of the substrate is also known). These measurements can be easily carried out through spectroscopic ellipsometry or spectrophotometry. Those techniques, however, have light passing through the thickness of the film with the optical path length, at best, being a few microns. A prism coupler, shown in Fig. 3.11, is a tool that allows for light from a source to couple into the film and propagate along it orthogonally to the normal. The film acts as a planar waveguide providing several centimetres of light-material interaction. As the light propagates through the film, a small amount escapes through surface scattering interactions. In order to determine optical attenuation, a detector can scan along the light streak in the film. This signal is then fit to a decaying exponential to extrapolate the film loss.

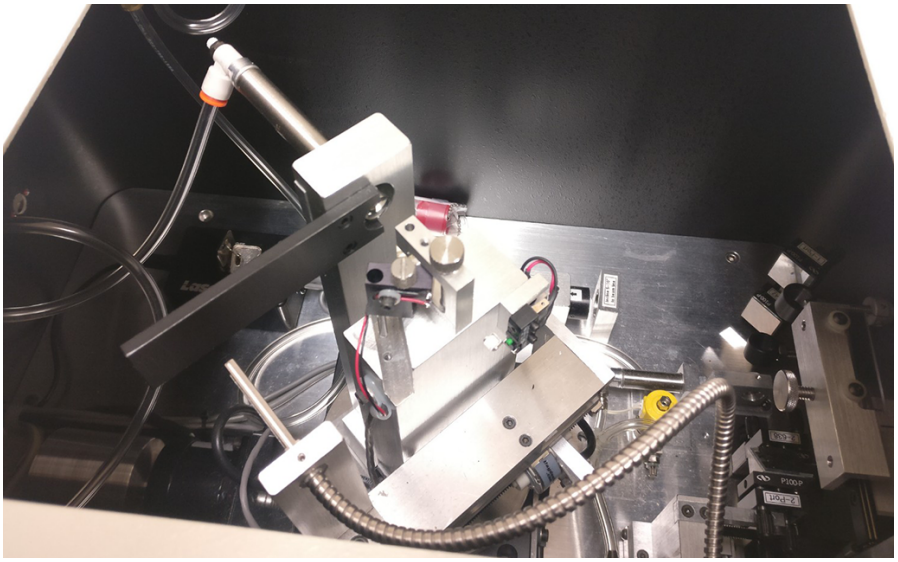

FIGURE 3.11: Photograph of the Metricon Model 2010/M Prism Coupler.

In order to perform a successful measurement, the refractive index of the film, n_F, must be greater than that of the substrate, n_0, in order to satisfy the total internal reflection conditions required for the film to guide light. Additionally, the refractive index of the prism, n_P, be must be greater than that of the thin film. A schematic of a prism coupler is shown in Fig. 3.12. The prism must be in good optical contact with the film to ensure that the evanescent field from the total internal reflection of the prism allows for coupling into the planar waveguide. Since the evanescent field strength will decay exponentially, the prism and film should be within a few µm or in contact. Furthermore, the films must be designed such that they can support a planar mode. Thermally oxidized silicon wafers provide a large surface area, low loss, low refractive index layer that can serve as the substrate layer for a planar waveguide. Care must be taken to ensure that the film is thick enough to prevent light from coupling into the higher index Si wafer under the thermal oxide. As a consequence, planar waveguide simulations using a mode

solver are essential to adequately ensure the partial power of the evanescent field interacting with the Si substrate is minimal. As a general rule, films in this thesis were designed to have less than 10^{-12} partial power in the silicon layer. These simulations should be carried out for each wavelength at which the user plans to obtain optical attenuation data.

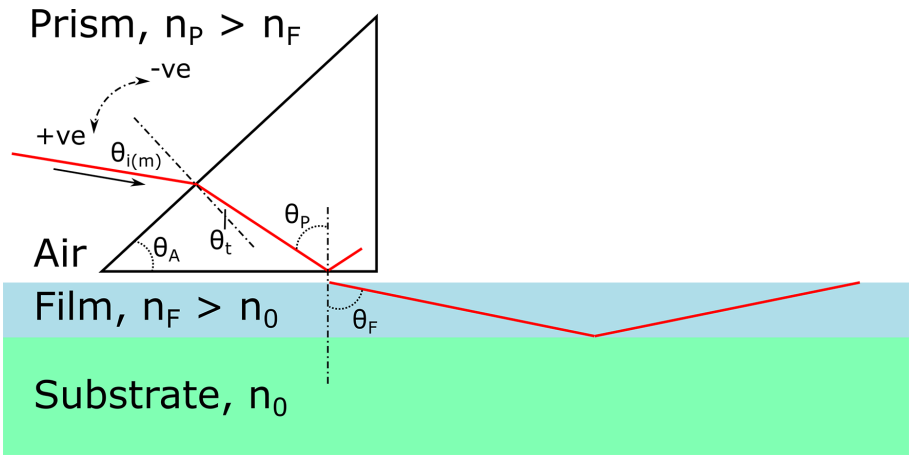

FIGURE 3.12: Schematic diagram of the prism coupling apparatus. A monochromatic laser source is coupled into the thin film through a prism. Coupling conditions allow discrete m- number of solutions for $\theta_{i(m)}$.

An additional criterion for light to couple into the planar waveguide is that the effective index, and consequently the phase velocity, of the light wave along the bottom surface of the prism (that of the evanescent field), must match the effective index of the waveguide mode, n_E. The phase velocity matching conditions are achieved through varying the angle of incidence of the light impinging upon the prism through rotation of the assembly. With reference to Fig. 3.12, the effective index of the light propagating along the prism surface at the prism waveguide boundary is $n_{EP} = n_P \sin\theta_P$ with the angle θ_P being a product of the prism angle and transmitted angle of the light at the prism input interface, $\theta_P = \theta_A + \theta_t$.

Through Snell's law, we can write, $\theta_t = \sin^{-1}[\sin(\theta_{i(m)})/n_p]$. The effective indices of the planar waveguide modes for which coupling is allowed can be observed through the following expression [153], [154]:

$$n_E = n_p \sin\left[\theta_A + \sin^{-1}\left(\frac{\sin\theta_{i(m)}}{n_p}\right)\right]. \tag{3.8}$$

The ability to change the effective index through assembly rotation is particularly useful as a mode order can be easily selected. Given that the fundamental mode is expected to have the lowest loss, the angle of the prism can be adjusted to couple into the mode with the highest effective index. The dependence on matching effective indices in order to couple into thin films presents a particular disadvantage of a prism coupler - it is not spectroscopic. The angle and the location of incidence of light impinging on the prism to achieve coupling is unique for each wavelength. As a result, spectroscopic loss measurements can be time-consuming as these must be carried out wavelength by wavelength.

In this work, optical attenuation measurements were obtained through a Metricon M2010/M prism coupler. Designed film heights were determined through slab mode simulations carried out in the RSOFT ModePROP^{TM} eigenmode expansion propagation tool. Films were then deposited onto a 3-inch diameter 6 µm thick thermally oxidized silicon wafer. These samples were stored in a vacuum desiccator between measurements in order to prevent potential film degradation over time caused by water diffusion into the films. Optical loss measurements were conducted over multiple paths on the wafer and averaged in order to minimize outlier results from surface defects on the film.

Chapter 4

System Development and Sample Fabrication

Preface

This chapter outlines the tools and fabrication techniques used to produce the samples in this thesis. A hybrid sputtering modality in an electron cyclotron resonance (ECR)-plasma enhanced chemical vapour deposition (PECVD) system was developed, which involved the extensive modification of an existing ECR-PECVD reactor. The development of this system is documented in the first section of this chapter. Thereafter, this chapter introduces the techniques used for *in-situ* rare-earth incorporation into silicon oxide (SiO_x) based thin films, on this newly developed system, via the hybrid sputtering of dopants inside an ECR reaction chamber. This is followed by a section that presents the fabrication of germanium oxide (GeO_2) samples, which were produced using IntlVac's alternating current (AC) plasma assisted reactive magnetron sputtering (PARMS) system. Lastly,

this chapter contains a section on the thermal annealing of thin films required to sensitize rare-earth dopants.

4.1 System development for hybrid sputtering in ECR-PECVD

The McMaster ECR-PECVD reactor is primarily used for the deposition of silicon-based thin films, such as silicon carbides, silicon oxides and silicon nitrides. The system was outfitted with metal-organic transport lines and crucibles in order to dope these silicon-based films with rare-earths. The installation of the original ECR-PECVD system is well documented in Ryszard Dabkowski's M.A.Sc thesis [155]. Differences in vapour pressures between rare-earth metal-organic precursors led to challenges regarding rare-earth contamination in films during growth. Additionally, the ligands from the metal organics can introduce additional contamination in the form of light elements [156]. The radio frequency (RF) sputtering modality was added to provide an alternate means of doping the hot matrix with rare-earth ions.

A similar technique had been developed for the *in-situ* doping of erbium in silicon dioxide (SiO_2) thin films 23 years ago [31], [157], [158]. The technique leveraged the high ion density from the ECR plasma and low pressure of the system to achieve sputtering by simply applying a negative direct current (DC) bias to the target. The target was placed mid-way between the ECR cavity and the gas injection ring. This configuration and power supply to the target differs from the approach taken with the system used in this thesis, as will be discussed later. In the previous work, film composition and doping concentration were adjusted through

varying the process gas flow rates, ratios and system pressure while maintaining a constant bias on the sputtering head. Again, as will be discussed, this is a different approach than the one taken in this thesis. The following section provides a detailed overview of the development of the hybrid sputtering system used for this thesis.

Hybrid sputtering was achieved with a Kurt J. Lesker Torus® circular high vacuum (HV) magnetron sputtering source combined with the ECR-PECVD system. The sputtering source used targets that are 50.8 mm (2 inches) in diameter and up to 6.3 mm (0.25 inches) thick. A schematic diagram of the sputtering source is provided in Fig. 4.1 and specifications are listed in Table 4.1. The sputtering source is relatively long compared to the radius of the chamber. This led to some initial concerns about the sputtering target being too close to the sample. Close proximity to the sample negatively impacts sample growth by providing too high a concentration of rare-earth ions into the film leading to ion-ion quenching effects. Furthermore, one of the primary benefits of using an ECR-PECVD is the remote plasma, which limits high energy ions from damaging the film during growth. This benefit is lost if the sputtering source is supplying a large number of these high energy ions. Therefore, the magnetron sputtering source was placed far back into the chamber, 22.0 cm from the sample, to provide a long throw range for the rare-earth ions. A schematic drawing of the modified system is provided in Fig. 4.2. A long throw range has the advantage of increasing film uniformity, which would translate into greater rare-earth doping uniformity. Furthermore, the greater range reduces the deposition rate of the sputtered rare-earth atoms, thanks to the inverse square law, which provides greater control of doping concentrations. Moreover, damage from electron bombardment

is limited, detracting less from the advantages provided by the ECR-PECVD system.

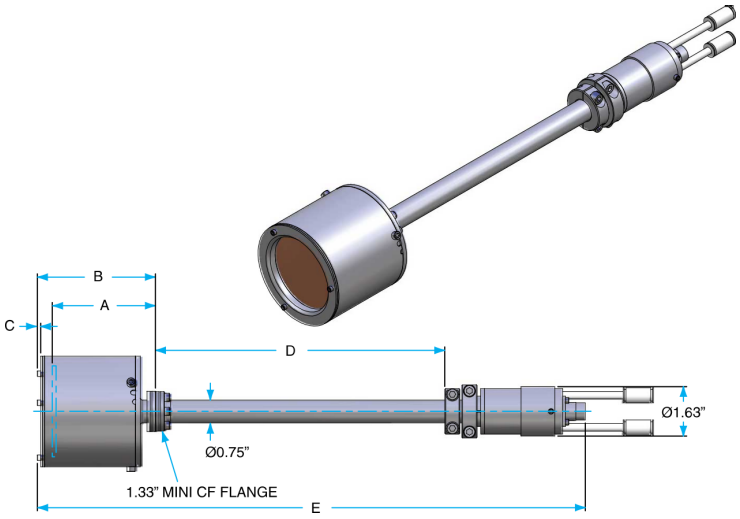

FIGURE 4.1: Schematic diagram of the TORUS® circular HV magnetron sputtering source. [159]

TABLE 4.1: Specifications for circular HV magnetron sputtering source shown in Fig. 4.1.

Parameter	Value	Parameter	Value
Target Diameter	2 in	Dim C	2.8 mm
Target Thickness	2 - 6.3 mm	Dim D	243 mm
Dim A	104 mm	Dim E	472 mm
Dim B	111 mm	Flange Size	6 in

In order to securely integrate the sputtering source to the main chamber and ensure a reasonable distance from the target to the sample, the sputtering source flange was mounted to a 6 inch to 8 inch off-center ConFlat® style reducer nipple and placed into a chamber port with a direct line of sight to the sample stage. It was decided during installation to opt for a chamber port at a greater angle to the sample normal as it avoided occlusion of the sample by the silane (SiH_4) gas injection ring; the angles for the sputtering source are illustrated in Fig. 4.3.

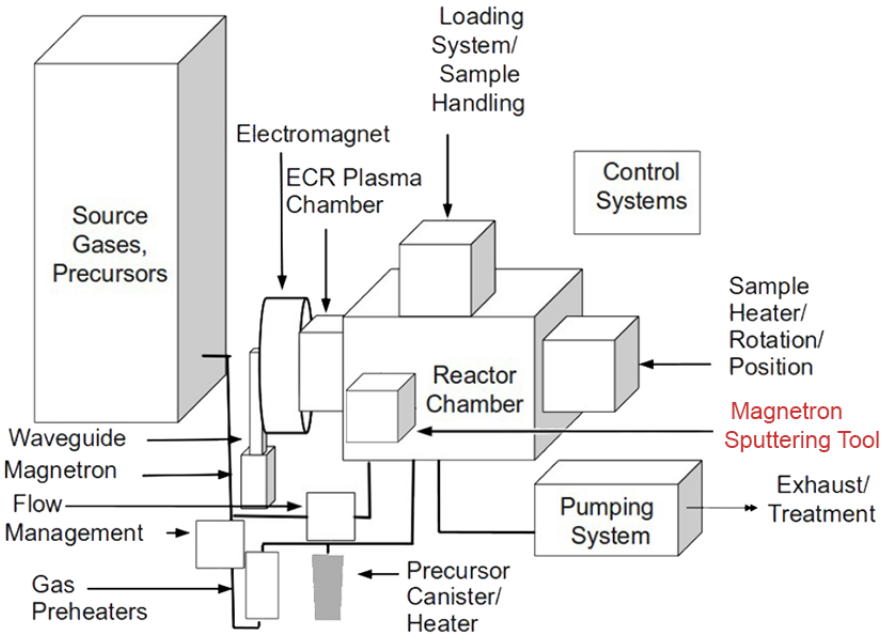

FIGURE 4.2: Schematic drawing of interconnection of major subsystems in the ECR-PECVD system. Image modified from [155].

The sputtering source's position can be moved in or out thanks to a flexible o-ring and screw fitting in the mounting flange. The decided upon position of the source is as far away from the sample as possible. If there were any future interest in positioning the source even further back, an 8 inch ConFlat® style full nipple could be added.

Argon was the inert gas chosen for sputtering and was supplied to the sputtering head through a gas injection ring. Modifications had to be made to the gas delivery lines for the ECR-PECVD to supply the sputtering tool. Initially, it was proposed that the Ar line that supplied the ECR reactor chamber be rerouted to the sputtering tool. This line was used for partial pressure compensation when studying the effects of altering gas ratios while maintaining a constant chamber

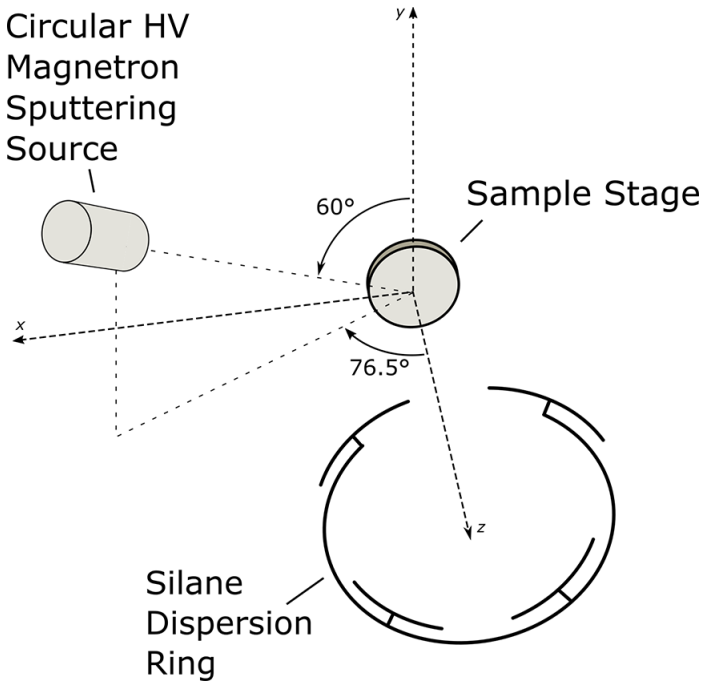

FIGURE 4.3: Schematic diagram of position circular HV magnetron sputtering source relative to other components in the reactor chamber.

pressure. It was later decided that it would be useful to maintain this functionality and that the Ar line would be bifurcated, shown in Fig. 4.4 a). The Ar transport line feeds into a mass flow controller, shown in Fig. 4.4 b), controlled by the bespoke programmable logic controller (PLC), which allows for a supply of up to 100 standard cubic centimeters per minute (sccm) of Ar to the sputtering head. The gas then travels into a flexible stainless steel tube, which connects to the gas inlets for the sputtering tool, as seen in Fig. 4.4 c).

The 13.56 MHz RF power to the sputtering source was supplied with a Seren R301 unit through a coaxial cable. An interlock is included in the power supply to ensure that it is used with an external control system. Given that no such external control system was used for this set-up, the interlock was cleared manually. This

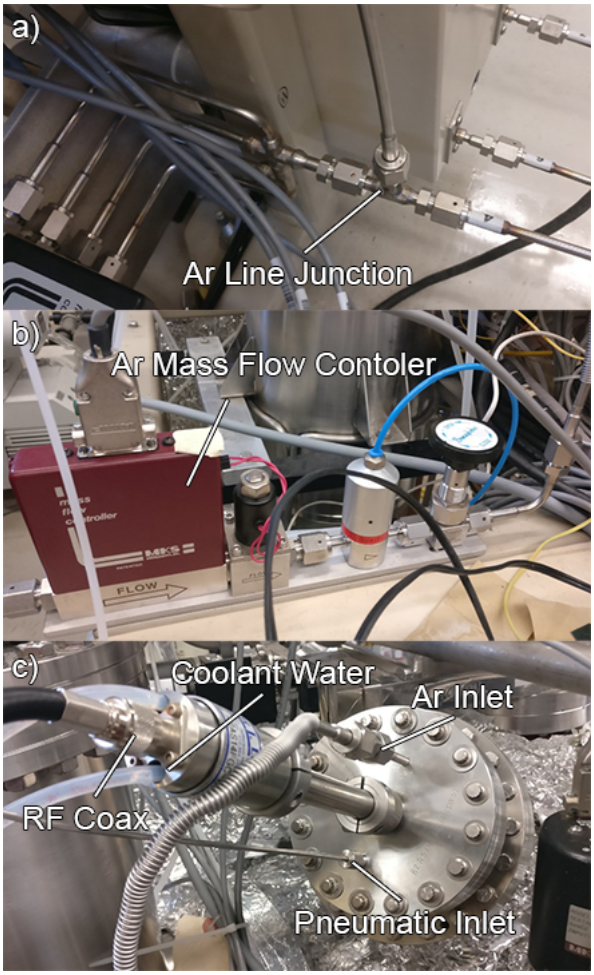

FIGURE 4.4: a) Various inputs for the sputtering source: coolant water, RF coaxial cable, Ar inlet, pneumatic inlet; b) MFC for Ar gas; c) bifurcated Ar line installed for sputtering source.

clearance was done by shorting pins 2 and 15 on the analogue interface connection together. A manual matching network, the Seren MM-Series, is used in conjunction with the power supply to impedance match the sputtering source load ensuring no reflected power. The matching network consists of two manual tunable knobs, a 22 – 822 pF tunable 'load' capacitor and a 17 – 178 pF tunable 'tune' capacitor. These sit in an 'L' configuration with the 'load' capacitor connecting the RF input to ground and the 'tune' capacitor connecting the RF input to the RF output

in series with a static inductor. The matching network also features a DC probe output, which allows the user to read the DC bias on the target. This reading can be especially useful if one wishes to determine the sputtering regime of the target in the presence of reactive gasses through the target hysteresis loop. As a note to users, the probe is attenuated by a factor of 200:1, and measurements must be appropriately scaled to obtain the actual DC bias.

To prevent samples from being coated with the sputtered materials during the sputtering source's ramp-up and cleaning phases, the target was shielded with a pneumatically actuated compact dome shutter. A 24 V DC valve manifold from IMI Norgen® was installed to manage the flow of compressed air to the sputtering source shutter and is controlled by the PLC system. As an additional upgrade to the system as a whole, a gas regulator with an inline filter was installed for the compressed air line to limit the compressed air pressure to 80 PSI.

Installing the sputtering source required the removal of the residual gas analyzer (RGA). The RGA serves to determine the composition of the gas in the chamber at base pressure. With it, it is possible to determine potential impurities before deposition. The most typical impurity would be water and hydroxide, which would show up as 18 and 17 amu respectively. Presently there exists an available port for installation should the RGA be needed.

The final installation of the sputtering source can be seen in Fig. 4.5 a) with its position relative to the silane dispersion ring and sample stage. The sputtering source is positioned such that it has a direct line of sight to the sample stage and is not partially occluded by the dispersion ring. An active deposition process is

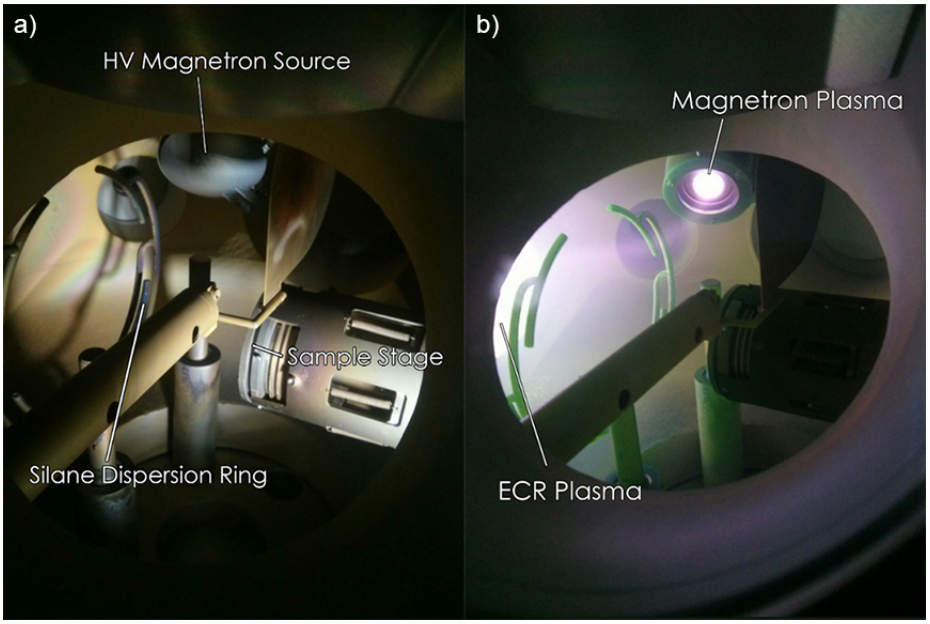

FIGURE 4.5: View inside ECR-PECVD reactor chamber. Individual elements are shown in a) with the positions of the silane dispersion ring, sample stage, and the HV magnetron source. The system under operation is shown in b). ECR plasma is contained in the ECR chamber, and the HV magnetron is introducing Tb species into the hot matrix.

shown in Fig. 4.5b). The ECR plasma is at left in the frame, and the magnetron plasma appears to be not contained to the sputtering head, forming a plasma trail to the ECR magnet. It is likely that the magnetic generated by the ECR solenoid and the sputtering magnetron significantly overlap, resulting in a dense magnetic field gradient that can contain the RF plasma between both plasma sources. The charged particles travel along these magnetic field lines, and the formation of the plasma trail is observed. Interestingly, green emission from the terbium ions coating various surfaces in the chamber, which are excited by the plasma, can also be observed in Fig. 4.5 b).

4.2 Deposition of Er and Tb doped thin films

An ECR-PECVD system was used to deposit the SiO_x host films while the terbium (Tb) and erbium (Er) dopant ions were introduced using a RF magnetron sputtering gun in the same reaction chamber. This hybrid sputtering system was installed as an upgrade to an existing ECR-PECVD chamber whose system details have been described in R. P. Dabkowski's M.A.Sc thesis [155]. The details pertaining to the integration of the RF magnetron sputtering tool for hybrid sputtering are described in Section 4.1.

The system was calibrated by depositing rare-earth-doped SiO_x thin films on slightly n-doped single-side polished $\langle 100 \rangle$ oriented silicon wafers and glossy carbon substrates. Samples were mounted onto a molybdenum sample holder held in place with tungsten wire pins. As further discussed in Section 5.1 the position of the sample on the stage is important; in order to maintain consistency between deposition runs, samples were placed in the same position on the sample holder. Samples were placed in a load-lock and moved into the reactor chamber via a vertical motorized transfer arm when the load-lock reached a suitable pressure of $<10^{-6}$ Torr (around 10 minutes).

Samples were heated using a back-side silicon carbide (SiC) heater controlled by a Eurotherm® 2404 proportional–integral–derivative (PID) controller. Given that sample temperature is a strong factor in influencing thin film properties, it is important to note that the steady-state temperature reported on the controller does not represent the actual steady-state temperature of the sample, but rather that of the heater. This difference in temperature is due to a combination of factors such

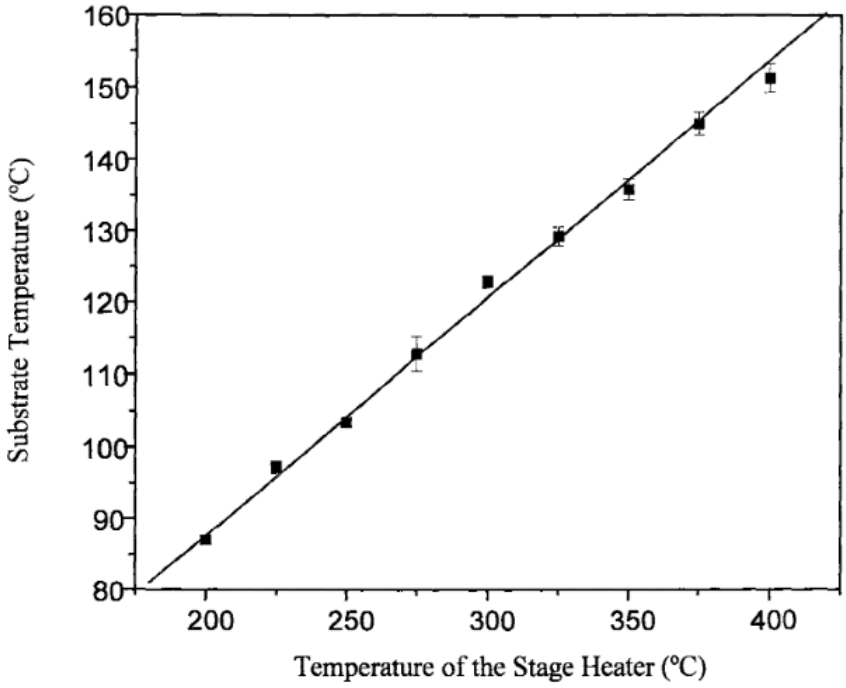

FIGURE 4.6: Temperature calibrations of the substrate temperature vs. the temperature of the stage heater. Taken from [160].

as heat loss through radiation, conduction through the sample arm assembly and thermal resistance of the molybdenum sample holder. Calibration of the sample temperature with respect to the heater temperature has been carried out elsewhere in H. Zhang's M.A.Sc thesis [160] and is presented in Fig. 4.6. The relation can be described through the following linear fit:

$$T_{sub} = 0.3303 \times T_{stage} + 21.58\,^{\circ}\mathrm{C} \tag{4.1}$$

where T_{sub} is the temperature of the sample substrate in °C and T_{stage} is the temperature of the stage heater in °C. For the films grown in this thesis, the stage heater was set to 350 °C, which according to Equation 4.1 corresponds to an actual

sample substrate temperature of 137 °C. The samples were left to sit after reaching this temperature for 20 minutes in order to ensure a steady-state.

For the thin film deposition, the microwave power from an Astex HS-1000 magnetron head was directed to the ECR-PECVD system via a waveguide and was set to 501 W forward power with an average value of 1 W reflected power. A circulator was used to monitor the reflected power and direct it towards a dummy load. Impedance load matching between the generator and the plasma was performed manually using a three stub tuner. The two process gases used were diluted in argon (SiH_4 at 30% and oxygen at 10%) and were introduced into the system through the SiH_4 dispersion ring and ECR reaction chamber. Doping of the thin films was achieved through a Kurt J Lesker axial mounted high vacuum RF magnetron sputtering gun. The head of the gun was configured to be 16.5 cm away from the sample and at an angular position relative to the SiH_4 dispersion ring and sample stage, as shown in Fig. 4.3 in Section 4.1, which enables a direct line of sight to the substrate. The rare-earth sources used were 99.999% pure Tb and 99.9% pure Er targets both 2 inches in diameter. Impurities were obtained for the less pure Er target by spectrographic analysis from the manufacturer and are shown in Table 4.2. Argon was used as the sputtering gas and was brought in to the sputtering head through a gas injection ring at a flow rate ranging from 40 to 60 sccm. Prior to deposition, the rare-earth target puck was cleaned using $2.0\,W/cm^2$ and 50 sccm Ar plasma for 10 min with the compact dome shutter closed to remove any possible contamination on the surface. The RF sputtering power density ranged from $0.5\,W/cm^2$ to $2\,W/cm^2$ for film depositions and was manually load matched and tuned to have 0 W of reflected power.

TABLE 4.2: Spectroscopic analysis of Er target.

Spectographic Analysis (ppm)				
La	Ce	Pr	Nd	Sm
21	12	29	15	25
Eu	Gd	Tb	Dy	Ho
3	28	9	45	41
Tm	Yb	Lu	Y	Fe
35	7	25	26	153
Si	Ca	Mg	Al	Cu
97	11	7	55	36
Ni	W	Mo	Ta	Nb
48	39	35	31	14

The rare-earth doping concentration was adjusted by varying the forward power applied to the RF sputtering tool. The films were grown at constant SiH_4 and oxygen (O_2) flow rates of 2.5 and 25.0 sccm, respectively. In order to achieve film uniformity during growth, a sample stage rotation of 0.5 Hz was applied to the sample holder. The sputtering power density and Ar partial pressure applied to the sputtering source were adjusted from 0.5 W/cm^2 to 2.0 W/cm^2 and 3.9 to 5.7 mTorr, respectively, for the study of Tb incorporation into SiO_x films. The total chamber pressure during film deposition was set at values ranging from 5.6 to 7.3 mTorr by keeping the SiH_4 and O_2 gas flow rates constant and adjusting the Ar gas flow rates from 10 to 40 sccm.

4.3 Deposition of GeO_2 thin films

Germanium oxide (GeO_2) thin films were deposited using an Intlvac Nanochrome IV plasma assisted reactive magnetron sputtering (PARMS) system. The system operated in a dual AC configuration with two 6" sputter sources comprised 99.995% pure germanium (Ge) targets. As the chamber was an experimental chamber that featured other material deposition processes, the inside walls and surfaces of the chamber were coated in a clean contaminant free ultra high vacuum (UHV) aluminum foil. After a change in the chamber process or after a set number of runs using the same process, the foil would be stripped from the inside of the chamber and replaced with a new set.

Single-side polished ⟨100⟩ n-doped Si, 6 µm thermal oxide and BK7 witness pieces (WPs) were prepared and mounted to an adjustable sample stage comprised of sliding rods that could be positioned to hold a sample of any shape less than 4-inches across. Once in place, the samples were further secured with Kapton® polyimide tape, which is chemically stable between −269 °C to 260 °C [161], and the sample holder was backed by UHV foil to mask any holes. As the system was a bottom-up sputter system, the samples were then secured into the system facing downwards.

A cryopump was used to pump the chamber down below 10^{-6} mTorr, and a set of 2 wall-mounted halogen lights interfaced with a PID system maintained the sample stage at a temperature of 120 °C. Deposition parameters were set into a bespoke system controller with the entire deposition process handled by the software. The deposition started with the introduction of argon (Ar) and O_2 gas

into the chamber followed by a gradual ramp-up in target forward power to the deposition set-point. This set-point was held for several minutes as a pre-cleaning stage to ensure contamination was removed from the Ge targets. Following the pre-cleaning, the target shutters were opened to commence the deposition.

Given that the system and deposition processes are tied to Intlvac's intellectual property, information has been deliberately omitted from this thesis and publication tied to this work highlighted in Chapter 6. These include the operational frequency of the AC sputtering source, sputtering power, chamber process pressures, rotation speed of the sample holder, and position and details regarding the ion-source.

4.4 Post-deposition annealing

The luminescence characteristics of SiO_x:Tb strongly depend on local structural properties that can be altered due to annealing, as shown in Section 5.4.4. To study these luminescent characteristics, following the deposition, the samples were annealed at temperatures from 700 °C to 1200 °C in steps of 100 °C in a Thermolyne^{TM} F21100 tube furnace with an operating range between 100 °C to 1200 °C. In order to limit contamination from the atmosphere, samples were introduced into the furnace in an inert high-purity molecular nitrogen (N_2) gas environment under constant flow.

The samples were placed onto a quartz sample boat connected to a long quartz rod and inserted into the front end of the quartz tube. The end of the tube was fitted with a metal end-cap with a small O-ring sealed hole to allow room for the quartz rod connected to the sample boat. The front end on the tube extended out

FIGURE 4.7: Photograph of Thermolyne^{TM} F21100 tube furnace used in the annealing of rare-earth doped SiO_x samples.

of the furnace by about 0.4 m, as seen in Fig. 4.7, allowing for the tube to be sealed and atmospheric gas to be purged with N_2. This feature allows for the insertion of the boat without subjecting the samples to annealing. After a waiting time of 15 minutes, the sample boat was moved to the center of the furnace. In order to ensure repeatability between the annealed samples, the quartz rod was marked to ensure the boat sat in the same position. The samples were then annealed for 60 minutes under a constant set N_2 flow. After annealing but before extraction, the samples were left to sit in the front end of the sealed tube to cool down for 15 minutes.

The temperature of the furnace was verified with a k-type thermocouple and it was found that the set point and actual temperature of the furnace did not agree at very high values (>1050 °C). Additionally, different regions of the furnace experienced different temperatures with the hottest point being in the centre. To

limit the influence of this temperature gradient, samples were only placed in the centre of the quartz boat.

While the quartz tube furnace provided a means to anneal small samples over a 60 min duration, it was not suitable for wafer sized samples that required annealing. These larger samples were required for prism coupling measurements, as explained further in Section 3.7, and were annealed in a Lindberg/Blue M^{TM} tube furnace with a maximum operating temperature of 1100 °C, see photograph in Fig. 4.8. The standard operating procedure for this furnace is similar to the Thermolyne^{TM} wherein a temperature was set, and a constant N_2 flow was pushed through the furnace. Samples were loaded onto a wafer boat and left in the front end of the tube for 15 min. After the purging time, the samples were pushed to the center of the furnace and annealed for 60 mins. To safely remove the samples, they were brought to the entrance of the tube and left to sit for 15 min before removal from the furnace.

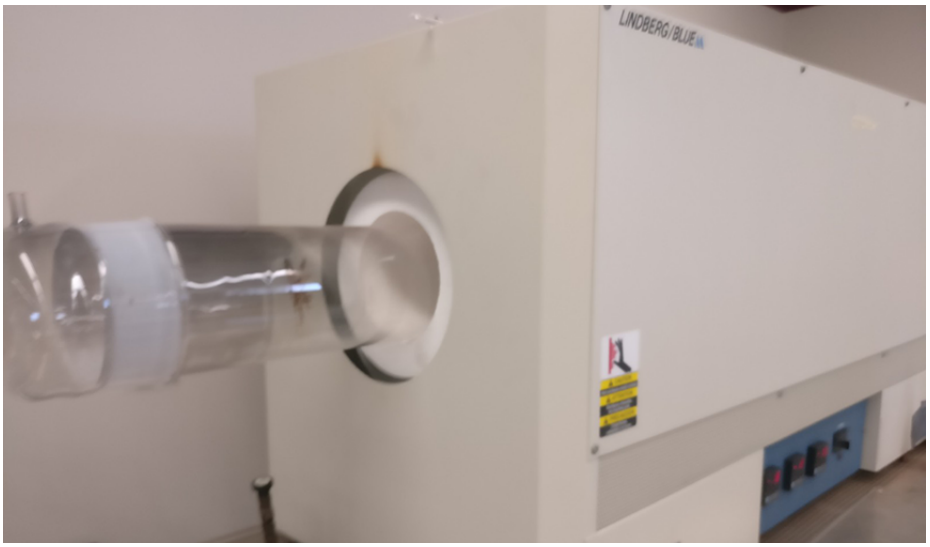

FIGURE 4.8: Photograph of Lindberg/Blue M^{TM} tube furnace used in the annealing of 3 inch GeO_2 samples.

Chapter 5

Study of Er:SiO_x and Tb:SiO_x Deposited through Hybrid ECR-PECVD

Preface

The following chapter presents results based on the addition of an radio frequency (RF) magnetron sputtering source for rare-earth doping using hybrid deposition in an electron cyclotron resonance (ECR)-plasma enhanced chemical vapour deposition (PECVD) system. The introduction of the sputtering source into the ECR-PECVD chamber began as a novel endeavour to explore alternative means of integrating rare-earth-dopants into silicon-based host matrices. It builds upon works carried out by previous group members who utilized metal-organic precursors as a means to incorporate rare-earth-dopants into silicon based thin films [162]–[165]. Over the course of those works, contamination from the metal-organic precursors had

become a concern. If the vapour pressure produced through the sublimation of one metal-organic precursor exceeds another, then small quantities of that precursor can pose a significant source of contamination. One benefit of sputtering from a rare-earth target is that it removes the need for the precursors and eliminates a potential source of contamination. Sputtered materials follow a line of sight path from the sputtering source and can be easily removed from surfaces in the chamber if they are adequately coated with foil.

While the work in this chapter concerning light emission from terbium, found in Sections 5.3, 5.4, and 5.5, has been published in the reference below, much of the calibration data surrounding the incorporation of erbium, found in 5.1, has not. It has been included as it provides a greater range of detail concerning the calibration of the novel hybrid sputtering in ECR-PECVD system. The approach taken towards calibration of the system is similar to past calibrations using metal-organics precursors, performed by past students in the research group, on the same ECR-PECVD system, which is carried out in P. R. J. Wilson's Ph.D. thesis [76].

J.W. Miller, Z. Khatami, J. Wojcik, J.D.B. Bradley, P. Mascher

"Integrated ECR-PECVD and Magnetron Sputtering System for Rare Earth-Doped Si-Based Materials"

This paper was published in *Surface and Coatings Technology*, in February 2018.

DOI:10.1016/j.surfcoat.2017.08.051

5.1 Calibration

Films produced in this section are stoichiometric SiO_2 or oxygen-rich SiO_x samples doped with either erbium or terbium. Sample composition was determined through Rutherford backscattering spectrometry (RBS) spectroscopy from as-deposited films, with the RBS spectra being fitted with the SIMNRA software package [141], with the atomic percentages quoted in this work obtained using this technique. It is also generally understood that there is hydrogen present in the as-deposited thin film samples. Outside of general comparisons, the hydrogen is not reported in the atomic make-up of the films.

The addition of the hybrid sputtering tool to the ECR-PECVD system introduces a significant radial asymmetry to the steady-state plasma distribution of the reactor chamber. The presence of this asymmetry raises the question of how significant, if at all, will this impact be on film uniformity across the available 3-inch deposition surface. Initial calibration of the chamber was based on deposition on a 3-inch silicon wafer. Except for the primary and secondary flat demarking the (110) plane, this wafer covered the entire available deposition surface. Two tests were conducted, one with and one without the 0.5 Hz sample stage rotation, during a typical deposition process. As expected, the film without sample rotation shows significant sample non-uniformity across a large area, as seen in Fig. 5.1 with a relative deviation in thickness, (Max-Min)/average, of 20.6%. The top left-hand section of the film shows the lowest film thickness, which roughly corresponded to the closest proximity of the wafer to the sputtering tool. The lower growth rate closer to the target can perhaps be explained by an uneven temperature distribution of the sample stage. It is possible that the section of the sample closer to the

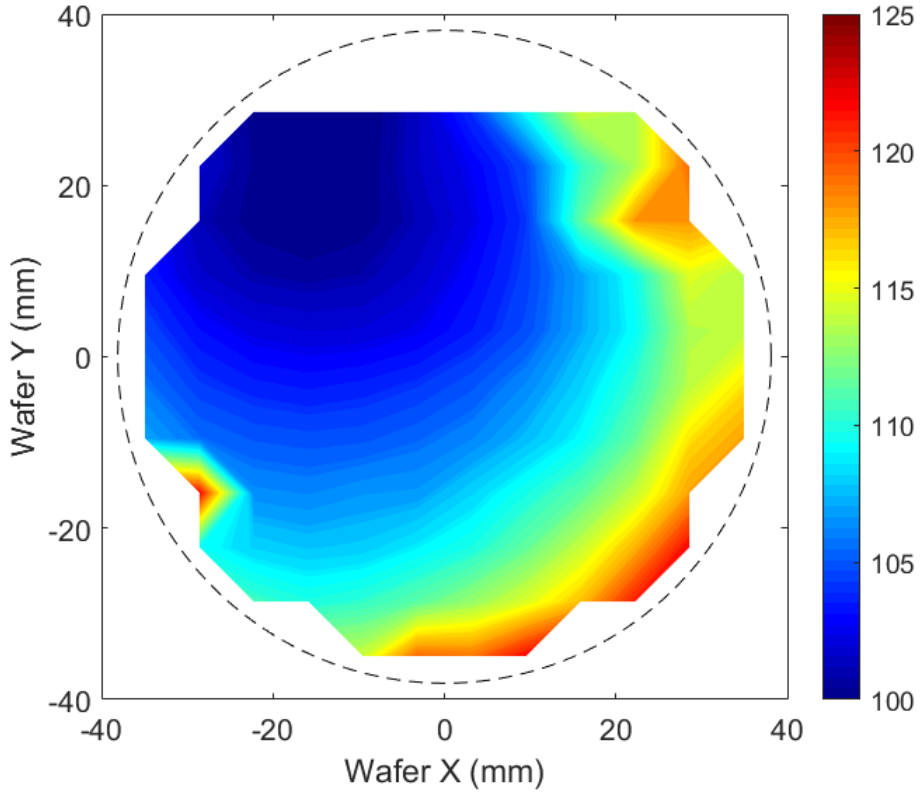

FIGURE 5.1: Heightmap in nanometers of an Er doped SiO_x thin film deposited on a 3-inch wafer under non-rotation conditions affixed to the sample stage. Primary $\langle 110 \rangle$ flat was oriented upwards. Sample fabricated with a sputtering power density of 0.74 W/cm^2, 2.5 sccm SiH_4/Ar, 25 sccm O_2/Ar, 40 sccm Ar to the sputtering head.

magnetron sputtering tool undergoes more high energy bombardment from plasma species, causing a local increase in temperature. The regions of the surface that are at a higher temperature experience a lower growth rate due to greater desorption and re-emission rates [166].

The introduction of 0.5 Hz rotation increases the large area sample uniformity relative to the non-rotating sample, as shown in Fig. 5.2, reducing the relative deviation in thickness to 7.6%. The sample exhibited radial symmetry, with the

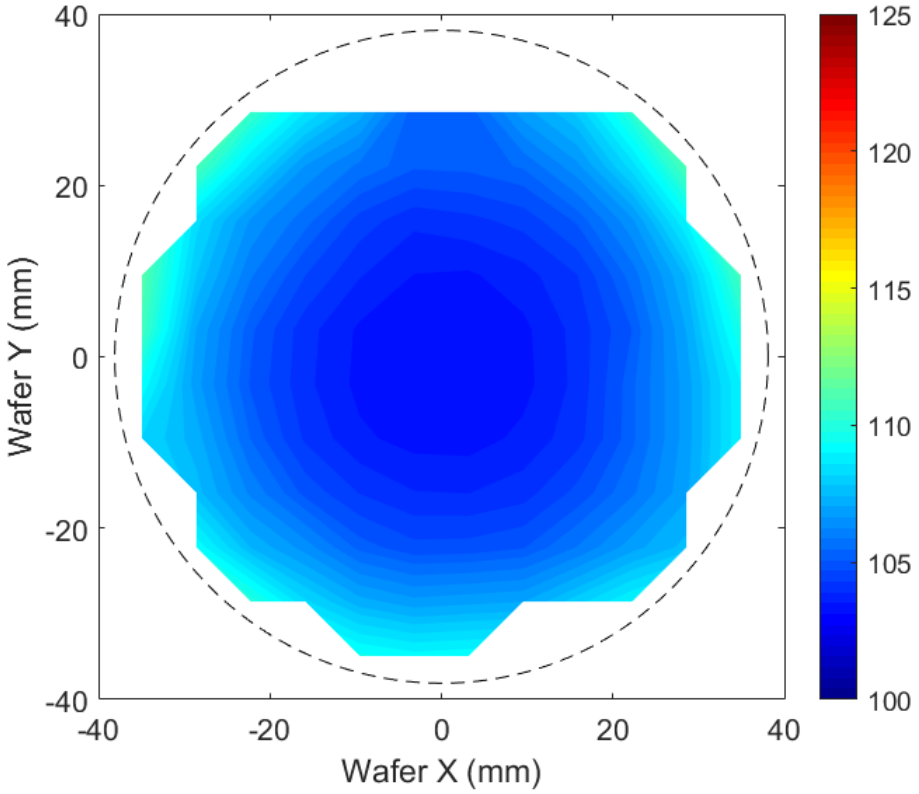

FIGURE 5.2: Heightmap in nanometers of an Er doped SiO_x thin film deposited on a 3-inch wafer under 0.5 Hz rotation conditions affixed to the sample stage. Primary ⟨110⟩ flat was oriented upwards. Sample fabricated with a sputtering power density of 0.74 W/cm^2, 2.5 sccm SiH_4/Ar, 25 sccm O_2/Ar, 40 sccm Ar to the sputtering head.

center of the wafer, having the lowest thickness. The presence of a slight radial non-uniformity raises the question of doping concentration uniformity for rare-earth materials deposited with the sputtering tool. Material characterization was performed with RBS on the sample along the linear segment bisecting across the center x-axis. These results showed a 6% higher relative concentration of rare-earth materials nearer to the center of the sample than near the edges, as seen in Fig. 5.3. Results for deposition uniformity without the sputtering tool were shown

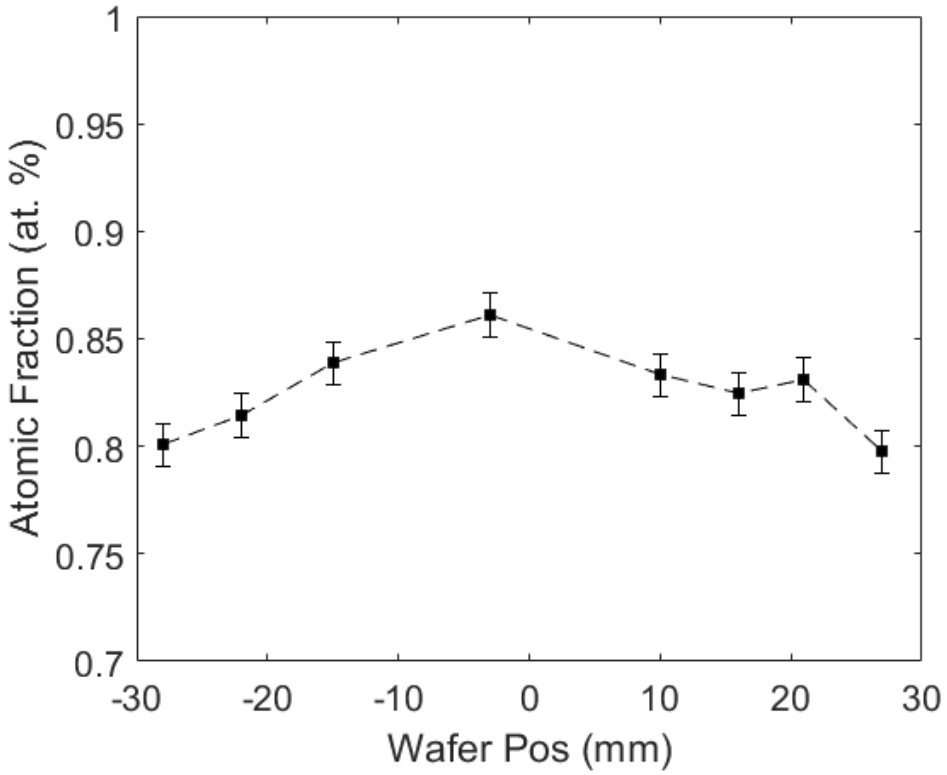

FIGURE 5.3: Atomic fraction of erbium ions across x-axis of 3-inch calibration wafer under 0.5 Hz rotation.

in previous work for the initial calibration of the ECR-PECVD system [155]. These show a radially symmetric tapered growth profile with the maximum thickness at the center of the sample stage with relative deviation in thickness, of 0.1% across a 15 mm radius. The sample shown in Fig. 5.3 has a relative deviation of 1.2% over the same radius.

The results, while intuitively obvious, are essential for building experiments on the upgraded ECR-PECVD system. In order to maintain consistency between experiments, samples should be placed roughly in the same position from one deposition run to the next. More importantly, however, if multiple experimental

samples are being fabricated in a single deposition, these samples should be placed equidistant from the center of the sample stage.

The effects of sputtering power from the RF magnetron sputtering tool was studied in the modified hybrid sputtering system. Films were grown with 2.5 standard cubic centimeters per minute (sccm) of SiH_4/Ar (30%/70%) and 25 sccm of O_2/Ar (10%/90%), a recipe that is known to grow stoichiometric SiO_2 on the system. This recipe was chosen as a starting point for the calibration of the system. A flow rate of 40 sccm of Ar (around 3.8 mTorr partial pressure) to the sputtering head was decided upon as it provided sufficient pressure to the inside of the reactor chamber to ignite the plasma surrounding the sputtering tool reliably. It should be noted that once the plasma at the sputtering head is ignited, the Ar flow to the head could be reduced without compromising the stability of the plasma. RF magnetron sputtering is known to operate at working pressures as low as 1 mTorr, which pairs nicely with the low working pressure of ECR-PECVD [167]. This information is only mentioned as it may be of particular interest for future students working on this system.

Sputtering powers of less than 4 W (0.2 W/cm^2) were found to not produce stable plasmas for the RF magnetron sputtering tool, and no films at that sputtering power or lower were produced. The adjustment of the sputtering power was thought to be the primary means by which doping concentration could be controlled; however, other parameters could also be used, such as the control of Ar partial pressure into the chamber, flow rates of the precursor gases, and less conveniently, the distance of the sputtering head to the sample stage. The deposition parameters of samples grown using the hybrid ECR-PECVD system are shown in Table 5.1, in

order of ascending sputtering power, along with resulting film properties such as atomic composition, thickness, refractive index, and mass density. The uncertainty of the atomic concentrations is strongly dependent on the substrate used for characterization. Samples grown with a carbon substrate witness piece (WP), had uncertainties for atomic fractions for Si and O of ± 1 at. % and uncertainties for Er of ± 0.1 at. %. This lower uncertainty is owed to the larger atomic cross-section of lanthanides due to their high atomic number, Z. Samples that use an Si WP have higher uncertainties for Si (± 4 at.%) and O (± 3 at.%) due to the signal overlap and channeling from the from the Si substrate. Some samples have unrecorded data and have been correspondingly marked (N/R).

TABLE 5.1: Hybrid ECR-PECVD system parameters and film properties. Atomic concentrations of Er, Si and O determined by RBS, and refractive index and thickness by VASE for all Er-doped SiO_x samples.

Sample Series		**SiO_x:Er**											
Sample ID#		**E01**	**E02**	**E03**	**E04**	**E05**	**E06**	**E11**	**E12**	**E13**	**E14**	**E07†**	**E08†**
Gas Flow Rate (sccm)	SiH_4/Ar	2.5	2.5	2.5	2.5	2.5	2.5	2.5	2.5	2.5	2.5	2.5	2.5
	O_2/Ar	25	25	25	25	25	25	25	25	25	25	25	25
	Ar	40	40	40	40	40	40	40	40	40	40	40	40
Gas Partial Pressure (mTorr)	SiH_4/Ar	0.10	0.15	0.14	N/R	N/R	0.12	0.15	0.14	0.12	0.18	0.16	N/R
	O_2/Ar	2.59	2.50	2.60	2.56	2.61	2.52	2.48	2.55	2.54	2.50	2.49	2.60
	Ar	3.90	3.84	3.67	3.77	3.82	3.95	3.77	3.81	3.82	3.90	3.75	3.75
Chamber Pressure	Deposition (mTorr)	6.42	6.37	6.42	6.40	6.45	6.48	6.50	6.44	6.60	6.55	6.63	6.52
	Base (nTorr)	500	200	600	300	400	400	300	400	200	200	400	300
Temperature (°C)	Stage Heater	350	350	350	350	350	350	350	350	350	350	350	350
ECR RF Power (W)	Forward	301	301	301	302	301	301	301	301	302	300	301	301
	Reflected	1	1	1	2	1	1	1	1	2	0	1	1
Sputtering Power Density (W/cm^2)	Forward	0.3	0.4	0.5	0.6	0.7	0.8	0.9	1.0	1.1	1.2	0.9	1.0
	Reflected	0	0	0	0	0	0	0	0	0	0	0	0
Time (min.)	Deposition	60	60	60	60	60	60	60	60	60	60	90	90
Atomic Fraction (at. %)	Si	33.21	33.68	33.11	32.66	32.30	31.56	31.64	31.14	29.40	33.21	27.4	28.1
	O	66.76	66.27	66.76	67.07	67.24	67.76	67.14	67.43	68.70	66.76	71.5	70.4
	Er	0.02	0.05	0.13	0.27	0.46	0.68	1.22	1.53	1.91	0.02	1.1	1.5
Physical Properties	Thickness (Å)	1022	1037	1049	1084	1060	1086	1045	1082	1063	1021	1577	1506
	Density (g/cm^3)	2.13	2.10	2.09	2.04	2.05	2.10	2.23	2.39	2.35	2.13	N/R	N/R
	n @ 632.8 nm	1.459	1.458	1.456	1.455	1.462	1.463	1.489	1.494	1.500	1.459	1.482	1.493

†Si RBS witness piece

TABLE 5.1: *(Continued).*

Sample Series		SiO_x:Er										
Sample ID#		E09†	E10†	E21	E23	E24	E26	E27	E28	E29	E30	E31	E32
Gas Flow Rate (sccm)	SiH_4/Ar	2.5	2.5	2.5	2.5	2.5	2.5	2.5	2.5	2.5	2.5	2.5	2.5
	O_2/Ar	25	25	25	25	25	25	25	25	25	25	25	25
	Ar	40	40	40	40	40	40	40	40	40	40	40	40
Gas Partial Pressure (mTorr)	SiH_4/Ar	0.15	0.14	0.16	0.15	0.13	0.15	0.14	0.15	0.16	0.14	0.12	0.15
	O_2/Ar	2.52	2.55	2.52	2.44	2.52	2.50	2.48	2.55	2.50	2.50	2.49	2.49
	Ar	3.83	3.91	3.91	3.84	3.92	3.99	4.03	4.02	4.07	3.98	4.01	3.97
Chamber Pressure	Deposition (mTorr)	6.48	6.5	6.54	6.61	6.6	6.51	6.6	6.6	6.53	6.51	6.54	6.54
	Base (nTorr)	500	600	600	400	500	300	140	300	200	400	100	100
Temperature (°C)	Stage Heater	350	350	350	350	350	350	350	350	350	350	350	350
ECR RF Power (W)	Forward	300	301	301	301	301	301	301	301	301	300	300	301
	Reflected	0	1	1	1	1	1	1	1	1	0	0	1
Sputtering Power Density (W/cm^2)	Forward	1.1	1.2	0.2	0.5	0.7	1.0	1.2	1.5	1.7	2.0	0.7	0.7
	Reflected	0	0	0	0	0	0	0	0	0	0	0	0
Time (min.)	Deposition	90	90	60	60	60	60	60	60	60	60	60	60
Atomic Fraction (at. %)	Si	27.2	28.40	33.10	32.11	31.23	31.18	29.53	29.54	28.82	27.10	N/R	N/R
	O	71.0	69.50	66.90	67.81	67.46	67.18	67.54	67.53	66.71	67.57	N/R	N/R
	Er	1.8	2.10	0.00	0.18	0.74	1.64	2.48	2.93	4.47	5.33	N/R	N/R
Physical Properties	Thickness (Å)	1510	1524	1085	1087	1063	1017	986	948	885	151	N/R	N/R
	Density (g/cm^3)	N/R	N/R	2.11	2.15	2.21	2.30	2.50	2.56	2.79	2.97	N/R	N/R
	n @ 632.8 nm	1.498	1.500	1.458	1.463	1.472	1.483	1.459	1.482	1.493	1.498	N/R	N/R

†Si RBS witness piece

The two sets of calibration samples, running from samples 01 through 14 and 21 through 32 are a result of using two separate erbium targets. Certain calibration samples were grown on silicon as opposed to carbon, samples 07 through 10. The RBS spectrum of these samples had a high amount of substrate channelling. As a consequence, the fits for the Si and O had higher uncertainty. The deposition conditions were later revisited using glassy carbon witness pieces in order to ensure that all samples were characterized using the same process.

The film compositions in Table 5.1 show the absolute atomic concentration of silicon, oxygen, and erbium. There are also trace amounts of argon in certain samples. Because argon is a noble gas, it is assumed that argon exists trapped in interstitial sites and consequently does not affect the bonding structure of the host matrix. The inclusion of hydrogen is also not shown in Table 5.1 as the element is too light to be detected through RBS. As further discussed in Section 5.4.1, there is some hydrogen present in the films, most likely introduced through the SiH_4 precursor gas.

Trends related to the atomic concentration of Er with respect to sputtering power density (sputtering power over the surface area of the target) are shown in Fig. 5.4. As expected, rare-earth incorporation increases as a function of sputtering power. Higher sputtering powers increase ionization, resulting in greater plasma densities around the target. This will lead to more ions hitting the target and result in more sputtered atoms. There appears to be two distinct incorporation trends. At higher sputtering power densities ($> 0.7\,\mathrm{W/cm^2}$), the atomic concentration of erbium appears to increases linearly with sputtering power. Given that the deposition rate of magnetron sputtering is linearly proportional to applied power, assuming all

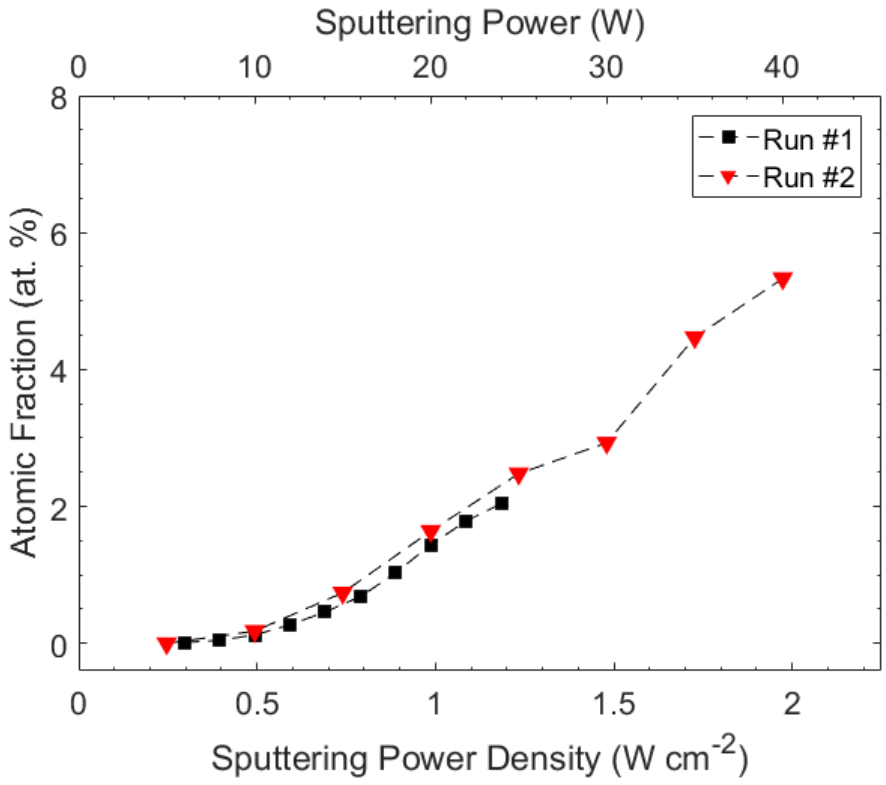

FIGURE 5.4: Atomic fraction of erbium ions in SiO_x matrix as a function of sputtering power density. Samples fabricated with 2.5 sccm of SiH_4/Ar, 25 sccm O_2/Ar, and 40 sccm Ar into the sputtering tool head. Uncertainty in the atomic concentrations is <0.1 at. % and too small to be displayed in this figure

other factors remain constant [168], then the linear relationship between sputtering power density and rare-earth incorporation makes intuitive sense. For lower power densities ($< 0.7\,\mathrm{W/cm^2}$), the relationship is non-linear with a gradual ramp-up to the linear trend. The non-linear relationship is advantageous when trying to incorporate small concentrations of rare-earth atoms into a matrix. The range of available powers for low concentration incorporation is more spread out, allowing for finer granularity over the atomic fraction of incorporated rare-earth ions. The

presence of this non-linear rare-earth incorporation response at low power densities can perhaps be explained by a similar non-linear response of the sputtering yield when operating just above the sputtering threshold [169], [170]. Alternatively, it perhaps is the case that the rare-earth atoms become ionized in the plasma and are subsequently influenced by the strong magnetic field generated by the ECR magnet. As these rare-earths would have low energies due to the low sputtering powers, their trajectories from the sputtering target to the sample would be more greatly affected.

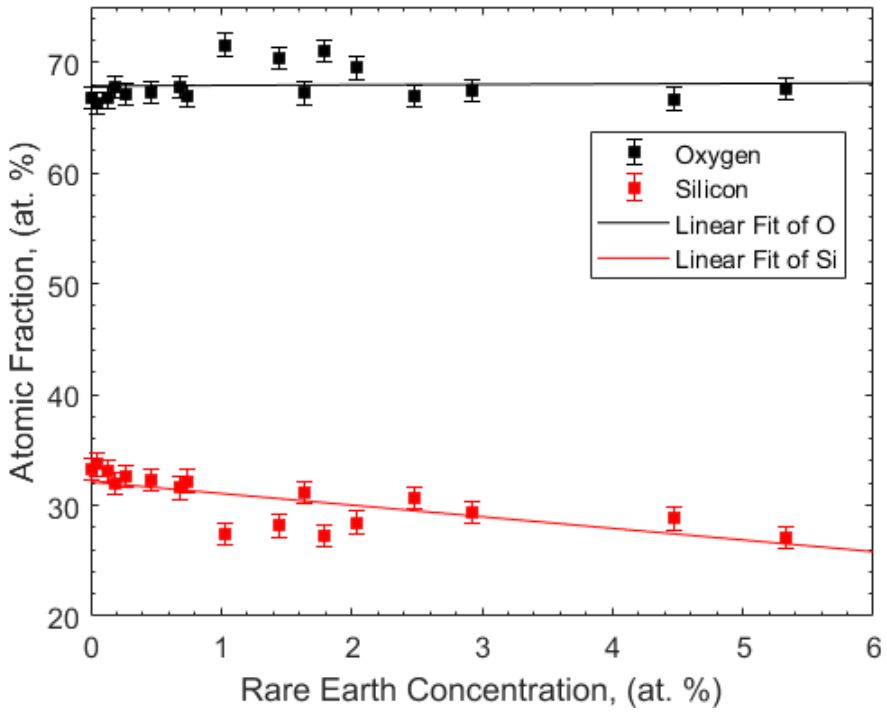

FIGURE 5.5: Silicon and oxygen atomic fractions as a function of rare-earth concentration in erbium-doped SiO_x films. Concentrations obtained through RBS.

The composition of the matrix in terms of atomic fraction of silicon and oxygen, compared to the concentration of rare-earths, is shown in Fig. 5.5. It can be seen

that the atomic fraction of oxygen remains relatively constant at around 68% whereas the atomic fraction of silicon linearly decreases. It can be reasonably inferred that the erbium ions are substituting Si atoms in the matrix as erbium will preferentially bond with oxygen over silicon [171]. The long throw-range of the sputtered erbium ions in the chamber plasma likely guarantee erbium will be coordinated with oxygen.

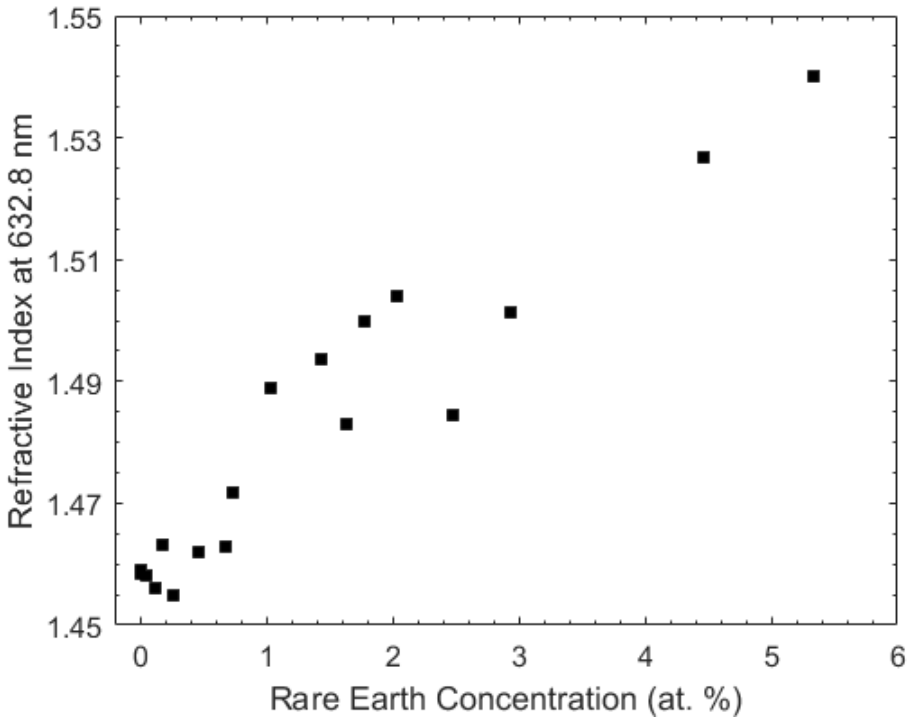

FIGURE 5.6: Refractive index at 632.8 nm as a function of erbium concentration in SiO_x films. Refractive index measurements obtained through VASE. Uncertainty in the data is too small to be shown.

Analysis of the films using VASE shows the change in the films' refractive index as a function of rare-earth concentration. The refractive index of the as-deposited films increases with higher rare-earth concentration, as depicted in Fig. 5.6. While these films are often referred to as rare-earth-doped glasses, it is perhaps more

accurate to refer to these films as alloys. The concentration of dopants is far more than what one would expect in a silicon semiconductor fabrication process. The significant increase in the refractive index can be described through the effective medium approximation (EMA), where the matrix is modelled as an alloy of SiO_2 and Er_2O_3, the latter of which has a refractive index reported between 1.8 to 1.9 at 632.8 nm [172]. By knowing the correlation between the refractive index and rare-earth incorporation, ellipsometry could be used as a quick estimate to determine the approximate rare-earth concentration of a sample at higher rare-earth concentrations.

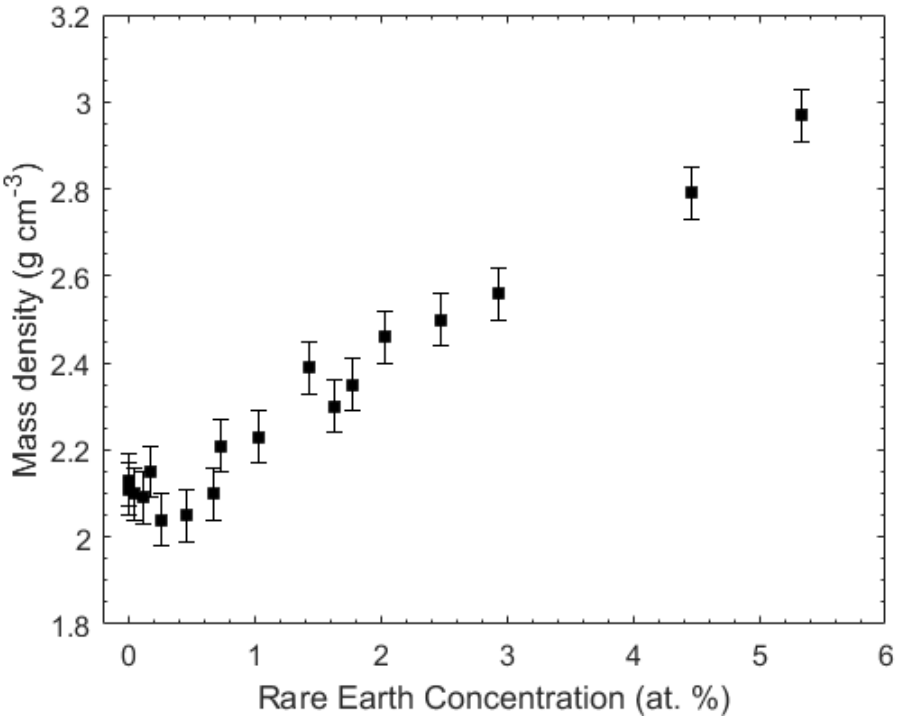

FIGURE 5.7: Mass density as a function of rare-earth concentration in SiO_x films. Results obtained with RBS and VASE measurements.

The incorporation of erbium also influences the mass density of the as-deposited films. These mass densities were calculated using a combination of RBS, to obtain

areal densities of elements within the films, and VASE to determine the thickness of the film. The calculation required is relatively trivial and is obtained with the following relation:

$$\rho = t^{-1} \sum_{i=1}^{k} \sigma_i m_i \tag{5.1}$$

where t is the thickness of the film, σ_i represents the areal density of an element within a film (in atoms/cm^2), and m_i represents the molar mass of that element (in g/mol). The sum is taken over a set of elements, k. The mass density of an a-SiO_2 grown through PECVD is approximately 2.202 g/cm^3 [173]. Variance in mass density may arise from the films' porosity during growth across different deposition conditions and between different deposition systems. The mass density of the thin films grown with a small (< 0.1 at.%) concentration of rare-earth ions is around 2.10 g/cm^3. It can be observed that the density of the films quickly increases to 2.97 g/cm^3, as shown in Fig. 5.7, with concentrations of Er of only 5.33 at. % representing a near 50% increase in mass density.

5.2 Integration of Tb into SiO_x

In the following sections, Tb-doped SiO_x thin films deposited through hybrid sputtered in an ECR-PECVD is presented. It is shown that *in-situ* doping through magnetron sputtering enables both widely tunable and highly consistent rare-earth dopant concentrations and yields less hydrogen incorporation in the films. The effects of sputtering power and Ar partial pressure on the Tb concentration, refractive index, thin-film morphology, and luminescence behaviour are investigated.

It is demonstrated that *in-situ* doping of rare-earths via magnetron sputtering is achievable with doping concentrations comparable to those achieved with metal-organic precursors and show green light emission for the first time using this promising new technique.

5.3 Experimental details

5.3.1 Deposition system

The microwave power of the ECR-PECVD system was set to 501 W with an average value of 1 W for the reflected power. The two process gases used were diluted in Ar (SiH_4 at 30%, O_2 at 10%) and were introduced into the system through the SiH_4 dispersion ring and ECR reaction chamber. They were directed towards the substrate, which was heated to a temperature of 120 °C. Doping of the thin films was achieved through a Kurt J Lesker axial mounted high vacuum RF magnetron sputtering gun. The head of the gun was configured to be 22.0 cm away from the sample and at an angular position relative to the SiH_4 dispersion ring and sample stage, as shown in Fig. 4.3, which enables a direct line of sight to the substrate. The rare-earth target was a 5 N elemental Tb puck, 2 inches in diameter. Argon was used as the sputtering gas and was brought in to the sputtering head through a gas injection ring at a flow rate ranging from 40 to 60 cm^3 per minute at sccm. The flow rate of the Ar gas was kept high to prevent poisoning of the target by the PECVD process gases. Prior to deposition, the Tb puck was cleaned using 2.0 W/cm^2 and 50 sccm Ar plasma for 10 min with the compact dome shutter closed to remove any possible contamination on the surface. The RF sputtering

power density ranged from 0.5 W/cm^2 to 2.0 W/cm^2 for film depositions and was manually load matched and tuned to have 0 W of reflected power.

5.3.2 Sample preparation

SiO_x:Tb^{3+} thin films were deposited on slightly n-doped single-side polished ⟨100⟩ oriented silicon wafers and glossy carbon substrates. The Tb^{3+} doping concentration was adjusted by varying the forward power applied to the sputtering gun. The films were grown at constant SiH_4 and O_2 flow rates of 2.0 and 15.0 sccm, respectively, which resulted in stoichiometric silicon dioxide thin films. The sputtering power density and Ar partial pressure applied to the sputtering source were adjusted from 0.5 W/cm^2 to 2.0 W/cm^2 and 3.9 to 5.7 mTorr, respectively, to deposit the set of samples listed in Table 5.2. This data in Table 5.2 is listed in order of ascending chamber pressure and increasing sputtering power. The total chamber pressure during film deposition was set at values ranging from 5.6 to 7.3 mTorr by keeping the SiH_4 and O_2 gas flow rates constant and adjusting the Ar gas flow rates from 10 to 40sccm. The average deposition rate was 11 ± 1 Å/ min, and the thickness of the films ranged from 26 to 37 nm. A summary of the sputtering conditions and resulting Tb concentrations, refractive indices, and thicknesses for the as-deposited thin films are given in Table 5.2. To study the luminescent properties, following the deposition, the samples were further annealed at temperatures from 700 °C to 1200 °C in steps of 100 °C. Annealing was carried out in a quartz tube furnace in a nitrogen gas environment for 1 h.

TABLE 5.2: Deposition parameters, atomic concentrations of Tb, Si and O determined by RBS, and refractive index and thickness determined by VASE for all Tb-doped SiO_x samples.

Sample Series		**SiO_x:Tb**											
Sample ID#		**Tb-4**	**Tb-1**	**Tb-8**	**Tb-5**	**Tb-2**	**Tb-9**	**Tb-6**	**Tb-3**	**Tb-13**	**Tb-11**	**Tb-10**	**Tb-12**
Gas Flow Rate (sccm)	SiH_4/Ar	2	2	2	2	2	2	2	2	2	2	2	2
	O_2/Ar	25	25	25	25	25	25	25	25	25	25	25	25
	Ar	40	50	60	40	50	60	40	50	60	40	50	60
Gas Partial Pressure (mTorr)	SiH_4/Ar	0.11	0.10	0.12	0.10	0.09	0.11	0.10	0.12	0.12	0.10	0.07	0.12
	O_2/Ar	2.5	2.6	2.5	2.4	2.5	2.5	2.5	2.6	2.5	2.5	2.5	2.5
	Ar	3.9	4.8	5.7	3.9	4.8	5.7	3.9	4.8	5.7	3.9	4.8	5.7
Chamber Pressure	Deposition (mTorr)	6.42	6.37	6.42	6.40	6.45	6.48	6.50	6.44	6.60	6.55	6.63	6.52
	Base (nTorr)	1000	500	1000	700	900	800	700	400	1000	620	1200	700
Temperature (°C)	Stage Heater	350	350	350	350	350	350	350	350	350	350	350	350
ECR RF Power (W)	Forward	301	301	301	301	301	301	301	301	301	301	301	301
	Reflected	1	1	1	1	1	1	1	1	1	1	1	1
Sputtering Power Density (W/cm^2)	Forward	0.5	0.5	0.5	0.7	0.7	0.7	1.0	1.0	1.0	2.0	2.0	2.0
	Reflected	0	0	0	0	0	0	0	0	0	0	0	0
Time (min.)	Deposition	30	30	30	30	30	30	30	30	30	30	30	30
Atomic Fraction (at. %)	Si (± 4)	33	33	-	31	36	-	32	35	-	30	33	26
	O (± 3)	65	66	-	67	62	-	65	62	-	62	61	67
	Tb (± 0.1)	0.4	0.6	0.4	1.2	1.4	1.7	1.7	2.0	1.8	6.8	7.4	7.0
Physical Properties	Thickness (±0.5Å)	350.6	344.3	355.9	331.0	348.1	369.1	319.1	341.3	351.4	263.7	284.1	268.1
	n @ 632.8 nm	1.49	1.5	1.49	1.51	1.51	1.51	1.52	1.52	1.53	1.61	1.62	1.63

5.4 Results and discussion

5.4.1 Composition analysis

Fig. 5.8 shows representative experimental RBS spectra and the corresponding fit of two SiO_x:Tb^{3+} samples grown using the same Ar flow rate (50 sccm) and with different sputtering powers. A higher concentration of Tb can be observed in the sample deposited with higher sputtering power. The Tb-1 and Tb-3 samples, grown using 0.5 W/cm^2 to 1.0 W/cm^2, respectively, contain 0.7 ± 0 .1 and 2.0 ± 0.1 at % Tb, respectively. The elemental analysis of all constituent elements of the Tb:SiO_x samples are plotted in Fig. 5.9 a). The low uncertainty in the Tb concentration is due to its high atomic number and, consequently, a large Rutherford scattering cross-section. This makes the Tb peak in the RBS spectrum, which is much greater than that of light elements, very sensitive to slight changes in the concentration. In addition, in the SIMNRA modelling software, certain elements (in this study Tb) can be fit with a higher degree of precision while sacrificing the precision of other elements. That explains the relatively high uncertainties for silicon and oxygen and the small error bars of Tb (Table 5.2 and Fig. 5.9). Within the uncertainty for the RBS measurements, the host material is found to be nearly stoichiometric silicon dioxide and relatively independent of pressure and sputtering power density from 0.5 to 2.0 W/cm^2.

To explore more closely the influence of the deposition conditions on the Tb concentration, the Tb atomic percent is plotted as a function of the chamber pressure and sputtering power density in Fig. 5.9 b). It can be observed that an increase of the sputtering power from 0.5 to 1.0 W/cm^2 increases the Tb content

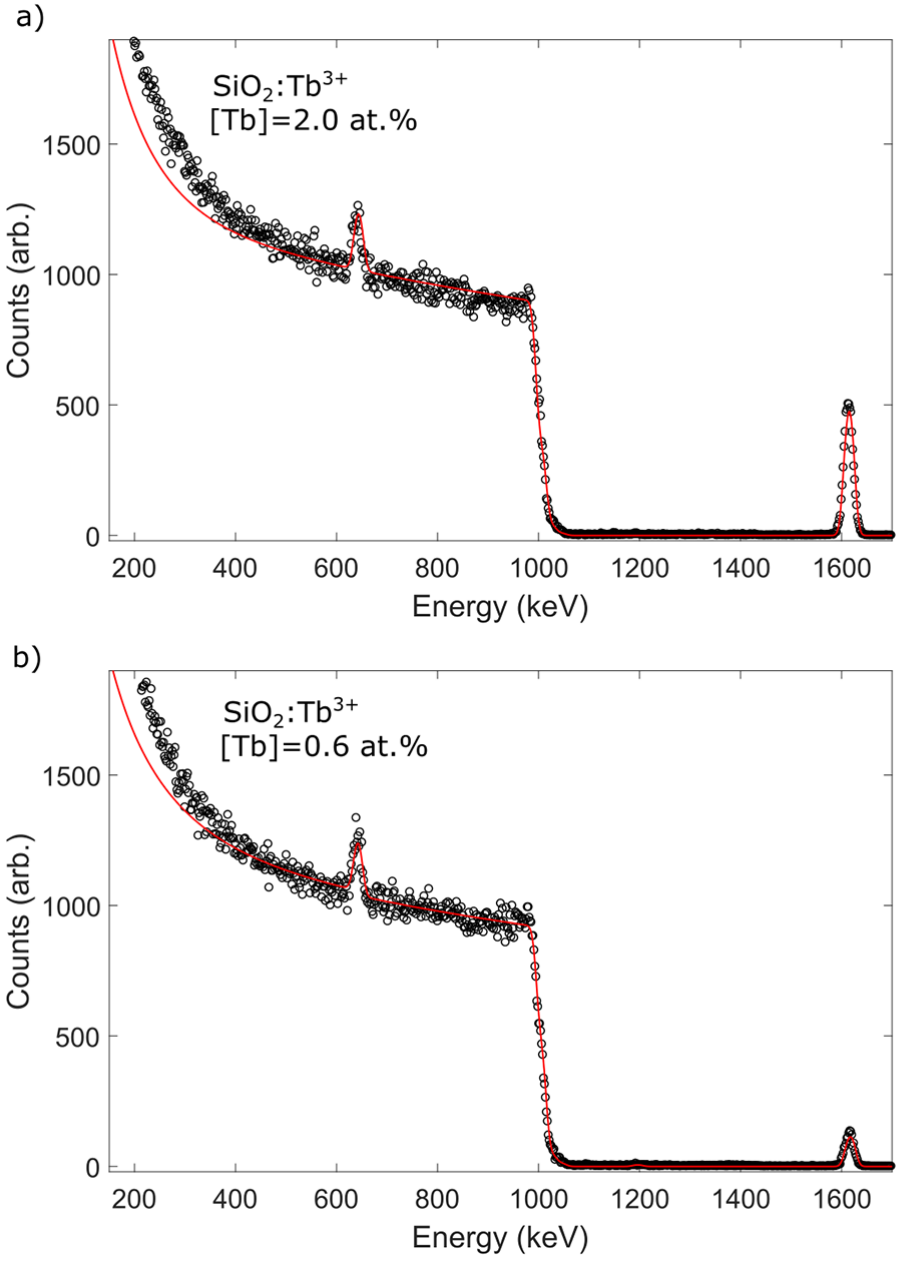

FIGURE 5.8: Experimental (black dots) and simulated (red line) RBS spectra of as-deposited SiO_2:Tb^{3+} thin films. The top sample, Tb-3, grown with a power density of 1.0 W/cm^2, contains 32 ± 3, 65 ± 4, and 2.0 ± 0.1 at % of Si, O, and Tb, respectively. The bottom sample, Tb-1, grown with a power density of 0.5 W/cm^2, contains of 32 ± 3, 67 ± 4, and 0.6 ± 0.1 at % Si, O, and Tb, respectively.

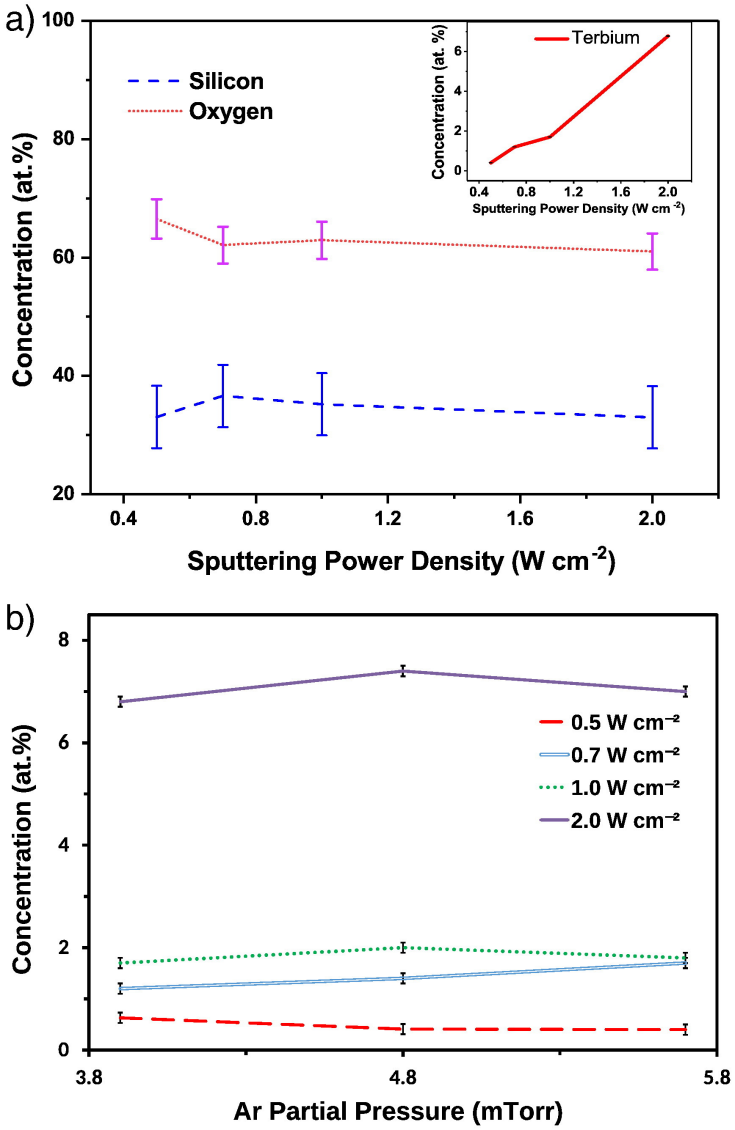

FIGURE 5.9: (a) Elemental composition of different as-deposited SiO_2:Tb^{3+} samples determined using RBS and plotted as a function of sputtering power density; (b) Tb concentrations of as-deposited films grown using varying RF powers, as a function of chamber pressure.

by about a factor of 3 whereas a further increase of sputtering power to 2.0 W/cm^2 leads to much more substantial increases of the Tb content by a factor of about 12. The influence of Ar gas flow shows a different behaviour and the virtually horizontal line of each sample in Fig. 5.9 b) implies that the chamber pressure has minimal impact on the Tb dopant concentration.

The hydrogen content of the films was determined using elastic recoil detection analysis (ERDA). The deposited films showed a hydrogen concentration of 3 at %, a much smaller amount than what is obtained commonly for a PECVD process employing SiH_4 gas as one of the precursors. Previously, the silicon-based films deposited using this ECR-PECVD system showed hydrogen concentrations at least three times larger [174], [175]. This may be explained by the higher dissociation of SiH_4 gas during the growth due to the presence of plasma species with higher energies in such an integrated ECR-PECVD and magnetron sputtering system. Alternatively, the lower hydrogen concentration may result from not using metal-organic precursors, which contain hydrogen in their ligands, to dope these thin-films with rare-earths. Residual hydrogen is produced when these precursors are cracked and may incorporate into the thin-film during growth.

5.4.2 Transmission electron microscopy

Fig. 5.10 shows a cross-section high resolution (HR)-transmission electron microscopy (TEM) image taken from the interface of the crystalline silicon substrate and the SiO_x:Tb^{3+} layer annealed at 1150 °C for 1 h in nitrogen gas ambient. The corresponding selected area electron diffraction (SAED) pattern reveals no feature, as shown in the inset of Fig. 5.11. SAED is generally used to confirm the local

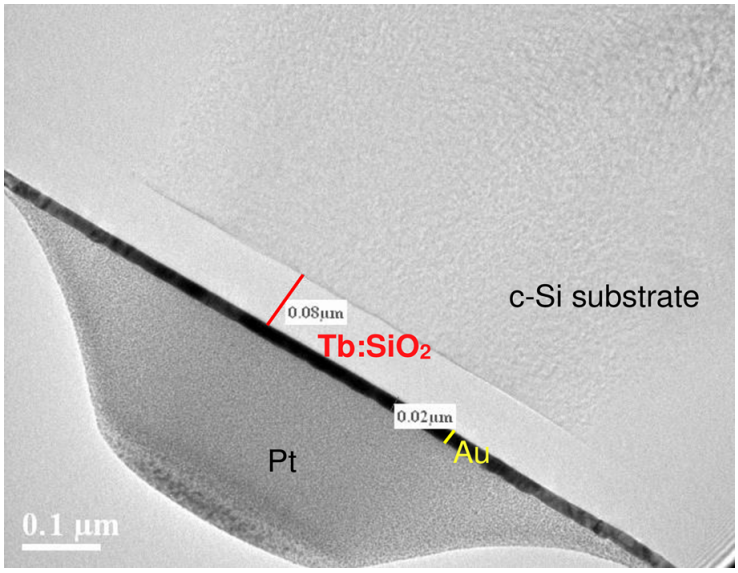

FIGURE 5.10: Low magnification cross-sectional HR-TEM images of the Tb:SiO_2 prepared by FIB. The thickness of the gold layer and the Tb:SiO_2 layer ([Tb]=2.0 at %) are shown.

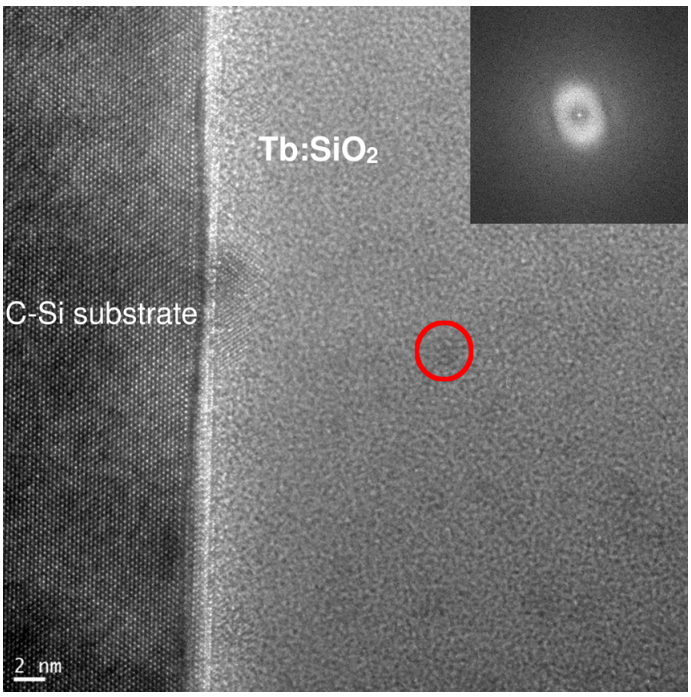

FIGURE 5.11: Cross-section HR-TEM bright-field image of a Tb:SiO_2 layer annealed at 1100 °C for 1h.

phases of relatively large nano-clusters (>5 nm) [176]. This indicates either that the observed spots are silicon nano-clusters with a size smaller than 5 nm or an agglomeration of Tb atoms (which is not the case as will be discussed in the following). Dark spots are observed through the film depth, one of which is marked by the red circle. The darker areas in the bright-field image indicate higher density regions, which could be the agglomeration of gold (Au) and platinum (Pt) atoms in addition to silicon and Tb atoms. The Au layer is used to prevent the charging of insulating materials during the FIB process using Pt beam, and both Au and Pt particles may diffuse in the host silicon dioxide film.

To identify the composition of the embedded clusters, both electron energy loss spectroscopy (EELS) and energy dispersive X-ray spectroscopy (EDX) were applied to examine these spots. Fig. 5.11 shows low magnification cross-sectional HR-TEM images of the sample thinned to 80 nm with a 20 nm Au layer on the top. The intensity of the Pt and Au signal in the EDX spectrum (not shown here) is around the noise level and is similar for both the amorphous areas and the darker spots. This indicates that the clusters are not composed of Au and/or Pt. EDX also shows a very weak Tb signal close to the noise level, which is expected due to the low concentration of Tb^{3+} ions in the film. Therefore, the composition of the embedded clusters cannot be confirmed by EDX measurements. However, low-loss measurements show that the spectrum in the region of the cluster is slightly different from that of the amorphous area of the film. The difference corresponds to an increase in the silicon signal, while no changes are observed for the Tb signal in the EELS spectrum in the cluster region. This indicates that Tb^{3+} ions are not aggregated upon the high annealing temperatures, which would serve to quench

the visible emission from these ions [38], and the observed clusters (dark areas) contain higher concentrations of silicon. However, silicon nanocrystals cannot be clearly detected in the HR-TEM image, which is expected from a non-silicon rich silicon oxide host matrix (the samples have a stoichiometry equal to that of silicon dioxide within the experimental uncertainty).

5.4.3 Optical properties

The model used for fitting the VASE data includes only the first two Cauchy coefficients and the parameters of the silicon substrate taken from Herzinger et al. [177]. The Cauchy model describes the refractive index (n) as a function of varying wavelength (λ) and extinction coefficient (k) as an exponential absorption function:

$$n(\lambda) = A + B/\lambda^2 + C/\lambda^4 \tag{5.2}$$

$$k(\lambda) = \alpha \exp\{\beta[12400(1/\lambda - 1/\gamma)]\} \tag{5.3}$$

the fitting parameters, α is the absorption coefficient, β is the exponent factor, and γ is the band edge. The exponential term in Equation. 5.3 can adequately describe any sub-bandgap absorption at the bandgap edge [178].

In Fig. 5.12 the refractive indices at 632.8 nm, and the thicknesses of the samples grown using an Ar flow of 40 sccm (Ar partial pressure of 3.9 mTorr) are plotted as a function of sputtering power density. The error bars depicted in Fig. 5.12 represents the low MSEs, which express a high quality of the fit. The refractive index of the film increases with increasing sputtering power density. In Fig. 5.12,

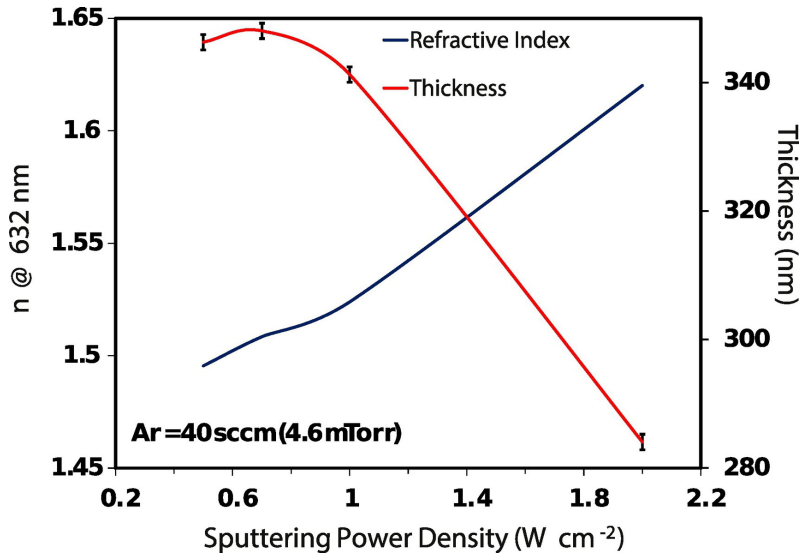

FIGURE 5.12: Refractive index and thickness of as-deposited Tb:SiO_2 thin films grown with Ar partial pressure of 4.8 mTorr (40 sccm Ar flow) as a function of Tb sputtering power density.

the increase of the refractive index is smaller within the lower power density region and is significantly larger at higher power. The film thickness, in contrast to the refractive index, is virtually constant for the lower sputtering power density (slightly decreases) and significantly decreases with the higher power density at 2.0 W/cm^2. The increase in the film index with higher sputtering power is likely related to the higher Tb concentration (see Fig. 5.9 in Section 5.4.1) [179].

5.4.4 Photoluminescence

Fig. 5.13 shows photoluminescence (PL) profiles of the Tb-1 sample subjected to annealing in N_2 for 1 h in the temperature range of 700 °C to 1200 °C. The sample was grown using 0.7 W/cm^2 of sputtering power density and 40 sccm of Ar gas flow (resulting in a partial pressure of 3.8 mTorr) and contains 0.6 at % Tb (Table 5.2). The green Tb related PL, observed by the naked eye under dark room-lighting

conditions, confirms the successful excitation of optically active Tb (Tb^{3+}) ions within the stoichiometric silicon dioxide host matrix. Regardless of the different Ar partial pressures and sputtering powers applied (and different resulting Tb concentrations), for all the samples, two main PL bands, associated with the Tb^{3+} intra-4f transitions from the $^5D_4$ to $^7F_6$ level at 493 nm and $^5D_4$ to $^7F_5$ level at 543 nm, and one negligible PL band related to the $^5D_4$ to $^7F_4$ transition at 584 nm are observed. The strongest emission is at 543 nm, which corresponds to the electric dipole transition and is often identified as the most intensive emission [162]. The PL emission intensity decreases upon annealing from 700 °C to 1000 °C, and it starts to increase with further annealing beyond 1100 °C, followed by a drastic increase at 1200 °C.

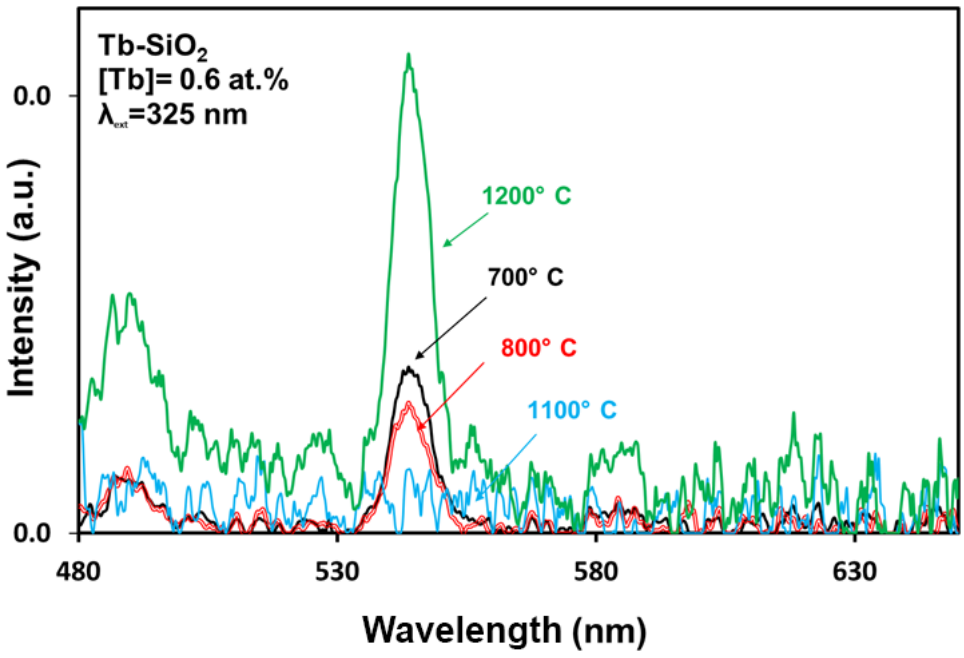

FIGURE 5.13: Luminescence spectra of Tb:SiO_x samples containing 0.6 at % of Tb annealed at various temperatures. The corresponding temperature is labelled.

Terbium is non-resonant at the excitation wavelength of 325 nm. However, the oxygen-related states, due to defects in the host matrix or oxygen bonding at the Tb sites can act as sensitizers and contribute to luminescence. At lower annealing temperatures, the decrease of PL emission with temperature can be explained by these oxygen-defect related luminescence centres [131]. In general, these defects are gradually removed during the annealing process in an inert ambient gas such as N_2 [131]. The enhancement of PL emission at elevated temperatures is possibly due to restructuring of the local environment of Tb^{3+} ions and the formation of Tb-silicate structures containing higher concentrations of silicon atoms, as supported by HR-TEM and EELS analyses (Section 5.4.2). The mechanisms of Tb^{3+} excitation at the higher annealing temperatures and their dependence on the embedded silicon-related clusters have been discussed previously [162], [180]. All samples show a similar trend for the thermally induced changes of PL emission at different annealing temperatures. Therefore, neither the sputtering power nor the Ar pressure have any considerable effect on the thermal behaviour of the PL emission.

5.5 Conclusion

In-situ Tb doping of SiO_x thin films using a magnetron sputtering source attached to an ECR-PECVD chamber was demonstrated. To characterize the system performance, the influence of the deposition conditions on SiO_x:Tb^{3+} samples was investigated. The RF sputtering power and Ar gas partial pressure was adjusted and the subsequent changes in Tb content and refractive index were measured. The Tb concentration showed a non-linear relationship with the sputtering power,

ranging from 0.4 to 7.4 at. % for sputtering power densities ranging from 0.5 to 2.0 W/cm^2. Changing the Ar gas partial pressure between 3.9 and 5.7 mTorr appeared to only slightly affect the Tb content (e.g. 6.8 to 7.4 at % at 2.0 W/cm^2). The refractive index of the films was found to increase with higher sputtering powers, which is likely due to the larger Tb concentration in the films. Green Tb^{3+} related PL was observed by the naked eye under dark room lighting conditions and the annealing conditions required to activate Tb^{3+} ions embedded in the silicon dioxide host matrix were investigated. HR-TEM imaging showed an amorphous structure of the produced SiO_x:Tb^{3+} thin films. The formation of silicon clusters was observed in the samples subjected to post-deposition annealing at 1100 °C as determined by EELS and EDS measurements and a corresponding increase in PL intensity were observed.

These results show that the custom integrated magnetron sputtering and ECR-PECVD system produced silicon-based thin films with a high level of control over dopant levels and achieved doping concentrations comparable to a metal-organic process. The exploitation of this technique is not limited to Tb dopants and, thus, opens opportunities for future investigations of other materials systems.

Chapter 6

Low-Loss GeO_2 Thin Films Deposited by Ion-Assisted Alternating Current Reactive Sputtering for Waveguide Applications

Preface

The following chapter presents results on germanium oxide (GeO_2) thin films deposited by ion-assisted alternating current reactive sputtering for waveguiding applications. This work is motivated by the appeal of high refractive index low-loss materials as waveguides for on-chip amplifiers and light sources and parallels similar work carried out by group members on other doped and undoped metal-oxide

materials [95], [98]. The work presents materials with low optical losses compared to other published deposition techniques without the need for post-deposition processing.

J.W. Miller, M. Chesaux, D. Deligiannis, P. Mascher, J.D.B. Bradley

"Low-loss GeO_2 thin films deposited by ion-assisted alternating current reactive sputtering for waveguide applications"

This paper was published in *Thin Solid Films*, in June 2020.

DOI:10.1016/j.tsf.2020.138165

6.1 Introduction

Dual alternating current (AC) magnetron sputtering in conjunction with high energy ionic bombardment is known to yield high-quality thin films with high density and uniformity [181]. While other films such as magnesium oxides and tantalum oxynitrides have been fabricated and reported on for optical applications [182], [183], GeO_2 thin film fabrication has not been extensively explored using this deposition technique.

In this chapter, GeO_2 thin film deposition using dual AC ion-assisted sputtering were studied. The films were deposited in varying regions of the sputtering bias hysteresis curve and their structural and optical properties were studied. The film stoichiometry is confirmed through high energy ion-matter interactions using Rutherford backscattering spectrometry (RBS) and elastic recoil detection analysis (ERDA). We measure low propagation losses using the prism coupling technique

and observe low surface roughness using atomic force microscopy (AFM). These properties, combined with high deposition rates and insensitivity to process variation, demonstrate ion-assisted dual AC sputtering to be a highly promising method for planar waveguide fabrication.

6.2 Experimental methods

6.2.1 Ion-assisted dual AC sputtering of GeO_2 thin films

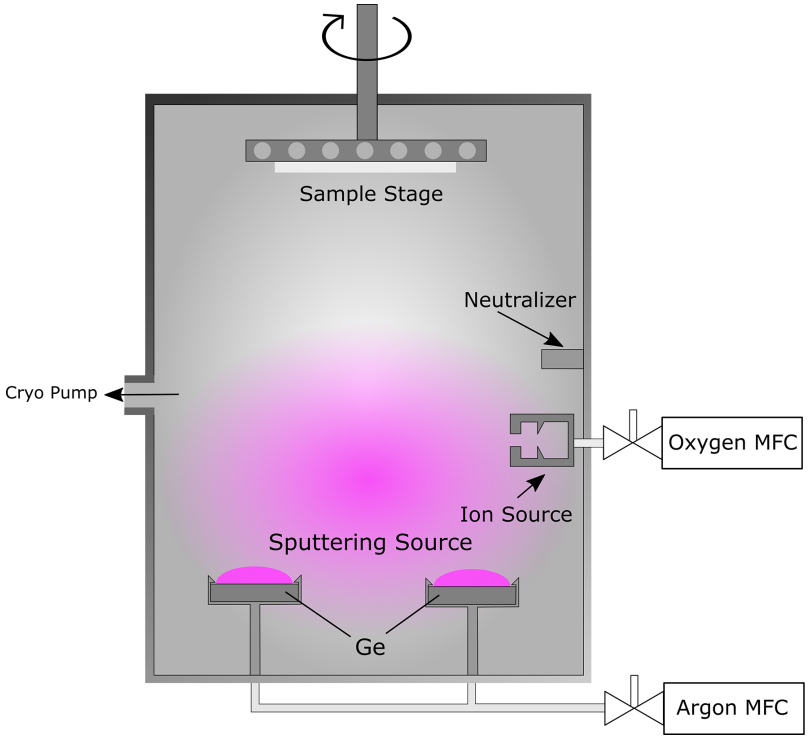

FIGURE 6.1: Schematic of the ion-assisted dual AC sputtering system applied to deposit GeO_2 thin films. The position of the ion source and neutralizer are not representative of the actual position and the system is not drawn to scale.

We deposited the GeO_2 thin films using an Intlvac Nanocrhome IV plasma assisted reactive magnetron sputtering (PARMS) system. A schematic of the

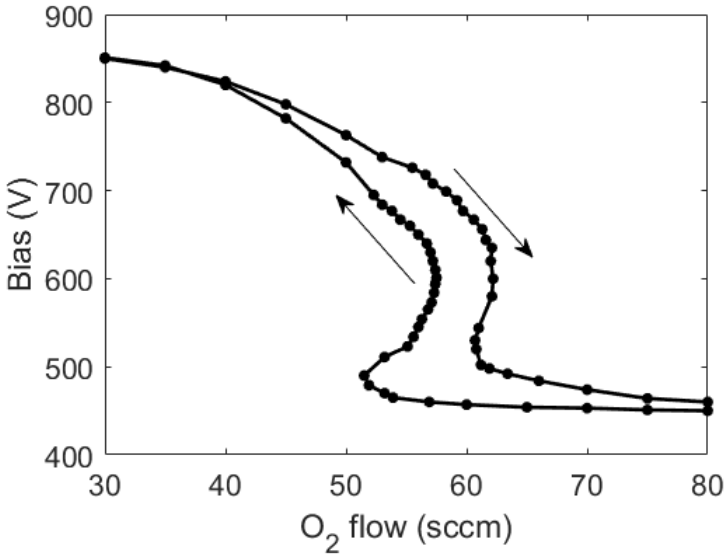

FIGURE 6.2: Target bias hysteresis for varying oxygen flow under ion-assisted deposition.

system is displayed in Fig. 6.1. The tool is a top-down sputter system that can be equipped with up to four 6 inch sputter sources for pulsed direct current (DC) or dual AC sputtering. In addition, the system contains an ion source for *in-situ* pre-cleaning and ion-assisted deposition. The PARMS system is designed for the production of dense and low defect films. Prior to the deposition, the chamber was pumped down to 1.3×10^{-7} kPa with a cryopump. Subsequently, the films were deposited under low heating, at 120 °C, using two 6-inch 99.995% pure germanium targets. The plasma processing parameters were varied across oxygen flow ranging from 40 to 80 standard cubic centimeters per minute (sccm) at constant power. In order to maintain film homogeneity during the growth process, the oxygen flow was either held constant or adjusted by an algorithm to maintain a selected target bias. In order to select the deposition parameters across different sputtering regimes, the target bias response for the system was examined. The target bias

vs. oxygen (O_2) flow rate hysteresis curves are shown in Fig. 6.2. The transition from metal to poisoned target mostly takes place between 40 and 65 sccm of O_2 flow. The difference between the curve when transitioning from oxide to metal and vice-versa are likely the result of slow variation in the chamber wall and target surface condition [184]. Films were deposited on either side of the hysteresis, i.e. where the target bias is relatively insensitive to oxygen flow and the process is inherently stable, as well as inside the hysteresis, e.g. at 550V where the algorithm is necessary to stabilize it [185]. The films were deposited on $\langle 100 \rangle$ silicon wafers for compositional analysis, as well as silicon substrates with 6-µm-thick thermal oxide for waveguide characterization, all fixed to a rotating sample holder. Further details regarding sample preparation and deposition can be found in Section 4.3.

6.2.2 Thin film characterization

We determined the composition of the GeO_2 films using RBS and ERDA. The RBS results were collected using a 1.8 MeV helium ion ($^4He^+$) ion beam in a Cornell geometry with a dose of 2 µC. The sample underwent random rotation during data acquisition to limit the effects of channeling in the crystalline silicon substrate. The ERD results were collected with a 2.9 MeV $^4He^+$ ion beam with an incident and exit angle of 75° to the normal of the sample surface. Modeling of the experimental data was performed using the SIMNRA software package to determine the stoichiometric composition of the thin films [141].

We determined the thicknesses and refractive indices of the thin films with the use of a J. A. Woollam M-2000 UV-Vis variable angle spectroscopic ellipsometry (VASE) fitted with a near-infrared extension. Measurements in the spectral range

of 250 to 1700 nm were taken at angles of 55°, 60°, 65°, 70° and 75° from the surface normal. The spectra were then analyzed with the use of J. A. Woollam's CompleteEASETM software package, assuming a homogenous film comprised of a single layer with no surface roughness on a silicon substrate [146].

In order to determine the optical loss of the deposited material, a set of 0.7-µm-thick films were grown onto 6-µm-thick thermal oxide layers on 3" diameter Si wafers. The propagation loss of the films deposited on oxidized silicon wafers was measured using a Metricon 2010/M prism coupler at 638, 847 and 1550 nm wavelength. Using a set of linear polarizers, the light was coupled into the film under transverse electric (TE) and transverse magnetic (TM) mode conditions. The mode order was selected by altering the coupling angle of the incident laser onto the prism with the fundamental TE and TM modes being chosen. Measurements were performed across different regions of the wafer approximately ten times and the statistical average of these measurements was selected as the loss of the film. We carried out multiple measurements to account for the sensitivity of the prism coupling system to the scattering of the propagating light from surface defects along the beam path. Pieces of the GeO_2-coated oxide oxidized Si wafers were cleaved and annealed separately in an annealing furnace under a constant N2 gas flow of 60 sccm. The samples were annealed at temperatures ranging from 200 °C to 400 °C in steps of 50 °C.

The surface roughness of 1.0-µm-thick films on polished silicon was measured using AC mode AFM. A probe stiffness of 60 N/m and a frequency of 300 kHz was used. Three random 2 µm x 2 µm locations on the surface were measured to determine the average root mean squared (RMS) roughness of the film. This scan

size was significantly larger than the surface features, thus was determined to be sufficiently large to obtain an average roughness. The data analysis for the AFM measurements was performed in the WSXM 5.0 application [150].

6.3 Results and discussion

Fig. 6.3 shows the experimental RBS spectra and corresponding simulated fit for a GeO_2 thin film grown with an O_2 flow rate of 60 sccm. A single layer model for the deposited film consisting of germanium, oxygen, and silicon was applied to the experimental data. There is no evidence of interstitial argon in the films based on a lack of signal around 1000 keV. From the fitted models, it can be observed that the films are near stoichiometric GeO_2 within the experimental uncertainty for germanium of 0.1 at. % and oxygen of 0.8 at. %. This uncertainty is obtained through the fit statistics given by the SIMNRA software. The lower uncertainty in the atomic percentage of germanium compared with oxygen can be attributed to germanium's higher atomic mass, which results in a larger atomic cross-section and a higher probability of scattering incoming $^4He^+$ ions. This stronger scattering renders the concentration of heavier elements more sensitive to measurement. The composition of the GeO_2 thin films does not change for different oxygen flow rates operating in the poisoning regime for the Ge targets as well as the metal sputtering regime and the hysteresis mid-point.

Fig. 6.4 shows the ERDA spectrum measured for the same GeO_2 film in order to characterize the hydrogen content. The simulated model suggests a hydrogen concentration of 1.1 at. % spread evenly throughout the thickness of the film. The source of this hydrogen is not certain. A possible explanation is the instruction of

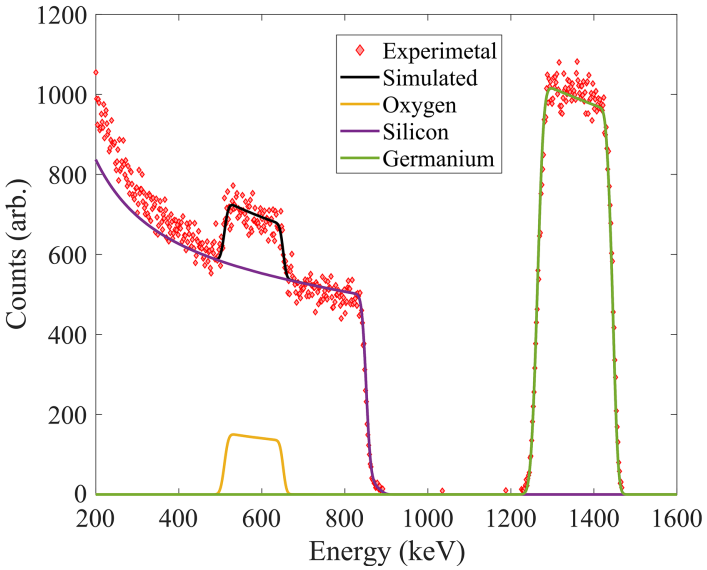

FIGURE 6.3: RBS experimental spectra (red dots) and fits based on a simulation model for a GeO_2 thin film. The yellow, purple, and green fit lines represent oxygen, silicon, and germanium, respectively. The composition of the GeO_2 is stoichiometric within the uncertainty in the simulated model.

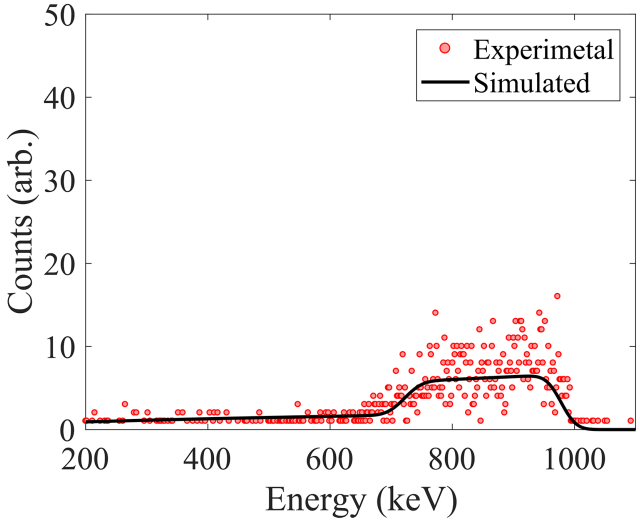

FIGURE 6.4: ERDA experimental spectra (red dots) with fit based on simulation model for 1.1 at.% hydrogen content uniformly distributed throughout the film.

hydrogen into the chamber from residual water vapor which is then incorporated into the film during the deposition. Alternatively, the hydrogen in the film might arise from water vapor diffusing into the film between deposition and ERDA measurements. We note that the presence of hydrogen in the films can be useful for specific applications. It is proposed that the presence of OH groups can contribute to defect sites such as germanium electron trap centers and these centers contribute to the photorefractive properties of GeO_2 when exposed to ultraviolet (UV) light [186], [187].

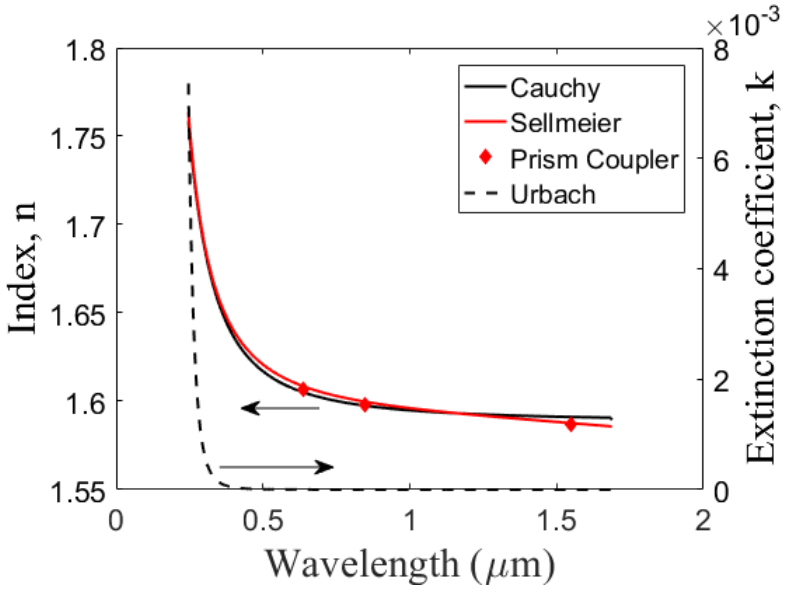

FIGURE 6.5: Material dispersion of GeO_2 thin film deposited with 60 sccm O_2 flow measured with VASE and prism coupler.

The Cauchy and Sellmeier model were applied to characterize the dispersion properties of the GeO_2 thin films from data obtained through VASE. The film loss was characterized using the Urbach absorption model. For this model, the parameters of the silicon substrate were taken from Herzinger [177]. Fig. 6.5 shows the Cauchy dispersion model and Urbach absorption as well as the Sellmeier model

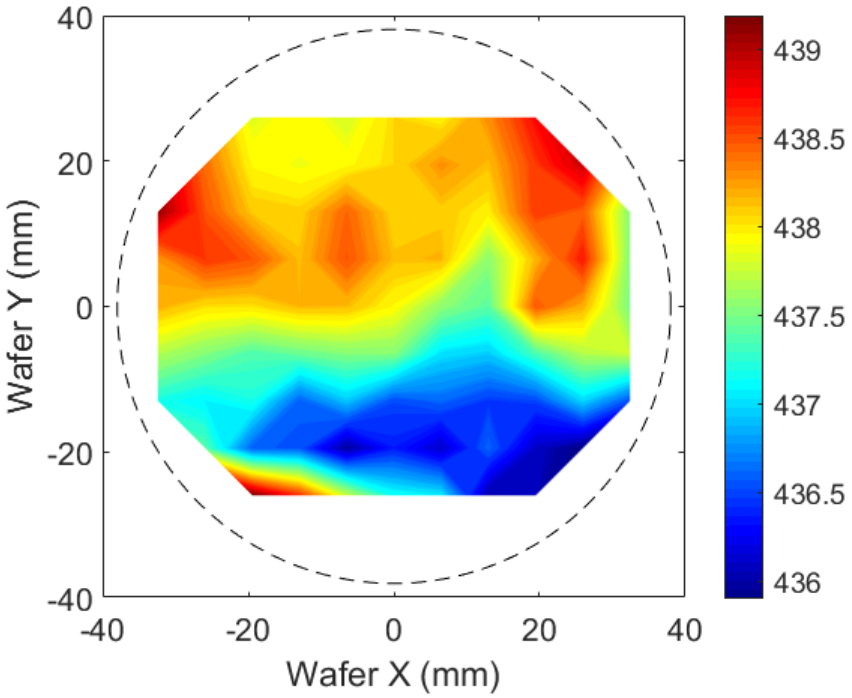

FIGURE 6.6: Height of GeO_2 thin film in nm using the Cauchy model measured across 3 inch silicon wafer

for a 60-sccm O_2 flow GeO_2 film. Overlaid on top of the dispersion curves are direct refractive index measurements obtained using prism coupling at three separate wavelengths. These overlap with the Cauchy and Sellmeier dispersion model except for the measurement taken at 1550 nm in which the Cauchy model overestimates the index. This difference is expected as the Sellmeier model is considered better over large wavelength ranges. The Cauchy model serves as a reasonable approximation across the visible region and is defined by the three-term function:

$$n = A + \frac{B}{\lambda^2} + \frac{C}{\lambda^4} + ..., \quad k = 0 \tag{6.1}$$

where the fitting parameters A, B and C are the material-dependent Cauchy

coefficients, n is the refractive index of the film and λ is the wavelength. Likewise, a 2-term Sellmeier model was used given by the formula:

$$n^2 = \epsilon(\infty) + \frac{B_1\lambda^2}{\lambda^2 - C_1} - E\lambda^2, \quad k = 0 \tag{6.2}$$

where $\epsilon(\infty)$ is the index offset, B_1 and C_1 are the experimentally determined Sellmeier coefficients and E is the position of the pole in the infrared. The values for the dispersion models shown in Fig. 6.5 are presented in Table 6.1. The refractive indices reported here are similar to those reported elsewhere using other deposition techniques [43], [64]. Fig. 6.6 shows the height map of a 3-inch silicon wafer coated in GeO_2 positioned mid-way between the center and the edge of the sample stage. The film shows high uniformity across a large area with a relative deviation in thickness (Max-Min)/average of 0.8 % across the 437.7 nm thick GeO_2 thin film with a standard deviation from the mean of 0.2 %.

TABLE 6.1: Cauchy and Sellmeier dispersion parameters coefficients obtained through VASE.

Cauchy	A	B $(\mu m)^2$	C $(\mu m)^4$	
	1.587	6.31 $\times 10^{-3}$	2.278 $\times 10^{-4}$	
Sellmeier	$\epsilon(\infty)$	B_1	C_1 $(\mu m)^2$	E $(\mu m)^{-2}$
	1.665	8.63 $\times 10^{-1}$	1.5447 $\times 10^{-1}$	8.84 $\times 10^{-3}$

Sputtering at lower oxygen flow rates resulted in a significant increase in the deposition rate, from 8 to 10 nm/min at flow rates of greater than 60 sccm to 38 nm/min at 40 sccm, as shown in Fig. 6.7. This increase in deposition rate primarily

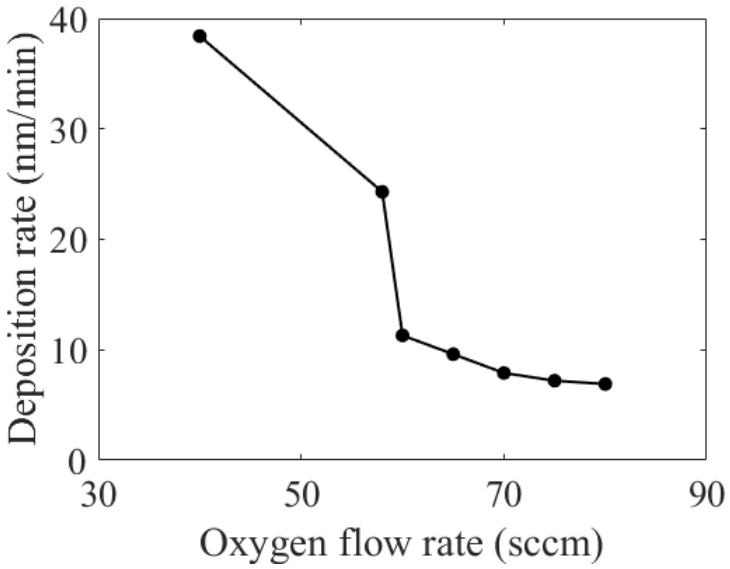

FIGURE 6.7: Height of GeO_2 thin film in nm using the Cauchy model measured across 3 inch silicon wafer.

can be attributed to the lower O_2 partial pressure, reducing target surface oxidation, thus increasing the germanium sputtering probability at lower O_2 flow rates. There a noticeable trend in the thin film losses deposited at different deposition rates. Those films deposited at lower rates in the poisoned regime showed low losses that were at the measurement limit of 0.1 dB/cm at 638 nm across the wafer for both the fundamental TE and TM modes. Films that were grown in the knee of the hysteresis with deposition rates around 25 nm/min showed losses around 0.2 dB/cm at 638 nm, and films grown in the metal sputtering region showed losses around 0.5 dB/cm at 638 nm, for both the fundamental TE and TM modes.

AFM was used to study whether surface roughness could account for the higher losses at 638 nm seen in the films with higher deposition rates. The RMS surface roughness of films deposited with between 60 and 80 sccm of O_2 and with deposition rates below 10 nm/min was typically 0.5 to 0.8 nm. This is consistent with other

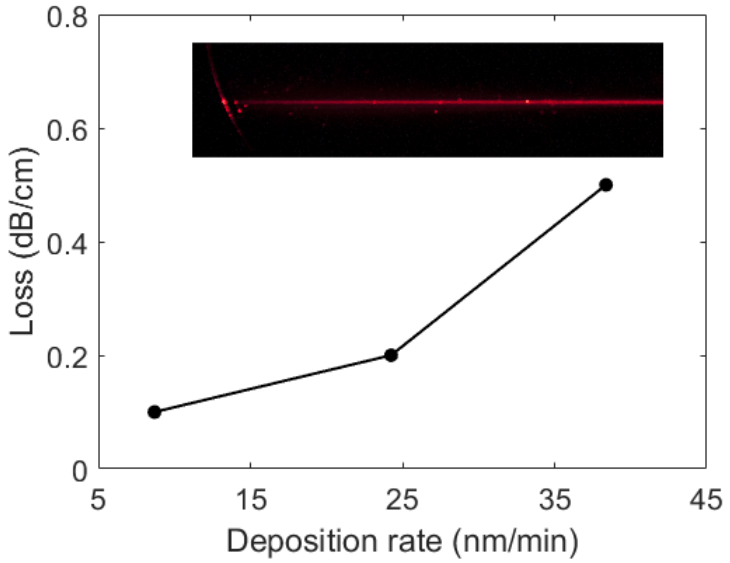

FIGURE 6.8: As deposited film loss at 638 nm measured by the prism coupling method of TE mode light vs. deposition rate. Insert shows 638 nm red streak from prism coupler coupling into GeO_2 film.

films grown through PARMS [188]. Annealing selected films in the range of 200 °C to 400 °C, as shown in Fig. 6.9, did not yield a noticeable difference in roughness compared to the as-deposited films. It can be noted that there appears to be a correlation between surface roughness and loss, shown in Table 6.2. The film with an RMS surface roughness of 0.92 nm exhibited the highest loss with 0.5 dB/cm at 638 nm. Conversely, the film with an RMS surface roughness of 0.54 nm had the lowest loss of 0.1 dB/cm at 638 nm. The loss in these films appears to decrease at higher wavelengths with all of them measuring a loss at 0.1 dB/cm at a wavelength of 980 nm. Given that scattering is scaled as λ^{-4}, we would expect the loss decrease at higher wavelengths if the primary loss mechanism was caused through light scattering at the interfaces.

The RMS roughnesses of the as-deposited films are less than those of similar GeO_2 films grown by radio frequency (RF) magnetron sputtering [64] and DC

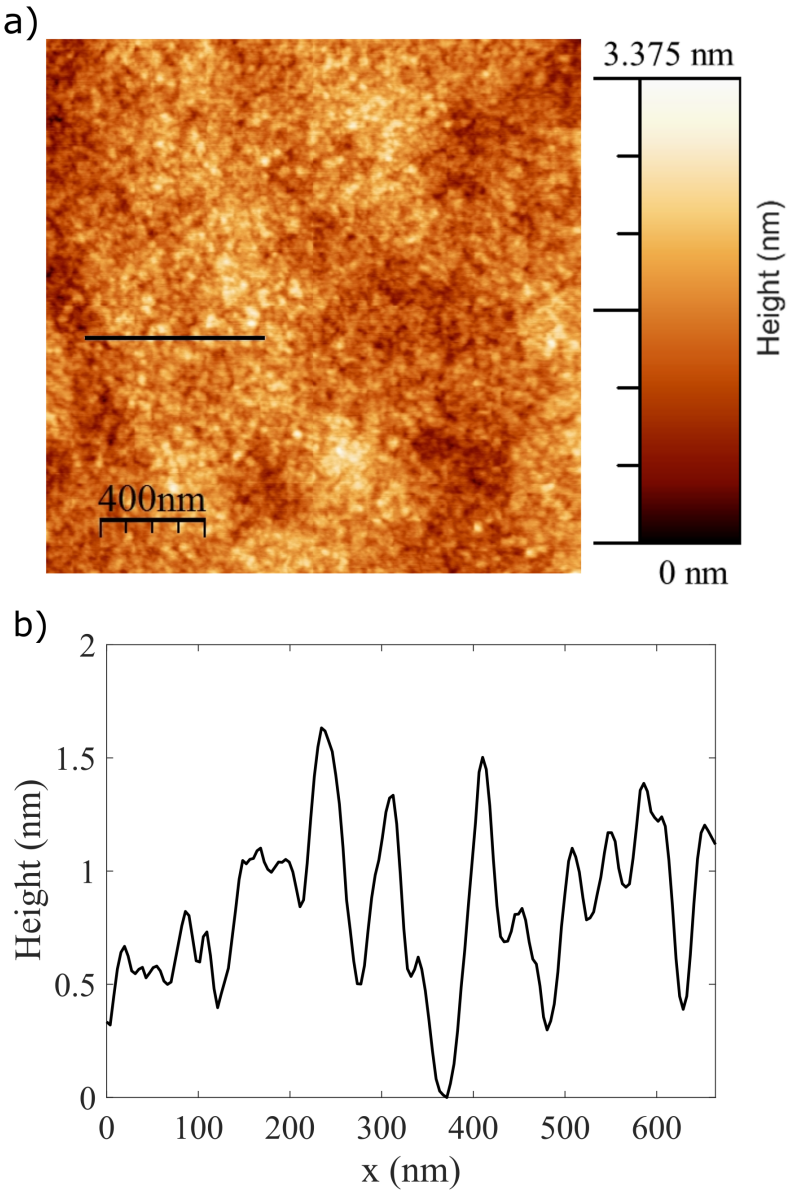

FIGURE 6.9: a) AFM profile for a 1-µm-thick GeO_2 thin film annealed at 400 °C with RMS roughness of 0.45 nm and peak to peak roughness of 3.8 nm. b) Height profile taken from AFM scan in a).

TABLE 6.2: Deposition parameters, atomic concentrations obtained through RBS, refractive index obtained through VASE, RMS roughness and peak to peak roughness for films obtained through AFM, losses obtained from prism coupling.

O_2 flow rate (sccm)	Ge (at. % ± 0.1)	O (at. % ± 0.8)	n (638 nm)	Loss, 638 nm (dB/cm)	R_{RMS} (nm)	Peak to Peak (nm)
40	31.0	69.0	1.603	0.5	0.92	9.2
55	31.0	69.0	1.600	0.2	0.73	6.2
60	32.5	67.5	1.605	0.1	0.54	4.1
65	32.5	67.5	1.605	-	0.53	5.1
70	32.8	67.2	1.605	-	1.21	8.6
75	33.0	67.0	1.605	-	0.77	8.9
80	32.8	67.2	1.605	-	0.45	3.8

reactive sputtering [63]. Thin films grown using PARMS have been shown to exhibit high packing densities and film surface uniformity [188]. The losses in these GeO_2 films are also shown to be less than the films grown using other methods without the need for post-processing.

6.4 Conclusion

We have demonstrated low-loss GeO_2 thin films fabricated by PARMS AC sputtering and show an improvement in losses for the as-deposited GeO_2 films compared to previous deposition techniques. The films were shown to be stoichiometric through RBS measurements, and the refractive index was modeled through VASE and prism coupler measurements and determined to be around 1.605 at 638 nm. The film composition and refractive index were found to be constant for different O_2 flow rates. Small amounts of hydrogen were present in the films, which might not be considered detrimental as hydrogen is known to sensitize GeO_2 to change its refractive index through the photorefractive effect. The films were shown to have

sub-nanometer surface roughnesses down to 0.5 nm, as determined through AFM, and losses as low as 0.1 dB/cm at 638 nm without the need for post-deposition process steps. The films also had high uniformity across a 3-inch wafer with a relative thickness deviation of 0.8%. The low surface roughnesses and losses demonstrate ion-assisted dual AC sputtering to be especially attractive for the deposition of optical waveguide materials.

Chapter 7

Conclusion

7.1 Summary

This thesis has focused on the deposition and characterization of group IV oxides. It has established both novel, complementary metal-oxide-semiconductor (CMOS) compatible techniques for rare-earth incorporation in silicon-based thin films as well as low optical loss germanium oxide (GeO_2) thin films for silicon photonics applications.

In Chapter 2, a summary of the physics of light emission from rare-earth doped solid thin films was presented, followed by a literature review of host materials for rare-earth dopants for silicon photonics applications. Details on the sample characterization techniques and tools used throughout this thesis were provided in Chapter 3.

Chapter 4 highlighted the development and assembly of a novel hybrid sputtering system in an electron cyclotron resonance (ECR)-plasma enhanced chemical vapour

deposition (PECVD) chamber and was followed by a description of the fabrication techniques used to produce samples.

A study of the system calibration for the novel hybrid sputtering ECR-PECVD system is performed in Chapter 5 for the *in-situ* incorporation of rare-earth ions into a silicon-based thin film matrix. For this system, the rare-earth concentration can be easily adjusted by varying the power to the sputtering tool. This relationship is non-linear at lower sputtering powers and linear at higher powers, perhaps due to the influence of the ECR magnet deflecting lower energy sputtered ions. The refractive index, obtained through variable angle spectroscopic ellipsometry (VASE), and film density, obtained from Rutherford backscattering spectrometry (RBS), were found to increase with higher concentrations of rare-earth dopants. Terbium was selected as a visible light-emitting rare-earth dopant to show light emission from a film deposited using this technique. Prominent green light from Tb^{3+} $^5D_4 \rightarrow {}^7F_5$ related photoluminescence (PL) was observed by the naked eye under dark room lighting conditions. The annealing conditions required to activate Tb^{3+} ions embedded in the silicon dioxide host matrix were investigated using high resolution (HR)-transmission electron microscopy (TEM) imaging. This imaging, in conjunction with electron energy loss spectroscopy (EELS) and energy dispersive X-ray spectroscopy (EDX), showed the formation of silicon clusters in the amorphous thin film observed in the samples subjected to post-deposition annealing at 1100 °C which corresponded to an increase in PL intensity. The results of this chapter show that custom hybrid sputtering in an ECR-PECVD system produced silicon-based thin films with a high level of control over dopant levels and achieved doping concentrations comparable to a metal-organic process.

In Chapter 6, low-loss GeO_2 thin films were fabricated by low pressure alternating current (AC) plasma assisted reactive magnetron sputtering (PARMS) utilizing germanium targets in an oxygen plasma environment. The germanium oxide films ranging from 0.7- to 1.0-µm-thick were fabricated at low temperature and high deposition rates of 6–38 nm/min on silicon and thermally oxidized silicon substrates. This sputtering technique produced as-deposited films that were shown to have an improved loss compared to previous deposition techniques. These losses, which were obtained using a prism coupler, were as low as 0.1 dB/cm from 638 nm to 980 nm for both fundamental transverse electric (TE) and transverse magnetic (TM) modes. It is speculated that if the primary loss mechanism for these films was through surface interface scattering, given that the scattering scales by λ^{-4}, the expected loss should decrease at higher wavelengths. RBS analysis has shown that the films produced were stoichiometric and VASE measurements indicated a refractive index of 1.6051 at 638 nm. The physical composition and refractive index are insensitive over the range of oxygen flow used during deposition, which covers both the metal and poisoning scheme of the reactive sputtering hysteresis. The films are also highly uniform across the 3-inch sputtering area with relative thickness deviations of 0.8%. The surface roughness' obtained using atomic force microscopy (AFM) show sub-nanometer root mean squared (RMS) roughness as low as 0.5 nm. The results of this chapter demonstrate that GeO_2 thin films deposited through AC PARMS are especially attractive for the deposition of optical waveguide materials.

7.2 Suggested future work

Suggested avenues of investigation that could extend upon work presented in this thesis are discussed. The successful integration of the co-sputtering tool for rare-earth-doping in an ECR-PECVD system, discussed in Section 4.1, opens up a broad set of materials for fabrication using this novel technique. Cerium for blue light emission and europium for red light emission would complement the green light emission from terbium. If these results prove successful, the material systems could perhaps be combined in a stacked multilayer device to be used as a white light emitter.

Preliminary results have been shown in this work for the integration of erbium into a silicon dioxide (SiO_2) matrix utilizing the novel hybrid deposition system. This material system could be further explored for integration into existing waveguide platforms, such as silicon and silicon nitride, as a cladding material for signal enhancement of C-band signals. This platform could further be used to study the erbium lifetimes in films produced and estimate the percentage of optically active ions through the comparison of experimental and simulated results. Preliminary work had also been conducted on introducing thulium dopants into silicon-based thin films for light emission around 1.8 µm. This material system could similarly be deposited onto silicon photonic waveguide platforms and be used for amplifiers or light sources operating near 2 µm. At present, there is currently contamination from a heavy element (molybdenum or niobium according to RBS data) in these samples. It remains uncertain if this contamination is from the target or a result of an unknown external source. As a starting point, a small amount of material could be removed from the surface of the target after it has been cleaned, and EDX

could be performed to determine its purity. Many other dopants can be expored for integrated light-emiting devices, including neodymium and ytterbium for 1 µm sources.

Another exciting avenue that could be explored is the addition of a second high vacuum (HV) magnetron sputtering tool to the ECR system. This addition would allow for the co-doping of rare-earth materials into silicon-based thin films. Work could be done, using the new technique, to replicate the very successful previously demonstrated cerium and terbium co-doped oxides from the group. Lightly doped terbium silicon oxides, when sensitized with cerium and annealed at high temperatures, had shown very strong blue-green emission. Similarly, any comprehensive study concerning erbium-doped oxides could benefit from an in-depth look at co-doping erbium and ytterbium using the new system. It has been previously shown through co-doping of these two elements can reduce erbium-ion clustering and significantly improve pump-to-signal conversion efficiency.

It would be interesting to investigate the plasma physics of the hybrid sputtering ECR-PECVD system. As discussed in Section 4.1, the operation of the system shows a plasma trail connecting the magnetron to the ECR chamber. An investigation to determine the influence of the magnetic field generated by the ECR magnet on both the magnetic field of the magnetron sputtering head and plasma density throughout the chamber. This study could be carried out using a Langmuir probe to map the temperature and density of the electrons in the plasma, including the plasma electric potential. Simulations of the chamber magnetic field and density could accompany this investigation. A better understanding of the plasma physics will benefit thin film deposition and optimization studies using this new system.

Bibliography

[1] Q. Cheng, M. Bahadori, M. Glick, *et al.*, "Recent advances in optical technologies for data centers: a review," *Optica*, vol. 5, no. 11, p. 1354, Nov. 2018. DOI: 10.1364/OPTICA.5.001354.

[2] N. Farrington and A. Andreyev, "Facebook's data center network architecture," in *2013 Optical Interconnects Conference*, IEEE, 2013. DOI: 10.1109/oic.2013.6552917.

[3] J. Du and J. Wang, "Design and fabrication of hybrid SPP waveguides for ultrahigh-bandwidth low-penalty terabit-scale data transmission," *Optics Express*, vol. 25, no. 24, pp. 30 124–30 134, 2017. DOI: 10.1364/OE.25.030124.

[4] C. Gui, C. Li, Q. Yang, and J. Wang, "Demonstration of terabit-scale data transmission in silicon vertical slot waveguides," *Optics express*, vol. 23, no. 8, pp. 9736–9745, 2015. DOI: 10.1364/OE.23.009736.

[5] Z. Ruan, L. Shen, S. Zheng, and J. Wang, "Subwavelength grating slot (SWGS) waveguide on silicon platform," *Optics express*, vol. 25, no. 15, pp. 18 250–18 264, 2017. DOI: 10.1364/OE.25.018250.

[6] S. Zheng, N. Zhou, Y. Long, *et al.*, "Compact tunable photonic comb filter on a silicon platform," *Optics Letters*, vol. 42, no. 14, pp. 2762–2765, 2017.

[7] A. Samani, D. Patel, M. Chagnon, *et al.*, "Experimental parametric study of 128 Gb/s PAM-4 transmission system using a multi-electrode silicon photonic Mach Zehnder modulator," *Optics express*, vol. 25, no. 12, pp. 13 252–13 262, 2017. DOI: 10.1364/OE.25.013252.

[8] B. Milivojevic, S. Wiese, S. Anderson, *et al.*, "Demonstration of optical transmission at bit rates of up to 321.4 Gb/s using compact silicon based modulator and linear BiCMOS MZM driver," *Journal of Lightwave Technology*, vol. 35, no. 4, pp. 768–774, 2016, ISSN: 0733-8724.

[9] R. Dubé-Demers, S. LaRochelle, and W. Shi, "Ultrafast pulse-amplitude modulation with a femtojoule silicon photonic modulator," *Optica*, vol. 3, no. 6, pp. 622–627, 2016. DOI: 10.1364/OPTICA.3.000622.

[10] J. Cui and Z. Zhou, "High-performance Ge-on-Si photodetector with optimized DBR location," *Optics Letters*, vol. 42, no. 24, pp. 5141–5144, 2017. DOI: 10.1364/OL.42.005141.

[11] H. Chen, P. Verheyen, P. De Heyn, *et al.*, " -1 V bias 67 GHz bandwidth Si-contacted germanium waveguide pin photodetector for optical links at 56 Gbps and beyond," *Optics Express*, vol. 24, no. 5, pp. 4622–4631, 2016. DOI: 10.1364/OE.24.004622.

[12] J. J. Ackert, D. J. Thomson, L. Shen, *et al.*, "High-speed detection at two micrometres with monolithic silicon photodiodes," *Nature Photonics*, vol. 9, no. 6, pp. 393–396, 2015. DOI: 10.1038/nphoton.2015.81.

[13] D. Thomson, A. Zilkie, J. E. Bowers, *et al.*, "Roadmap on silicon photonics," *Journal of Optics*, vol. 18, no. 7, p. 073 003, Jul. 2016. DOI: 10.1088/2040-8978/18/7/073003.

[14] S. Ossicini, L. Pavesi, and F. a. Priolo, "Silicon Nanostructures: Wells, Wires, and Dots," in *Springer Tracts in Modern Physics*, Springer Berlin Heidelberg, 2003, pp. 123–178. DOI: 10.1007/978-3-540-44877-8_4.

[15] Y. a. Kanemitsu, "Light emission from porous silicon and related materials," vol. 263, no. 1, pp. 1–91, 1995. DOI: 10.1016/0370-1573(95)00021-4.

[16] T. Karacali and K. Çiçek, "Strong white light emission from a processed porous silicon and its photoluminescence mechanism," *Journal of luminescence*, vol. 131, no. 10, pp. 2100–2105, 2011. DOI: 10.1016/j.jlumin.2011.05.031.

[17] E. Secret, C. Leonard, S. J. Kelly, *et al.*, "Size control of porous silicon-based nanoparticles via pore-wall thinning," *Langmuir*, vol. 32, no. 4, pp. 1166–1170, 2016. DOI: 10.1021/acs.langmuir.5b04220.

[18] E. M. T. Fadaly, A. Dijkstra, J. R. Suckert, *et al.*, "Direct-bandgap emission from hexagonal Ge and SiGe alloys," *Nature*, vol. 580, no. 7802, pp. 205–209, 2020. DOI: 10.1038/s41586-020-2150-y.

[19] B. Fazio, P. Artoni, M. A. Iatì, *et al.*, "Strongly enhanced light trapping in a two-dimensional silicon nanowire random fractal array," *Light: Science & Applications*, vol. 5, no. 4, e16062–e16062, 2016.

[20] M. Chen, C. Pan, T. Zhang, *et al.*, "Tuning light emission of a pressure-sensitive silicon/ZnO nanowires heterostructure matrix through piezo-phototronic effects," *ACS nano*, vol. 10, no. 6, pp. 6074–6079, 2016. DOI: 10.1021/acsnano.6b01666.

[21] W. Gu, X. Liu, X. Pi, *et al.*, "Silicon-quantum-dot light-emitting diodes with interlayer-enhanced hole transport," *IEEE Photonics Journal*, vol. 9, no. 2, pp. 1–10, 2017. DOI: 10.1109/JPHOT.2017.2671023.

[22] B. Ghosh, H. Yamada, S. Chinnathambi, *et al.*, "Inverted device architecture for enhanced performance of flexible silicon quantum dot light-emitting diode," *The Journal of Physical Chemistry Letters*, vol. 9, no. 18, pp. 5400–5407, 2018. DOI: 10.1021/acs.jpclett.8b02278.

[23] F. Meinardi, S. Ehrenberg, L. Dhamo, *et al.*, "Highly efficient luminescent solar concentrators based on earth-abundant indirect-bandgap silicon quantum dots," *Nature Photonics*, vol. 11, no. 3, pp. 177–185, 2017. DOI: 10.1038/nphoton.2017.5.

[24] S. Gallis, H. Efstathiadis, M. Huang, *et al.*, "Photoluminescence at 1540 nm from erbium-doped amorphous silicon carbide films," *Journal of Materials Research*, vol. 19, no. 8, pp. 2389–2393, 2004. DOI: 10.1557/jmr.2004.0292.

[25] M. G. Mynbaeva, E. N. Mokhov, A. A. Lavrent'ev, and K. D. Mynbaev, "High-temperature diffusion doping of porous silicon carbide," *Technical Physics Letters*, vol. 34, no. 9, p. 731, 2008. DOI: 10.1134/S1063785008090034.

[26] V. I. Gavrilenko, S. I. Frolov, and N. I. Klyui, "Electronic band structure and optical properties of cubic silicon carbide crystals," *Physica B: Condensed Matter*, vol. 185, no. 1-4, pp. 394–399, 1993. DOI: 10.1016/0921-4526(93)90267-A.

[27] S. Yerci, R. Li, and L. Dal Negro, "Electroluminescence from Er-doped Si-rich silicon nitride light emitting diodes," *Applied Physics Letters*, vol. 97, no. 8, p. 81 109, 2010. DOI: 10.1063/1.3483771.

[28] A. C. Hryciw, R. D. Kekatpure, S. Yerci, *et al.*, "Thermo-optic tuning of erbium-doped amorphous silicon nitride microdisk resonators," *Applied Physics Letters*, vol. 98, no. 4, p. 41 102, 2011. DOI: 10.1063/1.3545845.

[29] J. M. Ramírez, S. Cueff, Y. Berencen, *et al.*, "Role of silicon excess in Er-doped silicon-rich nitride light emitting devices at 1.54 μ m," *Journal of Applied Physics*, vol. 116, no. 8, p. 83 103, 2014. DOI: 10.1063/1.4893706.

[30] J. H. Shin, S.-y. Seo, S. Kim, and S. G. Bishop, "Photoluminescence excitation spectroscopy of erbium-doped silicon-rich silicon oxide," *Applied Physics Letters*, vol. 76, no. 15, pp. 1999–2001, 2000. DOI: 10.1063/1.126234.

[31] S.-Y. Seo and J. H. Shin, "Carrier-induced Er 3+ luminescence quenching of erbium-doped silicon-rich silicon oxide," *Applied Physics Letters*, vol. 75, no. 26, pp. 4070–4072, 1999. DOI: 10.1063/1.125539.

[32] M. Shah, M. Wojdak, A. J. Kenyon, *et al.*, "Rate equation modelling of erbium luminescence dynamics in erbium-doped silicon-rich-silicon-oxide," *Journal of luminescence*, vol. 132, no. 12, pp. 3103–3112, 2012. DOI: 10.1016/j.jlumin.2012.02.002.

[33] H. A. Lopez and P. M. Fauchet, "Room-temperature electroluminescence from erbium-doped porous silicon," *Applied Physics Letters*, vol. 75, no. 25, pp. 3989–3991, 1999. DOI: 10.1117/12.382845.

[34] Y. Zhou, P. A. Snow, and P. S. J. Russell, "Strong modification of photoluminescence in erbium-doped porous silicon microcavities," *Applied Physics Letters*, vol. 77, no. 16, pp. 2440–2442, 2000. DOI: 10.1063/1.1318230.

[35] A. Najar, H. Elhouichet, N. Lorrain, and M. Oueslati, "Excitation mechanisms and localization sites of erbium-doped porous silicon," *Applied surface science*, vol. 252, no. 16, pp. 5808–5813, 2006. DOI: 10.1016/j.apsusc.2005.07.071.

[36] N. V. Gaponenko, V. M. Parkun, O. S. Katernoga, *et al.*, "Erbium and terbium photoluminescence in silica sol–gel films on porous alumina," *Thin Solid Films*, vol. 297, no. 1-2, pp. 202–206, 1997. DOI: 10.1016/s0040-6090(96)09533-8.

[37] H. Amekura, A. Eckau, R. Carius, and C. Buchal, "Room-temperature photoluminescence from Tb ions implanted in SiO2 on Si," *Journal of Applied Physics*, vol. 84, no. 7, pp. 3867–3871, 1998. DOI: 10.1063/1.368591.

[38] A. J. Kenyon, "Recent developments in rare-earth doped materials for optoelectronics," *Progress in Quantum Electronics*, vol. 26, no. 4-5, pp. 225–284, 2002. DOI: 10.1016/S0079-6727(02)00014-9.

[39] F. Gloux, T. Wojtowicz, P. Ruterana, *et al.*, "Transmission electron microscopy investigation of the structural damage formed in GaN by medium range energy rare earth ion implantation," *Journal of Applied Physics*, vol. 100, no. 7, p. 073 520, Oct. 2006. DOI: 10.1063/1.2357845.

[40] A. Polman, D. C. Jacobson, D. J. Eaglesham, *et al.*, "Optical doping of waveguide materials by MeV Er implantation," *Journal of Applied Physics*, vol. 70, no. 7, pp. 3778–3784, Oct. 1991. DOI: 10.1063/1.349234.

[41] A. Podhorodecki, G. Zatryb, L. W. Golacki, *et al.*, "On the origin of emission and thermal quenching of SRSO:Er^{3+} films grown by ECR-PECVD,"

Nanoscale Research Letters, vol. 8, no. 1, p. 98, Dec. 2013. DOI: 10.1186/1556-276X-8-98.

[42] P. J. Lemaire, A. M. Vengsarkar, W. A. Reed, and D. J. DiGiovanni, "Thermally enhanced ultraviolet photosensitivity in GeO_2 and P_2O_5 doped optical fibers," *Applied Physics Letters*, vol. 66, no. 16, pp. 2034–2036, 1995. DOI: 10.1063/1.113683.

[43] S. Valligatla, A. Chiasera, N. Bazzanella, *et al.*, "CO_2 Laser irradiation of GeO_2 planar waveguide fabricated by rf-sputtering," *IOP Conference Series: Materials Science and Engineering*, vol. 73, no. 1, pp. 1537–1545, 2015. DOI: 10.1088/1757-899X/73/1/012006.

[44] F. L. Galeener, J. C. Mikkelsen, R. H. Geils, and W. J. Mosby, "The relative Raman cross sections of vitreous SiO_2, GeO_2, B_2O_3, and P_2O_5," *Applied Physics Letters*, vol. 32, no. 1, pp. 34–36, 1978. DOI: 10.1063/1.89823.

[45] A. Jha, B. Richards, G. Jose, *et al.*, "Rare-earth ion doped TeO_2 and GeO_2 glasses as laser materials," *Progress in Materials Science*, vol. 57, no. 8, pp. 1426–1491, 2012. DOI: 10.1016/j.pmatsci.2012.04.003.

[46] E. Dianov and V. Mashinsky, "Germania-based core optical fibers," *Journal of Lightwave Technology*, vol. 23, no. 11, pp. 3500–3508, Nov. 2005. DOI: 10.1109/JLT.2005.855867.

[47] S. Sebastiani, G. N. Conti, S. Pelli, *et al.*, "Characterization of a highly photorefractive RF-sputtered SiO_2-GeO_2 waveguide," *Optics Express*, vol. 13, no. 5, p. 1696, 2005. DOI: 10.1364/OPEX.13.001696.

[48] J.-P. Bérubé, A. Le Camus, S. H. Messaddeq, *et al.*, "Femtosecond laser direct inscription of mid-IR transmitting waveguides in BGG glasses," *Optical Materials Express*, vol. 7, no. 9, p. 3124, Sep. 2017. DOI: 10.1364/OME.7.003124.

[49] T. Geernaert, M. Becker, P. Mergo, *et al.*, "Bragg Grating Inscription in GeO_2-Doped Microstructured Optical Fibers," *Journal of Lightwave Technology*, vol. 28, no. 10, pp. 1459–1467, May 2010. DOI: 10.1109/JLT.2010.2043414.

[50] X. Liu, X. Yang, F. Lu, *et al.*, "Stable and uniform dual-wavelength erbium-doped fiber laser based on fiber Bragg gratings and photonic crystal fiber," *Optics Express*, vol. 13, no. 1, p. 142, Jan. 2005. DOI: 10.1364/OPEX.13.000142.

[51] A. D. Kersey, T. A. Berkoff, and W. W. Morey, "Multiplexed fiber Bragg grating strain-sensor system with a fiber Fabry–Perot wavelength filter," *Optics Letters*, vol. 18, no. 16, p. 1370, Aug. 1993. DOI: 10.1364/OL.18.001370.

[52] B. Eggleton, T. Stephens, P. Krug, *et al.*, "Dispersion compensation using a fibre grating in transmission," *Electronics Letters*, vol. 32, no. 17, p. 1610, 1996. DOI: 10.1049/el:19961027.

[53] Y. Fukuda, Y. Yazaki, Y. Otani, *et al.*, "Low-Temperature Formation of High-Quality GeO_2 Interlayer for High-κ Gate Dielectrics/Ge by Electron-Cyclotron-Resonance Plasma Techniques," *IEEE Transactions on Electron Devices*, vol. 57, no. 1, pp. 282–287, Jan. 2010. DOI: 10.1109/TED.2009.2035030.

[54] Rajni, "Realization of Directional-Coupler-Based Optical Waveguide Devices by Ultraviolet-Imprinting Technique Using Sol-Gel Derived Inorganic GeO_2 : SiO_2 Films," *IEEE Photonics Technology Letters*, vol. 19, no. 24, pp. 2048–2050, Dec. 2007. DOI: 10.1109/LPT.2007.909685.

[55] W. Bogaerts and L. Chrostowski, "Silicon Photonics Circuit Design: Methods, Tools and Challenges," *Laser & Photonics Reviews*, vol. 12, no. 4, p. 1 700 237, Apr. 2018. DOI: 10.1002/lpor.201700237.

[56] J. Hübner, S. Guldberg-Kjaer, M. Dyngaard, *et al.*, "Planar Er- and Yb-doped amplifiers and lasers," *Applied Physics B*, vol. 73, no. 5-6, pp. 435–438, Oct. 2001. DOI: 10.1007/s003400100697.

[57] C. B. de Araújo, L. R. Kassab, C. Tolentino Dominguez, *et al.*, "Photoluminescence and nonlinear optical phenomena in plasmonic random media—A review of recent works," *Journal of Luminescence*, vol. 169, pp. 492–496, Jan. 2016. DOI: 10.1016/j.jlumin.2014.11.013.

[58] S. Huang, Y. Xiao, J. Liu, *et al.*, "Nd^{3+}-doped antimony germanate glass for 1.06 μm fiber lasers," *Journal of Non-Crystalline Solids*, vol. 518, pp. 10–17, Aug. 2019. DOI: 10.1016/j.jnoncrysol.2019.05.008.

[59] D. Manzani, M. Montesso, C. Mathias, *et al.*, "Visible up-conversion and near-infrared luminescence of Er^{3+}/Yb^{3+} co-doped $SbPO_4$-GeO_2 glasses," *Optical Materials*, vol. 57, pp. 71–78, Jul. 2016, ISSN: 09253467. DOI: 10.1016/j.optmat.2016.04.019.

[60] L. Kassab, D. Kumada, D. da Silva, and J. Garcia, "Enhanced infrared-to-visible frequency upconversion in Yb^{3+}/Er^{3+} codoped Bi_2O_3–GeO_2 glasses

with embedded silver nanoparticles," *Journal of Non-Crystalline Solids*, vol. 498, 395–400, Oct. 2018. DOI: 10.1016/j.jnoncrysol.2018.03.019.

[61] M. M. Martins, L. R. Kassab, D. M. da Silva, and C. B. de Araújo, "Tm^{3+} doped Bi_2O_3-GeO_2 glasses with silver nanoparticles for optical amplifiers in the short-wave-infrared-region," *Journal of Alloys and Compounds*, vol. 772, pp. 58–63, Jan. 2019. DOI: 10.1016/j.jallcom.2018.08.146.

[62] D. E. Hagan, B. Torres-Kulik, and A. P. Knights, "Post-Fabrication Trimming of Silicon Ring Resonators via Integrated Annealing," *IEEE Photonics Technology Letters*, vol. 31, no. 16, pp. 1373–1376, Aug. 2019. DOI: 10.1109/LPT.2019.2927323.

[63] T. Lange, W. Njoroge, H. Weis, *et al.*, "Physical properties of thin GeO_2 films produced by reactive DC magnetron sputtering," *Thin Solid Films*, vol. 365, no. 1, pp. 82–89, 2000. DOI: 10.1016/S0040-6090(99)01106-2.

[64] Z. Yi Yin and B. K. Garside, "Low-loss GeO_2 optical waveguide fabrication using low deposition rate rf sputtering," *Applied Optics*, vol. 21, no. 23, p. 4324, Dec. 1982. DOI: 10.1364/AO.21.004324.

[65] A. Chiasera, C. Macchi, S. Mariazzi, *et al.*, "GeO_2 glass ceramic planar waveguides fabricated by RF-sputtering," M. J. F. Digonnet and S. Jiang, Eds., Mar. 2014, p. 89820D. DOI: 10.1117/12.2042099.

[66] V. Del Cacho, D. da Silva, L. Kassab, *et al.*, "PbO–GeO_2 rib waveguides for photonic applications," *Journal of Alloys and Compounds*, vol. 509, S434–S437, Jun. 2011. DOI: 10.1016/j.jallcom.2011.01.141.

[67] F. Bomfim, D. da Silva, L. Kassab, *et al.*, "Advances on the fabrication process of Er^{3+}/Yb^{3+}:GeO_2–PbO pedestal waveguides for integrated photonics," *Optical Materials*, vol. 49, pp. 196–200, Jan. 2015, ISSN: 09253467. DOI: 10.1016/j.optmat.2015.09.010.

[68] S. Ossicini, L. Pavesi, and F. Priolo, "Introduction: Fundamental Aspects," in *Light Emitting Silicon for Microphotonics*, 2003, pp. 1–36. DOI: 10.1007/978-3-540-44877-8_1.

[69] D. J. Lockwood, "Progress in Light Emission from Silicon Nanostructures," in *Spectroscopy of Emerging Materials*, Dordrecht: Kluwer Academic Publishers, pp. 97–114. DOI: 10.1007/1-4020-2396-0_8.

[70] J. R. Chelikowsky and M. L. Cohen, "Nonlocal pseudopotential calculations for the electronic structure of eleven diamond and zinc-blende semiconductors," *Phys. Rev. B*, vol. 14, pp. 556–582, 2 Jul. 1976. DOI: 10.1103/PhysRevB.14.556.

[71] G. H. Dieke, H. Crosswhite, and H. M. Crosswhite, *Spectra and energy levels of rare earth ions in crystals.* English. 1968.

[72] J.-C. G. Bünzli and S. V. Eliseeva, "Intriguing aspects of lanthanide luminescence," *Chemical Science*, vol. 4, no. 5, p. 1939, 2013, Electronic supplementary information (ESI). DOI: 10.1039/c3sc22126a.

[73] Encyclopædia Britannica, *Electron probabilities for gadolinium.* [Online]. Available: https://www.britannica.com/science/rare-earth-element/Minerals-and-ores#/media/1/491579/187149 (visited on 07/2010).

[74] A. J. Freeman and R. E. a. Watson, "Theoretical Investigation of Some Magnetic and Spectroscopic Properties of Rare-Earth Ions," *Physical Review*, vol. 127, no. 6, pp. 2058–2075, 1962. DOI: 10.1103/physrev.127.2058.

[75] G. K. Liu, *Spectroscopic Properties of Rare Earths in Optical Materials*, R. Hull, J. Parisi, R. M. Osgood, *et al.*, Eds., ser. Springer Series in Materials Science. Berlin, Heidelberg: Springer Berlin Heidelberg, 2005, vol. 83, ch. 1, pp. 1–94. DOI: 10.1007/3-540-28209-2.

[76] P. R. J. Wilson, "Study of Luminescent Silicon-Rich Silicon Nitride and Cerium and Terbium Doped Silicon Oxide Thin Films," Ph.D. McMaster University, 2013, p. 187.

[77] B. M. Walsh, "Judd-Ofelt theory: principles and practices," in *Advances in Spectroscopy for Lasers and Sensing*, Dordrecht: Springer Netherlands, 2006, pp. 403–433. DOI: 10.1007/1-4020-4789-4_21.

[78] L. Smentek, "Judd—Ofelt theory: past, present and future," *Molecular Physics*, vol. 101, no. 7, pp. 893–897, Apr. 2003.

[79] M. P. Hehlen, M. G. Brik, and K. W. Krämer, "50th anniversary of the Judd–Ofelt theory: An experimentalist's view of the formalism and its application," *Journal of Luminescence*, vol. 136, pp. 221–239, Apr. 2013. DOI: 10.1016/j.jlumin.2012.10.035.

[80] D. E. Mccumber, "Einstein Relations Connecting Broadband Emission and Absorption Spectra," *Physical Review*, vol. 136, no. 4A, A954–A957, 1964. DOI: 10.1103/physrev.136.a954.

[81] S. A. Payne, L. L. Chase, L. K. Smith, *et al.*, "Infrared cross-section measurements for crystals doped with Er^{3+}, Tm^{3+}, and Ho^{3+}," *IEEE Journal of Quantum Electronics*, vol. 28, no. 11, pp. 2619–2630, 1992. DOI: 10.1109/3.161321.

[82] D. L. Sidebottom, M. A. Hruschka, B. G. Potter, and P. K. Brow, "Structure and Optical Properties of Rare Earth-Doped Zinc Oxyhalide Tellurite Glass," University of New Mexico and Sandia national Laboratories, Albuquerque,NM, Tech. Rep., 1997, p. 14.

[83] D. Yu, J. Ballato, and R. E. Riman, "Temperature-Dependence of Multiphonon Relaxation of Rare-Earth Ions in Solid-State Hosts," *The Journal of Physical Chemistry C*, vol. 120, no. 18, pp. 9958–9964, May 2016, ISSN: 1932-7447. DOI: 10.1021/acs.jpcc.6b01466.

[84] R. Reisfeld and C. K. Jorgensen, *Lasers and excited states of rare earths*. Springer Science & Business Media, 2012, vol. 1.

[85] A. Kaminskii, *Crystalline lasers: physical processes and operating schemes*. CRC press, 1996, vol. 12.

[86] A. J. Kenyon, "Erbium in silicon," *Semiconductor Science and Technology*, vol. 20, no. 12, R65–R84, 2005. DOI: 10.1088/0268-1242/20/12/R02.

[87] J. Palm, F. Gan, B. Zheng, *et al.*, "Electroluminescence of erbium-doped silicon," *Physical Review B*, vol. 54, no. 24, pp. 17 603–17 615, 1996. DOI: 10.1103/physrevb.54.17603.

[88] A. a. Polman, "Erbium implanted thin film photonic materials," *Journal of Applied Physics*, vol. 82, no. 1, pp. 1–39, 1997. DOI: 10.1063/1.366265.

[89] F. Auzel and P. Goldner, "Towards rare-earth clustering control in doped glasses," *Optical Materials*, vol. 16, no. 1-2, pp. 93–103, Feb. 2001. DOI: 10.1016/S0925-3467(00)00064-1.

[90] G. N. van den Hoven, E. Snoeks, A. Polman, *et al.*, "Upconversion in Er-implanted Al_2O_3 waveguides," *Journal of Applied Physics*, vol. 79, no. 3, pp. 1258–1266, Feb. 1996. DOI: 10.1063/1.361020.

[91] C. Chryssou and C. Pitt, "Er^{3+}-doped Al_2O_3 thin films by plasma-enhanced chemical vapor deposition (PECVD) exhibiting a 55-nm optical bandwidth," *IEEE Journal of Quantum Electronics*, vol. 34, no. 2, pp. 282–285, 1998. DOI: 10.1109/3.658711.

[92] E. S. Hosseini, Purnawirman, J. D. B. Bradley, *et al.*, "CMOS-compatible 75 mW erbium-doped distributed feedback laser," *Optics Letters*, vol. 39, no. 11, p. 3106, Jun. 2014. DOI: 10.1364/OL.39.003106.

[93] N. Li, D. Vermeulen, Z. Su, *et al.*, "Monolithically integrated erbium-doped tunable laser on a CMOS-compatible silicon photonics platform," *Optics Express*, vol. 26, no. 13, p. 16 200, Jun. 2018. DOI: 10.1364/OE.26.016200.

[94] N. Li, M. Xin, Z. Su, *et al.*, "A Silicon Photonic Data Link with a Monolithic Erbium-Doped Laser," *Scientific Reports*, vol. 10, no. 1, p. 1114, Dec. 2020. DOI: 10.1038/s41598-020-57928-5.

[95] H. C. Frankis, K. M. Kiani, D. B. Bonneville, *et al.*, "Low-loss TeO_2-coated Si_3N_4 waveguides for application in photonic integrated circuits," *Opt. Express*, vol. 27, no. 9, pp. 12 529–12 540, Apr. 2019. DOI: 10.1364/OE.27.012529.

[96] R. Rolli, A. Chiasera, M. Montagna, *et al.*, "Rare-earth-activated fluoride and tellurite glasses: optical and spectroscopic properties," S. Jiang, Ed., Apr. 2001, p. 109. DOI: 10.1117/12.424767.

[97] Y. Hu, S. Jiang, G. Sorbello, *et al.*, "Cooperative upconversion in a new high-Er-doped tellurite glass," S. Jiang, Ed., Apr. 2001, p. 57. DOI: 10.1117/12.424760.

[98] H. C. Frankis, H. M. Mbonde, D. B. Bonneville, *et al.*, "Erbium-doped TeO_2-coated Si_3N_4 waveguide amplifiers with 5 dB net gain," *Photon. Res.*, vol. 8, no. 2, pp. 127–134, Feb. 2020. DOI: 10.1364/PRJ.8.000127.

[99] K. M. Kiani, H. C. Frankis, H. M. Mbonde, *et al.*, "Thulium-doped tellurium oxide waveguide amplifier with 7.6 dB net gain on a silicon nitride chip," *Opt. Lett.*, vol. 44, no. 23, pp. 5788–5791, Dec. 2019. DOI: 10.1364/OL.44.005788.

[100] I. Massarek, "Deposition and modelling of rare-earth doped optical films," Ph.D. University College London, 1994, p. 135.

[101] B. Walker, C. C. Dharmawardhana, N. Dari, *et al.*, "Electronic structure and optical properties of amorphous GeO_2 in comparison to amorphous SiO_2," *Journal of Non-Crystalline Solids*, vol. 428, pp. 176–183, Nov. 2015. DOI: 10.1016/j.jnoncrysol.2015.08.018.

[102] X. Jiang, J. Lousteau, and A. a. Jha, "The Structural, Thermal, and Optical Analyses of Multicomponent Germanium Oxide Glasses for Engineering Mid-Infrared Fiber Chemical Sensing," *Journal of the American Ceramic Society*, vol. 93, no. 10, pp. 3259–3266, 2010. DOI: 10.1111/j.1551-2916.2010.03913.x.

[103] C. B. Layne, W. H. Lowdermilk, and M. J. a. Weber, "Multiphonon relaxation of rare-earth ions in oxide glasses," *Physical Review B*, vol. 16, no. 1, pp. 10–20, 1977. DOI: 10.1103/physrevb.16.10.

[104] L. R. P. Kassab, M. M. Miranda, D. K. Kumada, *et al.*, *Journal of Materials Science: Materials in Electronics*, vol. 30, no. 18, pp. 16 781–16 788, 2019. DOI: 10.1007/s10854-019-01312-1.

[105] A. Menéndez, P. Sánchez, and D. Gómez, "Deposition of Thin Films: PECVD Process," in *Silicon Based Thin Film Solar Cells*, A. Menéndez, P. Sánchez, and D. Gómez, Eds., Bentham Science Publishers, Mar. 2013, ch. 2, pp. 29–57. DOI: 10.2174/978160805518011301000 6.

[106] A. Tarazona, T. D. Bucio, S. Oo, *et al.*, "Hot wire chemical vapor deposition for silicon photonics: An emerging industrial application opportunity," *Thin Solid Films*, vol. 676, pp. 26–30, Apr. 2019, ISSN: 00406090. DOI: 10.1016/j.tsf.2019.02.048.

[107] C. Duty, D. Jean, and W. Lackey, "Laser chemical vapour deposition: materials, modelling, and process control," *International Materials Reviews*, vol. 46, no. 6, 271–287, Jun. 2001. DOI: 10.1179/095066001771048727.

[108] Y. Hamedani, P. Macha, T. J. Bunning, *et al.*, "Plasma-Enhanced Chemical Vapor Deposition: Where we are and the Outlook for the Future," in *Chemical Vapor Deposition - Recent Advances and Applications in Optical, Solar Cells and Solid State Devices*, InTech, Aug. 2016. DOI: 10.5772/64654.

[109] C. Yang and J. Pham, "Characteristic Study of Silicon Nitride Films Deposited by LPCVD and PECVD," *Silicon*, vol. 10, no. 6, pp. 2561–2567, Nov. 2018. DOI: 10.1007/s12633-018-9791-6.

[110] C. Drosos and D. Vernardou, "Perspectives of energy materials grown by APCVD," *Solar Energy Materials and Solar Cells*, vol. 140, pp. 1–8, Sep. 2015, ISSN: 09270248. DOI: 10.1016/j.solmat.2015.03.019.

[111] V. Astié, C. Millon, J.-M. Decams, and A. Bartasyte, "Direct Liquid Injection Chemical Vapor Deposition," in *Chemical Vapor Deposition for Nanotechnology*, IntechOpen, Nov. 2018. DOI: 10.5772/intechopen.80244.

[112] T. Detchprohm, J.-H. Ryou, X. Li, and R. Dupuis, "Future Aspects of MOCVD Technology for Epitaxial Growth of Semiconductors," in *Metalorganic Vapor Phase Epitaxy (MOVPE)*, Wiley, Oct. 2019, pp. 507–548. DOI: 10.1002/9781119313021.ch14.

[113] "Fundamental properties of a-SiN_x:H thin films deposited by ICP-PECVD for MEMS applications," *Applied Surface Science*, vol. 284, pp. 348–353, 2013. DOI: https://doi.org/10.1016/j.apsusc.2013.07.104.

[114] S. R. Droes, T. T. Kodas, and M. J. Hampden-Smith, "Plasma-Enhanced Chemical Vapor Deposition (PECVD)," in *Carbide, Nitride and Boride Materials Synthesis and Processing*, Dordrecht: Springer Netherlands, 1997, pp. 579–603. DOI: 10.1007/978-94-009-0071-4_23.

[115] E. Meeks, R. S. Larson, P. Ho, *et al.*, "Modeling High-Density-Plasma Deposition of SiO_2 in $SiH_4/O_2/Ar$," Sandia National Laboratories, Livermore,CA, Tech. Rep., 1997, p. 52.

[116] O. Blázquez, J. López-Vidrier, L. López-Conesa, *et al.*, "Structural and optical properties of Al-Tb/SiO_2 multilayers fabricated by electron beam evaporation," *Journal of Applied Physics*, vol. 120, no. 13, p. 135 302, Oct. 2016, ISSN: 0021-8979. DOI: 10.1063/1.4964110.

[117] J. L. Frieiro, O. Blázquez, J. López-Vidrier, *et al.*, "Green Electroluminescence of Al/Tb/Al/SiO_2 Devices Fabricated by Electron Beam Evaporation," *physica status solidi (a)*, vol. 215, no. 3, p. 1 700 451, Feb. 2018. DOI: 10.1002/pssa.201700451.

[118] N. Hardy, *Thin Film Deposition By Sputtering: Essential Basics*, 2013. [Online]. Available: http://www.semicore.com/news/70-thin-film-deposition-sputtering (visited on 07/2017).

[119] N. Hardy, *What is reactive sputtering?* 2013. [Online]. Available: http://www.semicore.com/news/67-reactive-sputtering-basics (visited on 07/2017).

[120] N. Hardy, *What are planar magnetrons in pvd coatings?* 2013. [Online]. Available: http://www.semicore.com/news/66-planar-magnetron-pvd-coating (visited on 07/2017).

[121] M. Pollnau and J. D. B. Bradley, "Optically pumped rare-earth-doped Al_2O_3 distributed-feedback lasers on silicon [Invited]," *Optics Express*, vol. 26, no. 18, p. 24 164, 2018. DOI: 10.1364/OE.26.024164.

[122] K. Vu, S. Farahani, and S. Madden, "980nm pumped erbium doped tellurium oxide planar rib waveguide laser and amplifier with gain in S, C and L band," *Optics Express*, vol. 23, no. 2, p. 747, 2015. DOI: 10.1364/OE.23.000747.

[123] P. Sakthivel, S. Asaithambi, M. Karuppaiah, *et al.*, "Different rare earth (Sm, La, Nd) doped magnetron sputtered CdO thin films for optoelectronic applications," *Journal of Materials Science: Materials in Electronics*, vol. 30, no. 10, pp. 9999–10 012, 2019. DOI: 10.1007/s10854-019-01342-9.

[124] J. Kalkman, A. Polman, T. Kippenberg, *et al.*, "Erbium-implanted silica microsphere laser," *Nuclear Instruments and Methods in Physics Research Section B: Beam Interactions with Materials and Atoms*, vol. 242, no. 1-2, pp. 182–185, Jan. 2006. DOI: 10.1016/j.nimb.2005.08.160.

[125] S. Wang, L. Yang, R. Cheng, *et al.*, "Incorporation of erbium ions into thin-film lithium niobate integrated photonics," *Applied Physics Letters*, vol. 116, no. 15, p. 151 103, Apr. 2020. DOI: 10.1063/1.5142631.

[126] P. Roychowdhury and D. P. Chakravarthy, "High intensity electron cyclotron resonance proton source for low energy high intensity proton accelerator," *Review of Scientific Instruments*, vol. 80, no. 12, p. 123 305, Dec. 2009. DOI: 10.1063/1.3272786.

[127] F. F. Chen, *Introduction to Plasma Physics*. Boston, MA: Springer US, 1995, ISBN: 978-1-4757-0461-7. DOI: 10.1007/978-1-4757-0459-4.

[128] K.-M. Byun and W.-J. Lee, "Deposition characteristics of low dielectric constant SiOF films prepared by ECR PECVD," *Metals and Materials*, vol. 6, no. 2, pp. 155–160, Mar. 2000. DOI: 10.1007/BF03026360.

[129] J. Li, "Light Emission From Rare Earth-Doped Silicon Oxide Films Deposited By ECR-PECVD," Ph.D. McMaster University, 2008, p. 141.

[130] J. M. Ramírez, A. Ruiz-Caridad, J. Wojcik, *et al.*, "Luminescence properties of Ce^{3+} and Tb^{3+} co-doped SiO_xN_y thin films: Prospects for color tunability in silicon-based hosts," *Journal of Applied Physics*, vol. 119, no. 11, p. 113 108, Mar. 2016. DOI: 10.1063/1.4944433.

[131] T. Roschuk, P. R. J. Wilson, J. Li, *et al.*, "Structure and luminescence of rare earth-doped silicon oxides studied through their X-ray absorption near edge structure and X-ray excited optical luminescence," *physica status solidi (b)*, vol. 247, no. 2, pp. 248–253, Feb. 2010. DOI: 10.1002/pssb.200945531.

[132] M. Scherer, J. Pistner, and W. Lehnert, "UV- and VIS Filter Coatings by Plasma Assisted Reactive Magnetron Sputtering (PARMS)," in *Optical Interference Coatings*, Tucson, Arizona: OSA, 2010, MA7. DOI: 10.1364/OIC.2010.MA7.

[133] J. Broßmann, T. Best, T. Bauer, *et al.*, "Low-loss interference filter arrays made by plasma-assisted reactive magnetron sputtering (PARMS) for high-performance multispectral imaging," R. Meynart, S. P. Neeck, T. Kimura, and H. Shimoda, Eds., Oct. 2016, 100001E. DOI: 10.1117/12.2241069.

[134] M. Scherer, H. Hagedorn, W. Lehnert, and J. Pistner, "Innovative production of thin film laser components," C. Amra, N. Kaiser, and H. A. Macleod, Eds., Sep. 2005, p. 596 319. DOI: 10.1117/12.625226.

[135] M. Hughes, *What is MF or Mid-Frequency AC Sputtering?* 2017. [Online]. Available: http://www.semicore.com/news/97-what-is-mf-ac-sputtering (visited on 07/2017).

[136] A. Anders, "Plasma and ion sources in large area coating: A review," *Surface and Coatings Technology*, vol. 200, no. 5-6, pp. 1893–1906, Nov. 2005. DOI: 10.1016/j.surfcoat.2005.08.018.

[137] S. J. Pearce, M. D. B. Charlton, J. Hiltunen, *et al.*, "Structural characteristics and optical properties of plasma assisted reactive magnetron sputtered

dielectric thin films for planar waveguiding applications," *Surface and Coatings Technology*, vol. 206, no. 23, pp. 4930–4939, 2012.

[138] S. J. Pearce, M. D. B. Charlton, G. J. Parker, and J. S. Wilkinson, "Properties of rare earth doped thin film dielectric layers for upconversion laser waveguides," in *Solid State Lasers XX: Technology and Devices*, vol. 7912, International Society for Optics and Photonics, 2011, 79122H.

[139] M. Mayer, "Rutherford Backscattering Spectrometry (RBS)," *Workshop on Nuclear Data for Science and Technology: Materials Analysis*, May 2003.

[140] L. Goncharova and Interface Science Western, *Rutherford Backscattering Spectrometry (RBS)*. [Online]. Available: http://www.isw.physics.uwo.ca/facilities_techniques/rbs.html (visited on 07/2020).

[141] M. Mayer, *SIMNRA user's guide*. Max-Planck-Institut für Plasmaphysik Garching, 1997.

[142] J. N. Hilfiker, C. L. Bungay, R. A. Synowicki, *et al.*, "Progress in spectroscopic ellipsometry: Applications from vacuum ultraviolet to infrared," *Journal of Vacuum Science & Technology A: Vacuum, Surfaces, and Films*, vol. 21, no. 4, pp. 1103–1108, Jul. 2003. DOI: 10.1116/1.1569928.

[143] H. G. Tompkins and E. A. Irene, *Handbook of Ellipsometry*, H. G. Tompkins and E. A. Irene, Eds. William Andrew, 2005, p. 886, ISBN: 0-8155-1499-9.

[144] H. Fujiwara, *Spectroscopic Ellipsometry: Principles and Applications*. Ibaraki: John Wiley & Sons, Ltd, 2007, p. 392, ISBN: 978-0-470-01608-4.

[145] F. Wooten, *Optical properties of solids*. Academic press, 2013, ISBN: 1483220761.

[146] J. A. Wollam Co. Inc, *CompleteEASE ™ Data Analysis Manual*. Lincoln, NE, 2011, pp. 1–207.

[147] Y. Gan, "Atomic and subnanometer resolution in ambient conditions by atomic force microscopy," *Surface Science Reports*, vol. 64, no. 3, pp. 99–121, Mar. 2009. DOI: 10.1016/j.surfrep.2008.12.001.

[148] U. Hartmann, *An Elementary Introduction to Atomic Force Microscopy and Related Methods*, Saarbrücken, Germany, 1997.

[149] E. Gadelmawla, M. Koura, T. Maksoud, *et al.*, "Roughness parameters," *Journal of Materials Processing Technology*, vol. 123, no. 1, pp. 133–145, Apr. 2002. DOI: 10.1016/S0924-0136(02)00060-2.

[150] I. Horcas, R. Fernández, J. M. Gómez-Rodríguez, *et al.*, "WSXM: A software for scanning probe microscopy and a tool for nanotechnology," *Review of Scientific Instruments*, vol. 78, no. 1, 2007. DOI: 10.1063/1.2432410.

[151] R. Egerton and M. Malac, "EELS in the TEM," *Journal of Electron Spectroscopy and Related Phenomena*, vol. 143, no. 2-3, pp. 43–50, May 2005. DOI: 10.1016/j.elspec.2003.12.009.

[152] O. H. Y. Zalloum, M. Flynn, T. Roschuk, *et al.*, "Laser photoluminescence spectrometer based on charge-coupled device detection for silicon-based photonics," *Review of Scientific Instruments*, vol. 77, no. 2, p. 023 907, Feb. 2006. DOI: 10.1063/1.2173030.

[153] R. Ulrich and R. Torge, "Measurement of Thin Film Parameters with a Prism Coupler," *Applied Optics*, vol. 12, no. 12, pp. 2901–2908, 1973.

[154] M. S. A. Rahman and M. H. M. Zaman, "The Measurement of Refractive Index and Thickness of Planar Waveguide Using Couple Mode Theory Method–The Programming Highlight," *Australian Journal of Basic and Applied Sciences*, vol. 3, no. 3, pp. 2901–2907, 2009.

[155] R. P. Dabkowski, "Installation of a New Electron Cyclotron Plasma Enhanced Chemical Vapour Deposition (ECR-PECVD) Reactor and a Preliminary Study of Thin Film Depositions," M.A.Sc. McMaster University, 2012, p. 172.

[156] P. S. Andry, W. J. Varhue, F. Ladipo, *et al.*, "Growth of Er-doped silicon using metalorganics by plasma-enhanced chemical vapor deposition," *Journal of Applied Physics*, vol. 80, no. 1, pp. 551–558, 1996. DOI: 10.1063/1.362759.

[157] J. H. Shin, M.-J. Kim, S.-Y. Seo, and C. Lee, "Composition dependence of room temperature 1.54 μm Er^{3+} luminescence from erbium-doped silicon:oxygen thin films deposited by electron cyclotron resonance plasma enhanced chemical vapor deposition," *Applied Physics Letters*, vol. 72, no. 9, pp. 1092–1094, Mar. 1998. DOI: 10.1063/1.120974.

[158] J. H. Shin, S.-Y. Seo, and S.-J. Lee, "Effect of hydrogenation on room-temperature 1.54 μm Er^{3+} photoluminescent properties of erbium-doped silicon-rich silicon oxide," vol. 73, no. 25, p. 3647, 1998. DOI: 10.1063/1.122850.

[159] K. J. Lesker, *Dimensional drawings*. [Online]. Available: https://www.lesker.com/newweb/images/product_drawings/dwg-tr-tm03as10.svg (visited on 02/2017).

[160] H. Zhang, "Study of Optimal Deposition Conditions for an Inductively Coupled Plasma Chemical Vapour Deposition (ICP-CVD) System," M.A.Sc. McMaster University, 2005, p. 119.

[161] Electron Microscopy Sciences, *EMS Catalog*, 77708-Series.

[162] A. Podhorodecki, G. Zatryb, J. Misiewicz, *et al.*, "Green light emission from terbium doped silicon rich silicon oxide films obtained by plasma enhanced chemical vapor deposition," *Nanotechnology*, vol. 23, no. 47, p. 475 707, Nov. 2012. DOI: 10.1088/0957-4484/23/47/475707.

[163] J. Li, O. H. Y. Zalloum, T. Roschuk, *et al.*, "Light Emission from Rare-Earth Doped Silicon Nanostructures," *Advances in Optical Technologies*, vol. 2008, pp. 1–10, 2008. DOI: 10.1155/2008/295601.

[164] J. Li, O. Zalloum, T. Roschuk, *et al.*, "The formation of light emitting cerium silicates in cerium-doped silicon oxides," *Applied Physics Letters*, vol. 94, no. 1, p. 011 112, Jan. 2009. DOI: 10.1063/1.3067871.

[165] P. R. J. Wilson, Z. Khatami, R. Dabkowski, *et al.*, "XANES and XEOL Investigation of Cerium and Terbium Co-Doped Silicon Oxide Films," *Electrochemical Society Transactions*, vol. 45, no. 5, pp. 43–48, 2012. DOI: 10.1149/1.3700408.

[166] K.-H. Dahmen, "Chemical Vapor Deposition," in *Encyclopedia of Physical Science and Technology*, Elsevier, 2003, pp. 787–808. DOI: 10.1016/B0-12-227410-5/00102-2.

[167] K. Wasa, *Handbook of Sputter Deposition Technology : Fundamentals and Applications for Functional Thin Films, Nano-Materials and MEMS*. Binghamton, United States: Elsevier Science & Technology Books, 2012, ISBN: 9781437734843.

[168] D. Lundin, T. Minea, and J. Gudmundsson, *High Power Impulse Magnetron Sputtering: Fundamentals, Technologies, Challenges and Applications*. Elsevier Science, 2019, ISBN: 9780128124550.

[169] W. Eckstein, C. Garciá-Rosales, J. Roth, and J. László, "Threshold energy for sputtering and its dependence on angle of incidence," *Nuclear Instruments and Methods in Physics Research Section B: Beam Interactions with Materials and Atoms*, vol. 83, no. 1, pp. 95–109, 1993. DOI: https://doi.org/10.1016/0168-583X(93)95913-P.

[170] C. Yan and Q. Y. a. Zhang, "Study on low-energy sputtering near the threshold energy by molecular dynamics simulations," *AIP Advances*, vol. 2, no. 3, p. 32 107, 2012. DOI: 10.1063/1.4738951.

[171] A. G. Raffa and P. Ballone, "Equilibrium structure of erbium-oxygen complexes in crystalline silicon," *Physical Review B*, vol. 65, no. 12, p. 121 309, 2002. DOI: 10.1103/PhysRevB.65.121309.

[172] M. Al-Kuhaili and S. Durrani, "Optical properties of erbium oxide thin films deposited by electron beam evaporation," *Thin Solid Films*, vol. 515, no. 5, pp. 2885–2890, Jan. 2007. DOI: 10.1016/j.tsf.2006.08.048.

[173] R. A. B. Devine, "On the structure of low-temperature PECVD silicon dioxide films," *Journal of Electronic Materials*, vol. 19, no. 11, pp. 1299–1301, Nov. 1990. DOI: 10.1007/BF02673345.

[174] Z. Khatami, P. Wilson, J. Wojcik, and P. Mascher, "The influence of carbon on the structure and photoluminescence of amorphous silicon carbonitride thin films," *Thin Solid Films*, vol. 622, pp. 1–10, Jan. 2017. DOI: 10.1016/j.tsf.2016.12.014.

[175] G. B. Bosco, Z. Khatami, J. Wojcik, *et al.*, "Excitation mechanism of Tb^{3+} in a-Si_3N_4:H under sub-gap excitation," *Journal of Luminescence*, vol. 202, pp. 327–331, 2018. DOI: 10.1016/j.jlumin.2018.05.080.

[176] L. Pavesi and R. Turan, *Silicon Nanocrystals: Fundamentals, Synthesis and Applications*, L. Pavesi and R. Turan, Eds. Wiley, Mar. 2010, p. 627. DOI: 10.1002/9783527629954.

[177] C. M. Herzinger, B. Johs, W. A. McGahan, *et al.*, "Ellipsometric determination of optical constants for silicon and thermally grown silicon dioxide via a multi-sample, multi-wavelength, multi-angle investigation," *Journal of Applied Physics*, vol. 83, no. 6, pp. 3323–3336, Mar. 1998. DOI: 10.1063/1.367101.

[178] Y. Liu, J. Hsieh, and S. Tung, "Extraction of optical constants of zinc oxide thin films by ellipsometry with various models," *Thin Solid Films*, vol. 510, no. 1-2, pp. 32–38, Jul. 2006. DOI: 10.1016/j.tsf.2005.10.089.

[179] A. K. Sinha and E. Lugujjo, "Lorentz-Lorenz correlation for reactively plasma deposited Si-N films," *Applied Physics Letters*, vol. 32, no. 4, pp. 245–246, Feb. 1978. DOI: 10.1063/1.90006.

[180] A. Podhorodecki, L. W. Golacki, G. Zatryb, *et al.*, "Excitation mechanism and thermal emission quenching of Tb ions in silicon rich silicon oxide thin films grown by plasma-enhanced chemical vapour deposition - Do we need

silicon nanoclusters?" *Journal of Applied Physics*, vol. 115, no. 14, 2014. DOI: 10.1063/1.4871015.

[181] C. Ba, S. T. Bah, M. D'Auteuil, *et al.*, "Fabrication of HighQquality VO_2 Thin Films by Ion-Assisted Dual ac Magnetron Sputtering," *ACS Applied Materials and Interfaces*, vol. 5, no. 23, pp. 12 520–12 525, 2013. DOI: 10.1021/am403807u.

[182] H. Kupfer, R. Kleinhempel, F. Richter, *et al.*, "High-rate deposition of MgO by reactive ac pulsed magnetron sputtering in the transition mode," *Journal of Vacuum Science & Technology A: Vacuum, Surfaces, and Films*, vol. 24, no. 1, pp. 106–113, Jan. 2006. DOI: 10.1116/1.2138717.

[183] S. T. Bah, C. O. Ba, M. D'Auteuil, *et al.*, "Fabrication of TaO_xN_y thin films by reactive ion beam-assisted ac double magnetron sputtering for optical applications," *Thin Solid Films*, vol. 615, pp. 351–357, Sep. 2016. DOI: 10.1016/j.tsf.2016.07.055.

[184] K. Strijckmans, R. Schelfhout, and D. Depla, "Tutorial: Hysteresis during the reactive magnetron sputtering process," *Journal of Applied Physics*, vol. 124, no. 24, 2018. DOI: 10.1063/1.5042084.

[185] S. Berg and T. Nyberg, "Fundamental understanding and modeling of reactive sputtering processes," *Thin Solid Films*, vol. 476, no. 2, pp. 215–230, 2005. DOI: 10.1016/j.tsf.2004.10.051.

[186] K. D. Simmons, G. I. Stegeman, B. G. Potter, and J. H. Simmons, "Photosensitivity of solgel-derived germanosilicate planar waveguides," *Optics Letters*, vol. 18, no. 1, pp. 25–27, 1993. DOI: 10.1007/978-3-642-78166-7_3.

[187] M. Takahashi, A. Sakoh, Y. Tokuda, *et al.*, "Photochemical process of divalent germanium responsible for photorefractive index change in GeO_2–SiO_2 glasses," *Journal of Non-Crystalline Solids*, vol. 345-346, pp. 323–327, Oct. 2004. DOI: 10.1016/j.jnoncrysol.2004.08.037.

[188] S. J. Stefan Jakobs, M. L. Marc Lappschies, U. S. Uwe Schallenberg, *et al.*, "Characterization of metal-oxide thin films deposited by plasma-assisted reactive magnetron sputtering," *Chinese Optics Letters*, vol. 8, no. S1, pp. 73–77, 2010. DOI: 10.3788/COL201008S1.0073.